

Università degli Studi di Napoli

“Federico II”

Physics Department

PhD Thesis in

Innovative Technologies for Materials, Sensors and Imaging

Engineering Metamaterials and Photonic Crystals

in the Microwave Regime:

from Superlensing to Slow-Light

Salvatore Savo

Advisor:

Prof. A. Andreone

External Advisor:

Prof. S. Sridhar

Northeastern University, USA

to my mother, my brother

and to the memory of my father...

Preface

The following work involves the study of electromagnetic properties at the microwave frequency range of a class of materials called Metamaterials. A metamaterial is an artificial composite material that exhibits an electromagnetic response unlike any that have been observed in nature or constituent materials themselves. Usually, the response results from artificially fabricated, extrinsic or low dimensional inhomogeneities. In the last decade, metamaterials have provided scientists with an alternative and reliable way to experimentally study effects that could have never been achieved using conventional materials. The most astonishing of these effects was the concept of negative refraction, which was first theorized by the Russian scientist **Victor Veselago** in 1968. Since then, the publications of milestone works by **Eli Yablonovitch** and **Sajeev John** (in 1987), and **Sir John Pendry** (in 1999), have triggered enormous interest in metamaterials research, and have resulted in a tremendous number of theoretical and experimental works in field of metamaterials worldwide.

This study focuses on how metamaterials can be integrated into the process of molding the flow of light. This dissertation is divided into two main parts. It will begin with an introduction to the world of metamaterials and their applications, and will then branch out into two sections, with each section devoted to a specific type of periodic metamaterial, Photonic Crystals (PCs), and Split Ring Resonators (SRRs). The first part of the thesis will investigate Photonic Crystals. Photonic Crystals are made of a periodic, or quasi-periodic, arrangement of dielectric elements that show unique properties in a diffraction regime when a wavelength is comparable to the

unit cell size. For this study, I will investigate, both numerically and experimentally, the electrodynamic properties of photonic crystals, focusing the attention first, to the anomalous diffraction phenomena of two-dimensional (2D) PCs proving at microwave the Pendellösung effect, which is a physical effect of the Dynamical Diffraction Theory. Positive agreement between the numerical simulations and measurements carried out in a parallel plate waveguide have been found. Second, I will focus extensively on the subwavelength properties of one-dimensional PCs made with slanted dielectric bars by experimentally demonstrating, for the first time, the superlensing capabilities of 1D structures in the microwave regime. Finally, I will numerically analyze the improvement of the focusing capacity induced by the introduction of a proper surface corrugation.

Part two of the dissertation will focus on Split Ring Resonators (SRRs) which are made of arrays of metallic resonant elements that show their anomalous properties in the effective regime when the wavelength is much larger than the unit cell dimension. I will examine, from the numerical and experimental point of view, the electromagnetic properties of metamaterial media made with split ring resonators, focusing the attention on a full comprehension of their transmission properties. I will also discuss the Slow Light properties of a planar waveguide made with a dielectric core, and a single negative index cladding made with SRRs. Today, the concept of slowing light is popular because of the potential benefits it could have on a variety of real life applications. In fact, low group velocities control light propagation from microwave to optical frequencies, and could lead to several more applications including delay line filters and phase shifters. Moreover, the field of slow light, such as those belonging to the properties of PCs used for manipulating light, is fundamental for the future of integrated photonic chips.

All the experimental characterizations presented in this dissertation have been done at microwave wavelengths by sandwiching the samples in a parallel plate waveguide. The characterization of the metamaterials transmission properties was accom-

plished by using antennas connected to a Vector Network Analyzer that serviced in measuring the phase and amplitude of the signal. Finally, the slow light properties were analyzed by measuring the electromagnetic pulse delay using a Microwave Transition Analyzer. The results outlined in the first part of this dissertation were carried out at the University of Naples “Federico II” during the first year and a half of my PhD studies, while the results from part two were made possible at the Electronic Material Research Institute at Northeastern University in Boston, where I spent the second half of my PhD. This dissertation is the result of a long term scientific collaboration between the two above-mentioned universities, which are both interested in investigating the properties of metamaterials. As a result of this collaboration, the scholarship that supported me during the three years of my PhD was co-funded by both institutions.

Acknowledgements

Now comes the time where I would like to thank all the people who contributed to my work, both directly and indirectly.

The most important element for a successful PhD experience is, without a doubt, a good advisor. For those who think that choosing an advisor is a matter of luck, I can say that I have been extremely lucky. I am grateful to my advisor, Professor Antonello Andreone, for many reasons. The most important reason, is for the profound enthusiasm that he conveyed to me, first as a mentor, and then as a scientist. Professor Andreone consistently provided me with the best conditions for my research. I also thank Dr. Emiliano Di Gennaro for assisting me with my experiments at the University of Naples - “Frederico II”.

I would like to give a special thanks to Professor Vaglio, who I referred to first when looking to pursue a PhD. His encouragement and advice was very meaningful to me.

For all the research activities that I was able to pursue at Northeastern University in Boston, I would like to thank Professor Sri Sridhar for giving me the opportunity to grow in a stimulating international research environment.

My highest appreciation and regard goes to Dr. Didier Casse at Northeastern University, who, with immense patience, enthusiasm, and professionalism, has helped me through all the key moments of my research activity, and who was there for me, both, as a mentor and a friend. I would also like to thank Didier for going for the extra mile every time I needed his help in the lab and cleanroom. I would also like to thank the rest of my research group at Northeastern University, Evin, Dayane,

Praba, Kernel, Frank, Evan and Craig for sharing with me this incredible experience, and for also sharing espresso time with me.

A special and unique thanks is for Rita, who supported and always encouraged me during the last year with a dedication that can only be found in the hearth of a woman.

This achievement is devoted to all my friends in Italy, who indirectly supported me in realizing my dreams.

Finally, this result could never have been obtained without the constant presence of my family around me. I would like to thank my mother, who always sustained and encouraged my decisions, my brother, for being the first person who supported my decision to do research, and who always made himself available to discuss science, and my grandmom, Nonna Orsola, whose fortitude and simplicity have always been the right stimuli for me during the hard times. A special and constant devotion goes to my father, who first infused me with a love and enthusiasm for science. His understanding of the amazing secrets of nature were inspiring to me, and more importantly, showed me the possibilities in the freedom of thought.

Contents

List of Figures	xiv
1 Introduction	1
1.1 Electromagnetism of Complex Materials: Metamaterials	1
1.2 Classes of Metamaterials	2
1.2.1 Photonic Crystals	2
1.2.2 Resonant Structures	3
1.2.3 Cut Wires	4
1.3 Diffractive and non Diffractive Metamaterials	4
1.4 Propagation of Waves in Right-Handed and Left-Handed Substances .	5
1.5 Refraction at the Boundary Between Right-Handed and Left-Handed Media	8
1.6 The Concept of “Perfect Lens”	10
1.6.1 Dispersion in Negative Refractive Index Metamaterials	13
1.7 Application with Metamaterials	14
1.7.1 The Invisible Cloak	14
1.7.2 Inverse Phenomena in Left-Handed Metamaterials	18
I Diffractive Metamaterials	20
2 Photonic Crystals	21
2.1 Introduction	21

2.2	Photonic Crystals Properties	22
2.3	Scaling Properties of the Maxwell Equations	25
2.4	Photonic Band Structure	26
2.5	Wave Vector Diagram	28
2.6	Diffraction Phenomena: from Electronic Crystals to Photonic Crystals	32
2.6.1	The Pendellösung Effect in Photonic Crystals	33
2.6.2	Experimental Observation of the Pendellösung Effect at Microwave Frequencies	36
2.6.3	Application: Polarizing Beam Splitter	43
3	Superlensing in Photonic Crystals	44
3.1	Introduction	44
3.2	Superlensing in 2D Photonic Crystals	44
3.3	Superlensing in 1D Photonic Crystals	48
3.3.1	Study of the Focusing Properties and Effect of Surface Corrugation	51
3.3.2	Experimental Results	53
II	Non-Diffractive Metamaterials	58
4	Thin-Wires and Split Ring Resonators	59
4.1	Introduction	59
4.2	Thin-Wire Medium	60
4.3	Split Ring Resonators	62
4.3.1	Circuit Modeling of SRRs	66
4.4	Effective Parameters Retrieval Technique	68
5	Theory of Slow-Light in Metamaterials Structures	72
5.1	Introduction	72

5.2	State of the Art	73
5.3	Slow-Light Theory	76
5.3.1	Slow-Light in Single Negative Metamaterial Waveguides	78
5.4	Negative Permeability with SRRs	81
6	Waveguide Realization and Experimental Results	89
6.1	Microfabrication of SRRs Based Metamaterials	89
6.2	Experimental Characterization of the SRRs	92
6.3	Experimental Characterization of the Slowlight Waveguide	97
6.3.1	Experimental Setup	97
6.3.2	Pulsed Measurements	99
	Bibliography	105

List of Figures

1-1	Schematic diagram of the vector basis formed by \mathbf{E} , \mathbf{H} , \mathbf{k} and \mathbf{S} when the propagation occurs in a right-handed(a) and in a left-handed media.	7
1-2	Ray diagram of the refraction effect at the interface between two positive media and a positive and a negative indexed media. Blue arrows indicate the phase velocity while the red arrows refer to the energy velocity.	9
1-3	Ray diagram of the electromagnetic waves propagation through a negative refractive index slab having a width d and with a source located at a distance l from the first interface.	9
1-4	(a) Image formation due to the contribution of the propagating waves and evanescent waves respectively in conventional lens (a,b) and superlens (c,d) [1]	12
1-5	Schematics of imaging by a negatively-refractive medium(a) and imaging by a conventional lens(b).	12
1-6	Schematic diagram of light propagation in an open cavity made with negative and positive refractive media.	13

1-7	<p>Snapshots of time-dependent, steady-state electric field patterns, with stream lines [black lines in (a)] indicating the direction of power flow (i.e., the Poynting vector). The cloak lies in the annular region between the black circles and surrounds a conducting Cu cylinder at the inner radius. The fields shown are (a) the simulation of the cloak with the exact material properties, (b) the experimental measurement of the cloaked conducting cylinder.</p>	15
1-8	<p>The transformation optical design for the ground-plane cloak. The metamaterial cloak region is embedded in a uniform higher index background with gradients introduced at the edges to form impedance matching regions. (a) Photograph of the fabricated metamaterial sample. (b) Metamaterial refractive index distribution. The coordinate transformation region is shown within the box outlined in black. (c) Expanded view of the transformation optical region in which the mesh lines indicate the quasi-conformal mapping. Measured field mapping (E-field) of the ground, perturbation, and ground-plane cloaked perturbation. The rays display the wave propagation direction, and the dashed line indicates the normal of the ground in the case of free space and that of the ground-plane cloak in the case of the transformed space. (d) Collimated beam incident on the ground plane. Collimated beam incident on the ground-plane cloaked perturbation.</p>	16

1-9	(a) Schematic of Čerenkov radiation in a conventional natural medium with positive refractive index, in which the radiation falls in a cone in the forward direction. (b) Schematic of backward Čerenkov radiation in a left-handed medium, showing the reversed cone. (c) Schematics of the phased dipole array. (d) experimental setup with the metamaterial wedge placed on top of the phased dipole array and next to it is the picture of the metamaterial array made with split ring resonators and cut wires.	17
1-10	(a) Radiation power diagram for the Čerenkov effect observed at $8.5GHz$. The inset show the experimental setup where the source is in port 1. (b) Sum of the radiation power in each angle in the negative band (solid line) and positive band (dashed line).	18
2-3	(a) Band surface for a photonic crystal with an triangular unit cell, (b) corresponding equifrequency contour limited to the first band only.	29
2-5	(a) EFC plotted in the first and repeated Brillouin zones at $f=0.58$ for a TM mode (H field parallel to the rod axis) and the corresponding (b) ray diagram of the diffraction in the corresponding photonic crystal made of air holes (red colored) arranged in a triangular array and embedded in dielectric having $\epsilon_r = 12.96$ (yellow colored).	32
2-6	The band structure of the square-lattice PC for the TE polarization. The red line represents the normalized frequency $\omega_n = 0.722$ at which the Pendellösung effect takes place	34
2-7	The reciprocal space with the first Brillouin zone (dotted line) and symmetry points for the square-lattice PC. The contours for the normalized frequency $\omega_n = 0.722$ are plotted. Arrows indicate the directions of group velocity \mathbf{v}_g , whereas \hat{n} shows the normal to the incident surface.	35

2-8	Schematics of the basic setup used to perform measurements at microwave frequencies.	36
2-9	Pictures of the open parallel plate waveguide with the photonic crystal and the guiding structure made of absorbers used to generate a directive beam.	38
2-10	Schematic layout of the experiment carried out on the square-lattice PC slab having 25 rods columns and a number of rows n varying from 10 to 1. The dashed line box represents the scanned area during the measurements	39
2-11	(a)-(e): mapping of the measured electric field (real part) in a normalized scale for even n ; (f)-(j): mapping of the measured electric field (real part) in a normalized scale for odd n	40
2-12	The measured electric field intensity ratio I_+/I_- for all the crystal configurations considered. The case of 10 rows corresponds to the maximum thickness $t = (10a + 2r) = 16.4cm$	41
2-13	(a) FDTD simulation of the propagation pattern inside a crystal consisting of 10 rows of the $13.784GHz$ plane wave modulated by a rectangular profile and incident at an angle of 43.8° across the XM interface; (b) and (c): electric field intensity distribution (blue dashed lines) along line 1 and 2 respectively compared with the experimental results (red solid lines)	42
2-14	FDTD simulation for TM (a) and TE polarization (b). The incident wave ($\omega = 0.413$) has a Gaussian profile impinges at an angle 20.6° over a PC square lattice of air holes in silicon with $r/a=0.195$	43

3-1	Calculated photonic band structures for (a) square 2D PC with air-holes of radius $r = 0.35a$, in a dielectric matrix with $\epsilon = 12$, and (b) triangular 2D PC with air-holes of radius $r = 0.4a$, in a dielectric matrix with $\epsilon = 12.96$. Insets: equifrequency contours for (a) $\omega_1 = 0.192$ and (b) $\omega_2 = 0.305$	45
3-2	Negatively refracted beam constructed from the wave vector diagram method. The bold arrow indicate the group velocity direction, while the thin arrow stand for the phase velocity direction. The gray polygon is the Brillouin zone while the black lines indicate the boundary of the irreducible Brillouin zone.	46
3-3	FDTD simulation of the real part of the magnetic field obtained performing the point imaging on a triangular photonic crystal slab made of air holes embedded in dielectric matrix at the normalized frequency $\omega = 0.192$ under TE polarization(H field parallel to the holes axis). The radius of the hole is $r = 0.35a$ while the relative dielectric constant of the matrix is $\epsilon_r = 12$	46
3-4	Negatively refracted beam constructed from the wave vector diagram method. The bold arrow indicate the group velocity direction, the thin arrow stand for the phase velocity direction, the red dashed circle is the air EFC whereas the blue circle indicates the crystal EFC. The gray polygon is the Brillouin zone while the black lines indicate the boundary of the irreducible Brillouin zone.	47
3-5	FDTD simulation of the real part of the electric field obtained performing the point imaging on a triangular photonic crystal slab made of air holes embedded in dielectric matrix at the normalized frequency $\omega = 0.305$ under TE polarization(E field parallel to the holes axis). The radius of the hole is $r = 0.4a$ while the relative dielectric constant of the matrix is $\epsilon_r = 12.96$	48

3-7	(a) Sketch of the slab obtained rotating, by an angle θ , a one dimensional PC having a unit cell made of two different dielectric materials $\epsilon_1 = 8.6$ and $\epsilon_2 = 1$. (b) and (c) equi-frequency contours at $\omega = 0.260$ (1^{st} band) and $\omega = 0.457$ (2^{nd} band) respectively, plotted in the first and in the repeated Brillouin zone, relatively to the crystal in (a); k_1 and k_2 are two wave vectors impinging the air-PC interface at two generic different angles γ_1 and γ_2 , whereas k_{1r} and k_{2r} are the wave vectors diffracted inside the crystal.	51
3-8	(a) Detail of the photonic crystal surface termination for the case with and without corrugation. (b) Comparison of the focus profiles (calculated via FDTD) produced by the slab with corrugation (blue line) and without corrugation (red line). (c) and (d) Transversal and lateral profiles respectively of the transmitted energy in a normalized scale. All the above profiles are taken along the lines (parallel and perpendicular to the PC surface) where the focused image exhibits its maximum. . .	52
3-10	(Color online) 3D spatial mapping of the point source signal transmitted by the alumina-air slab at $13.7175GHz$	55
3-11	In-plane spatial mapping of the measured electric field intensity ((a), (c), (e)) and phase ((b), (d), (f)) for the alumina-air PC at $7.800GHz$, $9.0825GHz$ and $13.7175GHz$ respectively.	55
3-12	Normalized transversal (a) and lateral (b) experimental profiles, taken at $13.7175GHz$ along the lines where the focused image exhibits its maximum, for the alumina-air superlens.	56
3-13	Normalized transversal (a) and lateral (b) experimental profiles, taken at $7.3505GHz$ along the lines where the focused image exhibits its maximum, for the alumina-plexiglas superlens.	57

3-14	Simulated (a) and measured (b) lateral profiles respectively for the focused image of a point source changing its position (d_{source}) normal to the surface of the alumina-plexiglass PC superlens	57
4-1	Periodic structure composed of infinite wires having radius r arranged in a cubic lattice of period a	60
4-2	Schematic of a closed ring (a) and split ring resonator (b).	63
4-3	Schematic of a split ring resonator made of two concentric rings.	64
4-4	Real part (continuous line) and imaginary part(dashed line) of the $\mu_{eff}(\omega)$	66
4-5	Equivalent circuitual model for the single split ring (a) an the double split ring (b).	67
4-6	Wave incident on a slab of thickness d . The meaning of the S-parameters (i.e. the complex transmission and reflection coefficients) is illustrated.	69
5-1	Example of a PC based chip provided with all the functions typical of a conventional electronic chip.	73
5-2	(a) Group velocity along ΓM direction versus frequency for three different lengths of PC sample. Solid black line represent the predicted behavior from band structure calculation. (b) Left y axis - group velocity dispersion of a CMM in a waveguide for different sample lengths compared with cw experiment result (red dot line). Slowest v_g of $c/50$ is obtained at 10.3 GHz in this configuration. Right y axis - Experimental and theoretical empty waveguide group velocity dispersion [2].	74
5-3	(a) Scanning electron microscope image and, (b), schematic band and group-index spectrum of a silicon PCW with respect to the absolute frequency [3].	75

5-4	Photonic-crystal nanocavity with a locally modulated waveguide width. (a) The design parameters, where a is the lattice constant, r is the hole radius and t is the slab thickness. (b) A SEM image of the device fabricated in a silicon photonic-crystal slab. (c) A near-field image acquired using a near-infrared camera from the top of the sample when a resonant wavelength light was injected through the input waveguide. The waveguide regions are indicated by the red squares [4]	75
5-5	(a) Schematic of the waveguide structure made up of an ordinary waveguide part and a tapered waveguide part having a metamaterial core. A wave packet is efficiently injected in from the ordinary waveguide to the left-handed part experiencing a spatial decomposition in to its frequency constituents. (b) Ray diagram of the light inside the tapered metamaterial core when experiencing the Goos-Hächen phase shift [5]	76
5-6	A sketch of a slab waveguide inside a parallel plate waveguide.	78
5-7	Parameter space (shaded area) for stopping light in a waveguide with (a) dielectric core (ϵ_D) and cladded with a negative permeability metamaterial ($\mu_M < 0$ and $\epsilon_M > 0$) and (b) dielectric core with $\epsilon_D = 8.6$ and cladded with a negative permeability metamaterial.	80
5-8	(a) SRR layout. (b) SRR unit cell. The dimensions are $w = 3mm$, $d = c = g = 0.33mm$. The unit cell size is	82
5-9	(a) Computed transmission and reflection coefficients. (b)-(c) The retrieved effective parameters ϵ and μ for SRR shown in Fig. 5-8	83
5-10	Phase index n_p as a function of thickness d for waveguide with core layer $\epsilon_D = 8.6$ and cladded with $\epsilon_M = 4.4$ and $\mu_M = 0.22$ at 8.57 GHz in the lossless case. The circle marks the location of zero group velocity	84
5-11	Phase index n_p as a function of thickness d when losses are introduced. The cladding has $\mu_M = -0.22 + i0.27$ and $\epsilon_M = 4.4 - i0.14$	84

5-12	Parameter space for stopping light in a waveguide with a dielectric core made $\epsilon_D = 8.6$ (red area) and a core made of air $\epsilon_D = 1$ (blue area) .	85
5-13	(a) Layout and (b) 3D unit cell of the SRR geometry used to in the experiment. (a) Transmission and reflection, (b) effective permeability and (c) effective permittivity parameters corresponding to the unit cell in (b).	86
5-14	(a) Comparison of the effective permeability for (a) the double split ring resonators shown in Fig. 5-8 and (b) the single SRR in Fig. 5-13. (c) Plot of the ratio of the real part and the imaginary part of the effective parameters shown in (a) and (b).	87
5-15	Real part of the effective permeability (a) and permittivity (b) for different values of the gap g	87
5-16	Real part of the effective permeability and permittivity for different values of the (a)-(b) ratio s/l , (c)-(d) metal with w and (e)-(f) radius of curvature r	88
6-1	3D illustration of the slow-light structure. The SRRs and the dielectric core (grey) are placed between two parallel metal plates. The top plate is not shown here.	89
6-2	(a) Spin coater with the wafer ready to be processed. (b) Mask and (c) machine used for the photolithography. (d) Wet etching step. (e) Stripping	91
6-3	(a) Wafer sample with the SRRs layout, (b) single stripe provided with gaps used to assemble the metamaterial slab in (c).	91
6-4	(a) Wafers with a CRR and SRR copper layout. (b) Transmission curve for the CRR slab (blue line) and SRR slab (red line), the inset shows a magnification of the curves around the magnetic resonance. .	92
6-5	(a) Transmission curves for corresponding to the different ring orientation showed in (b).	93

6-6	Measured (blue line) and simulated (red line) scattering parameter S_{21} in a normalized scale, corresponding to the metamaterial slab showed in Fig. 6-3(c).	94
6-7	(a) Measured scattering parameters for the case of parallel stripes arrayed along the x direction only with period l_x equal to a (green), $2a$ (red) and $3a$ (black). Scattering parameters measured for $l_z = 6a$ (b), $l_z = 2a$ (c) and $l_z = a$ (d). In the insets are the schematics of the arrayed slabs realized with interlaced stripes.	95
6-8	(a) Scattering parameters obtained measuring the transmission from a slab made with $l_x = l_z = a$ illuminated with a plane wave impinging the sample at different angles. (b) and (c) magnification of the resonance band highlighted in (a) respectively with red and green dotted lines.	96
6-9	Pictures of the planar waveguide having a cladding made of metamaterial cladding ($l_M = 40cm$, $w_M = 2.3cm$ and height $1cm$) and a core made of air. T and R indicate the position of the transmitting and receiving antenna.	98
6-10	Schematic of the experimental setup used to perform the pulsed measurements. A computer controlled microwave transition analyzer MTA modulates the signal generated from the synthesized sweeper SS and feeds, by a rectangular shaped pulse, two lines: A containing the metamaterial sample, and B which is used as a reference. The source is sent to A and B using a power beam splitter. Two isolator are inserted to avoid kill reflections. The two signals from A and B are then sent in the two MTA ports.	99
6-11	Measured values of the group index n_g over a range frequencies f . The different color of the curves correspond to different value of the core thickness d	100

6-12 Group index plotted versus the core thickness d for fixed frequencies.(a)
 n_g profile predicted by the model, (b) experimental values. 101

CHAPTER 1

Introduction

1.1 Electromagnetism of Complex Materials: Metamaterials

The understanding of materials properties has troubled scientists for centuries because it is not easy to give a detailed picture of what is behind the surface of matter. Scientific literature has shown extensively the manifold properties of diverse materials, but still the degree of freedom of the internal structure of materials are so many that analyzing them all is impossible.

Sometimes the macroscopic properties of a compound can be unexpectedly different from that of single elements. This is exemplified well with the simple properties of ice cream where the taste of the ice and the cream separately are different from the finished ice cream as a whole.

“*Metamaterial*” is an appropriate word for artificial materials that show unconventional macroscopic properties. During the past year the field of metamaterials has attracted large interest from the scientific community, most specifically because of its connection with the area of electromagnetism. Since the birth of the word “metamaterial” many attempts have been made to give a proper definition for it, for example the following:

Metamaterials are a new class of ordered nanocomposites that exhibit

exceptional properties not readily observed in nature. These properties arise from qualitatively new response functions that are: (1) not observed in the constituent materials and (2) result from the inclusion of artificially fabricated, extrinsic, low dimensional inhomogeneities .

However, regardless of the particular definition, which can differ depending on the given application of the metamaterials they have in common two basic and distinctive properties:

- they are not observed in the constituent materials,
- they are not observed in nature.

1.2 Classes of Metamaterials

The world of composite materials is so enormous that it can be categorized under many different classes, involving both natural and artificial materials. The following sections will identify some of the categories that find applications in the field of electromagnetism. However it is also worth mentioning that metamaterials have broader application in the field of acoustics [6] and cosmology [7].

1.2.1 Photonic Crystals

Photonic crystals (PC) are composite materials made of a unit cell obtained by alternating dielectric and/or metallic elements. They can be built by arranging a unit cell either with a periodic or aperiodic rule. A very straightforward analogy can be made with the electronic crystals that are made with a periodic arrangement of atoms. Photonic crystals are composed of elements called “atoms” which are repeated in space to form crystal *lattice*. Their physical properties can also be described in terms of band structures. In fact, as will be shown in the following chapters, their lattice properties are such that they can either prohibit the propagation of certain waves, or

allow the transport of energy for other frequencies. These unique features make them the best candidates for the building of *all-optical on a photonic chip*, in fact what makes PCs extremely interesting and attractive for photonic applications is that they provide a complete control over the propagation of electromagnetic waves. PCs can be included under the class of metamaterials because their behavior differs from that of each of the elements that they are assembled with, for example depending on the wavelength they can act as either a mirror or a transparent block. PCs also possess qualities that are not observed in nature, for example the *negative index of refraction* that will be discussed extensively in the next chapters.

1.2.2 Resonant Structures

A different type of composite material showing features not present in the basic constituent elements is a structure assembled by arranging resonant elements. What results from assembling resonant structures is magnetic response regardless of whether the basic elements are magnetic or not. In fact, the magnetic moment is generated from the current loops that circulate in each resonant element, whereas the overall magnetic response of the metamaterial originates from assembling them in a periodic structure. The highly non linear properties of these elements allow metamaterials to show negative permeability and act, for example, as an absorber in the same frequency range where the single “atoms” resonate. A possible way to achieve negative permeability is by using elements called *split ring resonators* (SRRs) [8] which take the shape a metallic ring provided with a gap which allows the necessary condition for resonance. The extraordinary properties behind these artificial materials have made them superior candidates for both realizing structures like cloaking devices [9], where it is necessary to have an overall a magnetic response with *negative permeability* as well as slowlight waveguides [10] which will be discussed in the following chapters.

1.2.3 Cut Wires

Another artificial structure showing extraordinary properties is the counterpart of the metamaterial made from resonant elements. In fact, if we consider a structure where the building block is a very thin metallic wire [11], it can be demonstrated, that the whole material behaves as a plasma characterized by a plasma frequency that is much lower than that of the bulk metals. And like metals, this metamaterial shows *negative permittivity* below the resonance frequency.

By assembling together resonant elements and cut wires, we obtain a metamaterial that shows *negative refractive index*, which in turn introduces us to the world of *left handed metamaterials*. This world was theorized by Russian physicist, Viktor Veselago, [12] who in 1967 first asked the question:

What happens in a material when both the permittivity and permeability are negative?

Veselago proposed that under such negative refractive index condition, the Snell law still apply, but in a reversed form, where the phase velocity and the group velocity are opposite to each other giving origin to the idea of left handed materials. Veselago's work remained unconsidered until recent years when scientists realized the enormous breakthrough of his work which gave birth to a sector of science of left-handed metamaterials that today gathers researchers from all over the world.

1.3 Diffractive and non Diffractive Metamaterials

The three types of artificial metamaterials discussed thus far can all be grouped under the class of metamaterials. Although they all have in common the two main properties of metamaterials, these being that they are not observed in the constituent materials and that they are not observed in nature, there are however substantial differences among them. While photonic crystals are *diffractive metamaterials*, and are suitable

for molding the flow of light only at frequencies for which the wavelength is of same order of magnitude of the unit cell, that is in a diffractive regime $\lambda \approx a$, structures assembled with resonant elements, cut wires, or both, show their metamaterial-like properties only in the condition of effective medium regime, when $\lambda \gg a$, and for this reason we label them *non-diffractive metamaterials*.

1.4 Propagation of Waves in Right-Handed and Left-Handed Substances

The permittivity ϵ , and the permeability μ are the basic entities that determine the way an electromagnetic wave propagates inside a matter. From the general form of the dispersion equation it is clear that they appear as the only parameters:

$$\left| \frac{\omega^2}{c^2} \epsilon_{ij} \mu_{ij} - k^2 \delta_{ij} + k_i k_j \right| = 0 \quad (1.1)$$

which for isotropic medium becomes

$$k^2 = \frac{\omega^2}{c^2} n^2 \quad (1.2)$$

with n being the index of refraction

$$n^2 = \epsilon \mu. \quad (1.3)$$

We must be very careful taking the square root of equation (1.4). If we neglect losses, ϵ and μ are both real numbers, and it can easily be seen from (1.2) and (1.4) that changing the sign to both of them makes no difference from the mathematical

point of view. As Veselago first pointed out [12], this can give rise to three different interpretations:

1. that the properties of substances are not affected by a simultaneous change of sign of ϵ and μ
2. that ϵ and μ both being negative might contradict some fundamental law of nature with the consequence that no substances with these characteristics can exist.
3. That ϵ and μ can be simultaneously negative and that substances with such attribute show unusual properties never seen in material where ϵ and μ are both positive.

As we will demonstrate in the coming sections, the third case is the one admitted by nature. To study the effect of ϵ and μ on the propagating waves it is convenient to start from the Maxwell equations and the constitutive relations in the time domain:

$$\nabla \times \mathbf{E} = -\frac{1}{c} \frac{\partial \mathbf{B}}{\partial t}, \quad (1.4)$$

$$\nabla \times \mathbf{H} = \frac{1}{c} \frac{\partial \mathbf{D}}{\partial t}, \quad (1.5)$$

$$\mathbf{B} = \mu \mathbf{H}, \quad (1.6)$$

$$\mathbf{D} = \epsilon \mathbf{E}. \quad (1.7)$$

For a plane wave in which all the quantities are proportional to $e^{i(kz - \omega t)}$ the above expression reduces to

$$\mathbf{k} \times \mathbf{E} = \frac{\omega}{c} \mu \mathbf{H}, \quad (1.8)$$

$$\mathbf{k} \times \mathbf{H} = -\frac{\omega}{c} \epsilon \mathbf{E}. \quad (1.9)$$

We see from (1.8) and (1.9) that if $\epsilon > 0$ and $\mu > 0$ then \mathbf{E} , \mathbf{H} and \mathbf{k} form a right-handed basis of vectors, whereas if $\epsilon < 0$ and $\mu < 0$ they behave as a *left-handed* set.

Moreover, from the expression of the Poynting vector,

$$\mathbf{S} = \frac{c}{4\pi} \mathbf{E} \times \mathbf{H} \quad (1.10)$$

we notice that the propagation direction of the vector \mathbf{S} does not depend on the sign of ϵ and μ . This implies that for right-handed materials, \mathbf{S} and \mathbf{k} share the same direction of propagation, as shown in Fig.1-1(a), while for left-handed substances, they travel in opposite directions(Fig.1-1(b)). Furthermore, since the phase velocity $\mathbf{v}_p = \frac{\omega}{|\mathbf{k}|} \hat{\mathbf{k}}$ propagates in the same way as \mathbf{k} we can assume that in the left-handed case the group velocity \mathbf{v}_g is opposite to the phase velocity, being \mathbf{v}_g the velocity at which the energy flux \mathbf{S} propagates.

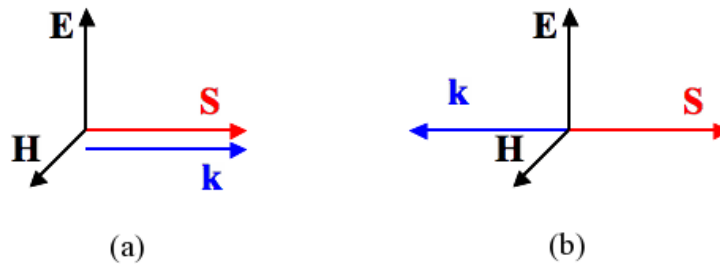


Figure 1-1: Schematic diagram of the vector basis formed by \mathbf{E} , \mathbf{H} , \mathbf{k} and \mathbf{S} when the propagation occurs in a right-handed(a) and in a left-handed media.

1.5 Refraction at the Boundary Between Right-Handed and Left-Handed Media

When a ray travels from one medium to another the following boundary conditions must be satisfied:

$$E_{t_1} = E_{t_2}, \quad H_{t_1} = H_{t_2} \quad (1.11)$$

$$\epsilon_1 E_{n_1} = \epsilon_2 E_{n_2}, \quad \mu_1 H_{n_1} = \mu_2 H_{n_2}. \quad (1.12)$$

These boundary conditions are valid whether or not the two media have the same right-ness. The first aspect that we note from (1.11) is that the direction of the tangential components do not depend on the right-ness of the two substances, whereas (1.12) shows that normal components have opposite signs if the two media have different right-ness. It is clear that Snell's law still holds but it must be given a more general form,

$$\frac{\sin \theta}{\sin \alpha} = n_{1,2} = \frac{p_2}{p_1} \left| \sqrt{\frac{\epsilon_2 \mu_2}{\epsilon_1 \mu_1}} \right|, \quad (1.13)$$

where p_1 and p_2 are two factors that represent the right-ness of the first and second medium. Figure 1-2 shows by ray diagram formalism Snell law at the interface between two media where both have $n > 0$, and the situation where one medium is right-handed $n < 0$ and the other is left-handed $n < 0$. The positive refracted wave lays in the opposite half plane with respect to the normal of the interface while in the second circumstance the negative refracted ray lays in the same half space of the incoming beam.

Fig. 1-3 shows how rays propagate when they travel, first, from a medium with positive refractive index $+n$, then, to a second medium which is long d with a negative

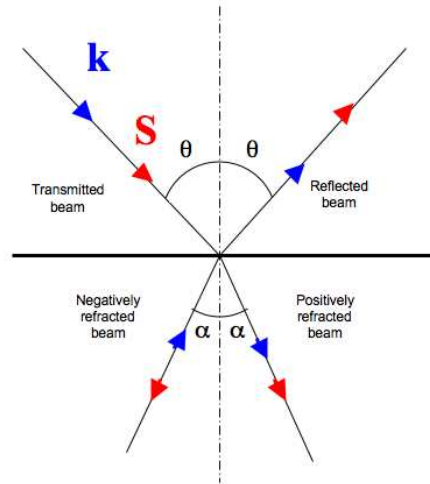


Figure 1-2: Ray diagram of the refraction effect at the interface between two positive media and a positive and a negative indexed media. Blue arrows indicate the phase velocity while the red arrows refer to the energy velocity.

refractive index $-n$, and then again into a medium with $+n$.

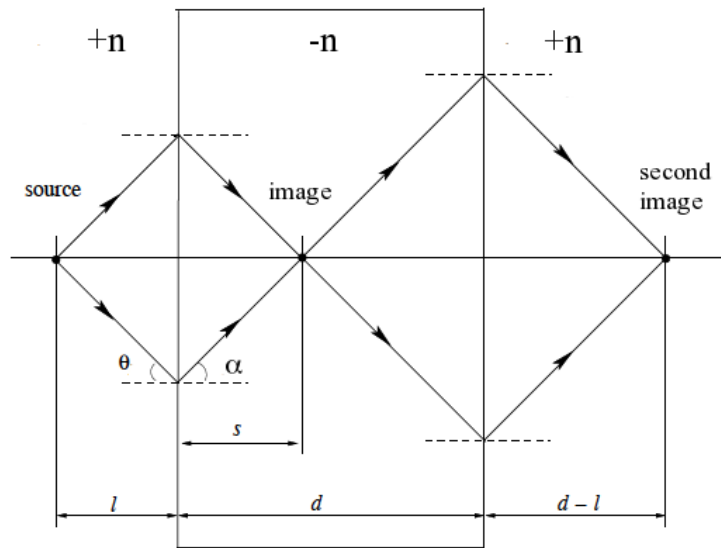


Figure 1-3: Ray diagram of the electromagnetic waves propagation through a negative refractive index slab having a width d and with a source located at a distance l from the first interface.

Under the circumstances where the absolute value of the indexes are the same and only the sign changes we do not observe any reflection because the reflection

coefficient is one. Such a system is capable of focusing radiation at a point in the image plane from a point source located at a distance of $l < d$ from the negative index slab. Basically, this object acts as a “strange” type of lens since the parallel rays coming from infinity are not focused on one point as in conventional lenses.

1.6 The Concept of “Perfect Lens”

Thanks to the concept of negative refraction it is now possible to introduce the *super-lens*, which is a new class of lenses that have performances capabilities far beyond any conventional lens. Sir John Pendry first proposed the remarkable idea of superlens in 2000 [13] as an extension of the work started thirty years earlier by Veselago [12]. Pendry suggested that the imaging capabilities of a lens can be greatly improved by recovering the evanescent waves that quickly decay in conventional materials. He discovered that this can be accomplished by means of a thin slab made of negative index materials. Under these circumstances it is possible to beat the Abbe-Rayleigh diffraction limit which is approximately the same size of the wavelength. In order to recognize the limitations of conventional lenses we have to look to the Fourier spectrum of the electric field excited from an infinitesimal electrical dipole

$$\mathbf{E}(\mathbf{r}, t) = \sum_{\sigma, k_x, k_y} \mathbf{E}_{\sigma}(k_x, k_y) e^{(ik_x x + ik_z z + ik_y y - i\omega t)} \quad (1.14)$$

where z coincides with the axis of the lens. From Maxwell’s equations we know that

$$k_z = +\sqrt{\frac{\omega^2}{c^2} - k_x^2 - k_y^2} \quad \text{for} \quad \frac{\omega^2}{c^2} > k_x^2 + k_y^2. \quad (1.15)$$

which represents the propagating component of the wave, while

$$k_z = +i\sqrt{k_x^2 + k_y^2 - \frac{\omega^2}{c^2}} \quad \text{for} \quad \frac{\omega^2}{c^2} < k_x^2 + k_y^2. \quad (1.16)$$

which is the evanescent component of the field that dies in the far field zone and does not contribute to the imaging formation. Pendry demonstrated that under the condition of $\epsilon = -1$ and $\mu = -1$ the energy is perfectly transmitted in the $+z$ direction while in the medium it is required that

$$k'_z = -k_z = -\sqrt{\frac{\omega^2}{c^2} - k_x^2 - k_y^2} \quad (1.17)$$

leading to an overall transmission for both TE and TM polarization [13] equal to

$$T = e^{-ik_z d}. \quad (1.18)$$

From (1.18) it is clear that for waves traveling through a medium with $\epsilon = -1$ and $\mu = -1$ the evanescent components are amplified, leading to an image which possesses both the contributions of transmitted and evanescent fields. To summarize, Fig.(1-4) is drawn schematically to illustrate the differences between a conventional lens and a superlens. Normally, to have good resolution in a conventional lens we can adjust the aperture which conveys rays with large θ (see Fig.1-4(a)), however, the image resolution is still limited to the size of the wavelength because the evanescent components are totally decayed in the far field (Fig.1-4(b)). With the superlens we can in principle recover the entire spectrum of information of the source, the transmitted (Fig.1-4(c)) and the evanescent (Fig.1-4(d)) components, the latter being amplified and not suppressed as in traditional lenses.

Furthermore, a superlens does have a significant difference from a conventional

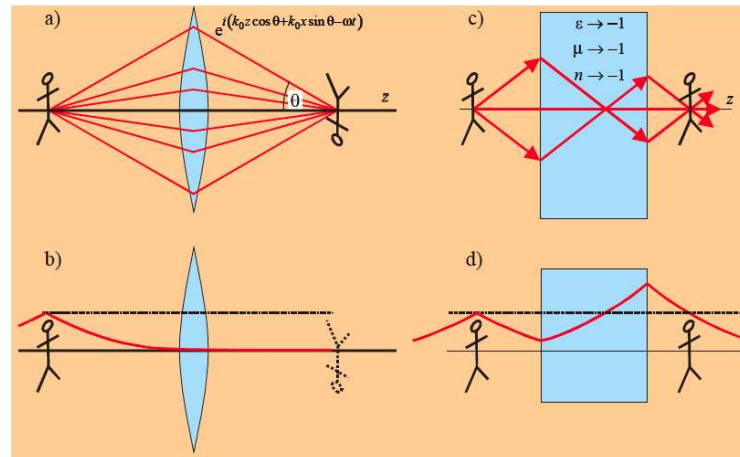


Figure 1-4: (a) Image formation due to the contribution of the propagating waves and evanescent waves respectively in conventional lens (a,b) and superlens (c,d) [1]

lens. Imaging by a traditional lens, as described by Newton’s formula, is one in which the focal length is an important parameter, and also, where the magnification depends on the relative distance of an object from the lens (see Fig.1-5(b)) resulting only in a 2D image on the focal plane.

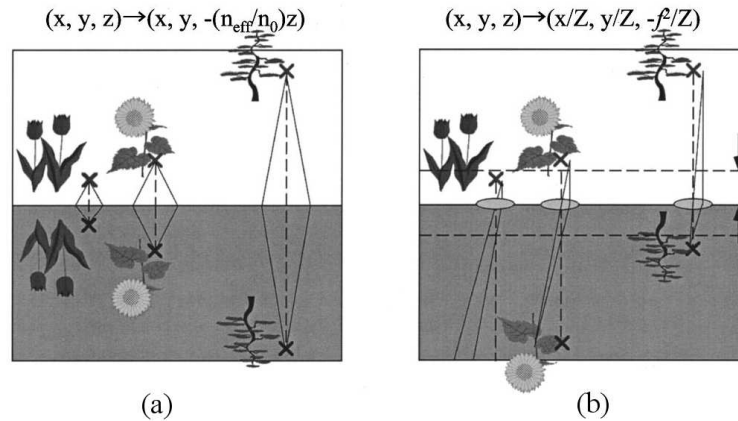


Figure 1-5: Schematics of imaging by a negatively-refractive medium(a) and imaging by a conventional lens(b).

On the contrary, a negative refractive system can produce a 3D image due to the mirror-inversion transformation $(x, y, z) \rightarrow (x, y, -\beta z)$ where $\beta = \text{abs}(n_{eff}/n_0)$ [14], which differs from Newton’s formula (see Fig.1-5(a)). Moreover the conventional lens imaging has a definite principal axis, whereas the imaging by the superlens has

translational symmetry in the boundary plane which produces a lack of optical axis, and in this sense, the latter is closer to imaging by a mirror. To this end the apparent difference between a superlens and a mirror is that the former produces a real image, but the latter only produces a virtual image.

Fig.1-6 shows an example of an open cavity realized by assembling together right-handed and left-handed structures. This structure is very interesting because it shows that in principle negative refraction makes it possible to achieve an open cavity without reflecting walls.

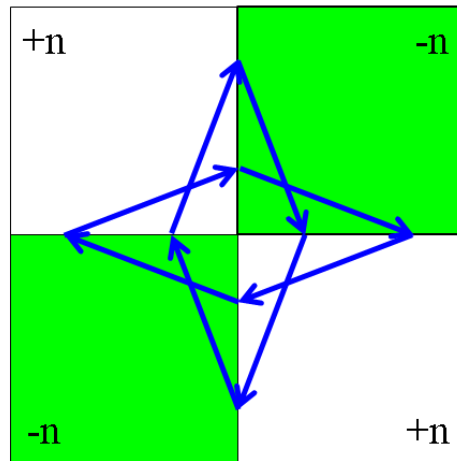


Figure 1-6: Schematic diagram of light propagation in an open cavity made with negative and positive refractive media.

1.6.1 Dispersion in Negative Refractive Index Metamaterials

An important point that needs to be mentioned is that the simultaneous negative ϵ and μ can be realized only when there is frequency dispersion. We will demonstrate that this is a necessary condition that nature imposes in order to achieve negative refraction.

If we write the following relation

$$W = \epsilon \mathbf{E}^2 + \mu \mathbf{H}^2 \quad (1.19)$$

we see that when there is neither frequency dispersion nor absorption we cannot have $\epsilon < 0$ and $\mu < 0$ since the total energy would be negative. However, when there is frequency dispersion, we can rewrite the previous expression in the following form,

$$W = \frac{\partial(\epsilon\omega)}{\partial\omega} \mathbf{E}^2 + \frac{\partial(\mu\omega)}{\partial\omega} \mathbf{H}^2. \quad (1.20)$$

In order for the energy W to be positive it is required that,

$$\frac{\partial(\epsilon\omega)}{\partial\omega} > 0, \quad \frac{\partial(\mu\omega)}{\partial\omega} > 0. \quad (1.21)$$

The relations (1.21) do not mean that ϵ and μ cannot be simultaneously negative, but in order for them to hold their property they must be frequency dependent.

1.7 Application with Metamaterials

1.7.1 The Invisible Cloak

The potential of metamaterial based structures cannot be understood without connecting them to some real life application. Recently the most intriguing achievement that scientists have been trying to pursue is the electromagnetic cloak. Nowadays the possibility to hide objects at optical wavelength is representing one of the most important results for military applications. Most probably in the near future the invisible cloak, which now is only in fiction, could become reality.

One of the most promising way to realize a invisibility is by using the concept of

transformation optics which basically offers the opportunity for the control of the electromagnetic waves. A wide variety of conventional devices can be designed by the transformation optical approach, including beam shifters [15], beam bends [16], beam splitters [15], focusing and collimating lenses [17], and structures that concentrate electromagnetic waves [18]. Within all these properties the most compelling one is without any doubt that of a medium that can conceal objects from detection by electromagnetic waves. In the transformation optical approach, one imagines warping space so as to control the trajectories of light in a desired manner. As an example of this approach, a cloak can be designed by performing a coordinate transformation that squeezes the space from within a sphere to within a shell having the same outer radius.

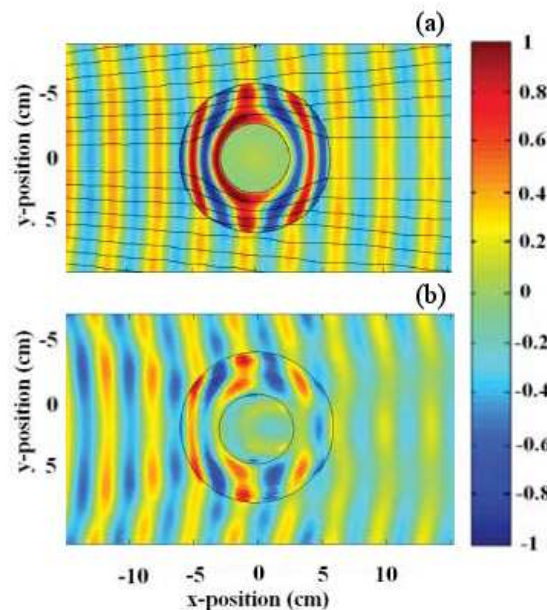


Figure 1-7: Snapshots of time-dependent, steady-state electric field patterns, with stream lines [black lines in (a)] indicating the direction of power flow (i.e., the Poynting vector). The cloak lies in the annular region between the black circles and surrounds a conducting Cu cylinder at the inner radius. The fields shown are (a) the simulation of the cloak with the exact material properties, (b) the experimental measurement of the cloaked conducting cylinder.

Waves do not interact with or scatter from the core because it is simply not part of the transformed space. The form invariance of Maxwell's equations implies

that the coordinate transformation can instead be applied to the permittivity and permeability tensors, yielding the prescription for a medium that will accomplish the desired functionality. The resulting medium is highly complex, being anisotropic and with spatial gradients in the components of the permittivity and permeability tensors.

In 2006 *Smith et al.* [9] proofed for the first time that a cylindrical structure made with split ring resonators can hide an object placed in its center. The experiment was performed at microwave wavelength placing the sample inside a parallel plate waveguide and sensing the phase and amplitude of the propagating field all over the region embedding the sample. Results are shown in Fig. 1-7. The most important aspect to highlight is that thank to the transformation optics the electromagnetic field is not influenced by the cylindrical object but it warps around it keeping the phase unaltered.

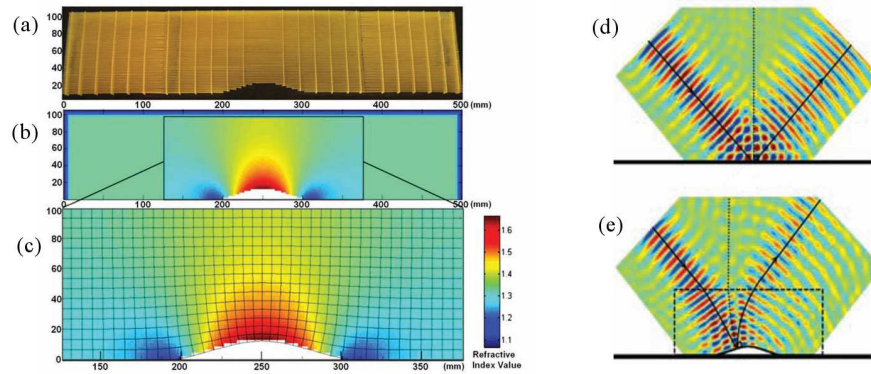


Figure 1-8: The transformation optical design for the ground-plane cloak. The metamaterial cloak region is embedded in a uniform higher index background with gradients introduced at the edges to form impedance matching regions. (a) Photograph of the fabricated metamaterial sample. (b) Metamaterial refractive index distribution. The coordinate transformation region is shown within the box outlined in black. (c) Expanded view of the transformation optical region in which the mesh lines indicate the quasi-conformal mapping. Measured field mapping (E-field) of the ground, perturbation, and ground-plane cloaked perturbation. The rays display the wave propagation direction, and the dashed line indicates the normal of the ground in the case of free space and that of the ground-plane cloak in the case of the transformed space. (d) Collimated beam incident on the ground plane. Collimated beam incident on the ground-plane cloaked perturbation.

Cloaking wise the same group also developed a ground plane cloak which thank

to the non resonant nature of the constitutive elements shows a very broad band [19]. The principle is still based on the properties of transformation optics where a conformal coordinate transformation is applied to Maxwell's equations to obtain a spatially distributed set of constitutive parameters that define the cloak. Unlike the previous case where there is a suppression of the scattering at the cylinder to air interface, here the metamaterial structure is built in a way that the parameters space distribution eliminates the backscattering due to the presence of the object to be hidden and restores the reflected waves in the same way as if the object was not there. In Fig. 1-8(a) is shown the metamaterial structure while in figure (b) and (c) are shown respectively the effective parameter distributions and the quasi conformal mapping obtained from the transformations. In the experimental results in Fig. 1-8(e) they show that a plane wave impinging the object, which is under the white bump region, is not affected and it gets reflected as there was no object on the ground plane(Fig. 1-8(d)).

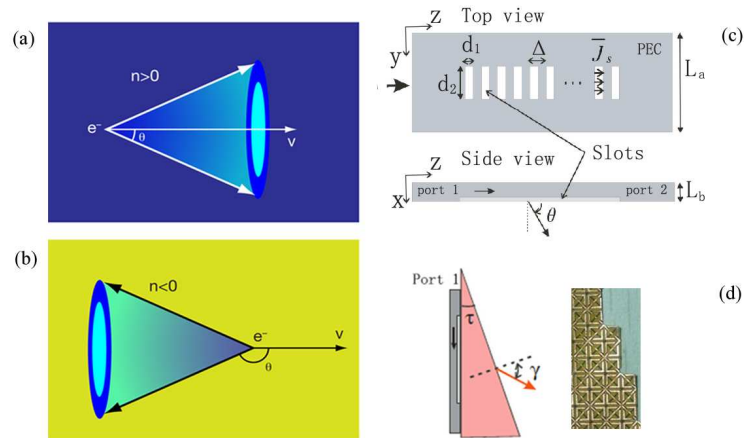


Figure 1-9: (a) Schematic of Čerenkov radiation in a conventional natural medium with positive refractive index, in which the radiation falls in a cone in the forward direction. (b) Schematic of backward Čerenkov radiation in a left-handed medium, showing the reversed cone. (c) Schematics of the phased dipole array. (d) experimental setup with the metamaterial wedge placed on top of the phased dipole array and next to it is the picture of the metamaterial array made with split ring resonators and cut wires.

1.7.2 Inverse Phenomena in Left-Handed Metamaterials

Beside the above applications that find most of their interests in the military field, the exotic properties of left handed medium leads to inverse phenomena like negative refraction, inverse Doppler effect, backward Čerenkov radiation and negative radiation pressure. Very recently *Xi et al.* [20,21] proofed unambiguously for the first time the Čerenkov radiation at microwave frequencies. The Čerenkov radiation is generated when charged particles such as electrons travel through a dielectric medium with a speed greater than the phase velocity of the light in the medium. Hence electromagnetic radiation is emitted that falls into a cone fanning out in the forward direction (see Fig. 1-9(a)). Since the phase velocity in a left-handed medium is negative, i.e., opposite to the direction of the energy flow, the cone angle is obtuse and hence the radiation cone is facing toward the backward direction, as shown in Fig. 1-9(b).

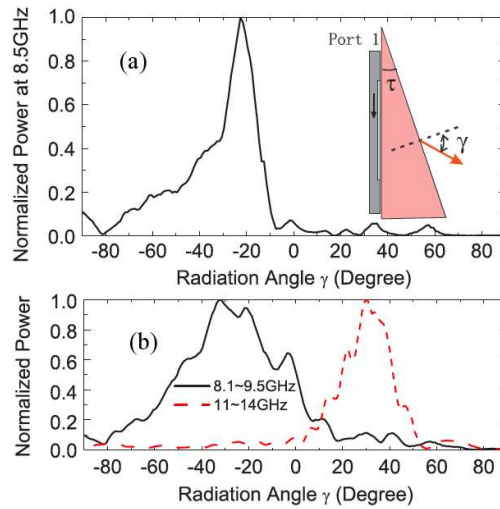


Figure 1-10: (a) Radiation power diagram for the Čerenkov effect observed at 8.5GHz. The inset show the experimental setup where the source is in port 1. (b) Sum of the radiation power in each angle in the negative band (solid line) and positive band (dashed line).

The radiated power of a fast-moving charged particle at microwave frequency is very small. In order to improve the radiated power, a phased dipole array was used to model the charged particle. In fact they showed that this modeling is reasonable and that the current density of a moving charge can be emulated by the current

density generated by a phased dipole array. The schematic of such array is illustrated in Fig. 1-9(c) where a parallel plate waveguide provided with a certain number of rectangular slots on one of the plate is used to model the fast moving charged particles. The radiated field couples then with a metamaterial wedge placed at the exit of the slots (see Fig. 1-9(d)). The metamaterials structure is realized by a periodic array of resonant elements and cut wires deposited on a dielectric substrate. The inverse Čerenkov effect is expected to take place in the region where the metamaterial shows a negative refractive index, while the conventional Čerenkov radiation happens when $n > 0$. For the above metamaterial the measured effective refractive index is positive in the range $[8.1 - 9.5]GHz$ while being negative in the range $[11 - 14]GHz$.

In Fig. 1-10(a) is shown that radiated power measured at $f = 8.5GHz$ exits the metamaterial wedge at the negative angles resulting in a backward Čerenkov radiation. In Fig. 1-10(b) are plotted the sums of radiated powers over the corresponding frequency ranges measured at each angle for the case of a forward and backward radiation. These results unambiguously proof the inverse Čerenkov effect in negative index materials.

Part I

Diffractive Metamaterials

CHAPTER 2

Photonic Crystals

2.1 Introduction

Before the advent of photonic crystals a number of phenomena in solid state physics were analyzed borrowing the formalism from the field of optics and electromagnetism. By contrast, the opposite situation has rarely occurred, and only on few occasions have optics and electromagnetism borrowed concepts and theoretical method from solid state physics. In the same way as the periodicity of solid state crystals determines the energy bands and the conduction properties of electrons, the periodical structuring of photonic materials at wavelength scale has turned out to be one of the most viable approaches toward the control of the energies and the fluxes of photons occurring in these materials. The analogy between electronic waves and electromagnetic waves is a mere consequence of the formal relation between the Schrödinger's equation for electronic wavefunctions and Maxwell's equations for electromagnetic waves. Indeed, leaving aside the spins of the particles, a harmonic electromagnetic wave in a dielectric lossless medium satisfies Eq. 2.2, which formally is analogous to the equation ruling the wave function for an electron with mass m in a potential V (Eq. 2.1):

$$\nabla \times [\nabla \times \mathbf{E}(\mathbf{r})] = \frac{\omega}{c^2} \epsilon_r(\mathbf{r}) \mathbf{E}(\mathbf{r}) \quad (2.1)$$

$$\nabla^2 \psi(\mathbf{r}) = -\frac{2m}{\hbar} (E - V(\mathbf{r})) \psi(\mathbf{r}) \quad (2.2)$$

The spin difference between the photons, which are bosons, and electrons, which are fermions, results in different statistics for the energy state populations, and also explains that these two equations are of a different nature: the equation for photons is vectorial whereas the equation for electrons is scalar. What is important to note in order to make the comparison between the two systems more straightforward is that, by comparing the above two equations, it turns out that the dielectric permittivity $\epsilon_r(\mathbf{r})$ is for photons the analogue of the potential $V(\mathbf{r})$ for electrons. Furthermore, in analogy with the electronic band gaps of semiconductors, it then becomes intuitive that periodic variation of $\epsilon_r(\mathbf{r})$ may result in the formation of photonic band gaps. This means that for a certain range of wavelength light beam incident on this material will be totally reflected, regardless the polarization and direction of propagation.

2.2 Photonic Crystals Properties

Photonic crystals are artificial structures assembled by arranging a unit cell according to a certain periodic or quasi-periodic rule. For this dissertation we will only consider periodic photonic crystals made out of only dielectrics. A PC is characterized by a relative dielectric function $\epsilon(\mathbf{r})$ assumed to be real and periodic along all the three directions of space.

Fig. 2-1 shows the three possible types of periodic PCs, one-dimensional, two dimensional and three dimensional photonic crystals, depending on the properties of the dielectric function $\epsilon(\mathbf{r})$.

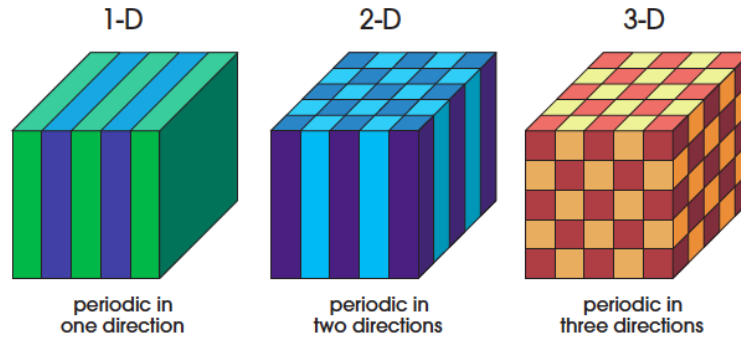


Figure 2-1: Schematic of a 1D, 2D and 3D photonic crystal. The different color in each drawing indicate different dielectric materials.

When studying the electromagnetic properties of these periodic structures we assume the following approximation for the dielectric materials

1. the fields strength are small enough so that we are in the linear regime, and second order effects can be neglected,
2. the material is assumed macroscopic and isotropic so that $\mathbf{E}(\mathbf{r}, \omega) = \epsilon(\mathbf{r}, \omega)\mathbf{H}(\mathbf{r}, \omega)$
3. the material is not dispersive in frequency, $\epsilon(\mathbf{r}, \omega) = \epsilon(\mathbf{r})$
4. $\epsilon(\mathbf{r})$ is considered purely real and positive.

Assuming all this approximation to be valid we can write the following constitutive relation for the materials,

$$\mathbf{D}(\mathbf{r}) = \epsilon_0 \epsilon_r(\mathbf{r}) \mathbf{E}(\mathbf{r}) \quad (2.3)$$

$$\mathbf{B}(\mathbf{r}) = \mu_0 \mathbf{H}(\mathbf{r}) \quad (2.4)$$

where μ_0 is the vacuum permeability. $\mu(\mathbf{r})$ was omitted because for most of the materials in use the corresponding value is very close to unity. The electric field \mathbf{E} and the magnetic field \mathbf{H} satisfy the Maxwell's equations [22] which here are represented in the symbolic notation,

$$\nabla \times \mathbf{E}(\mathbf{r}) - i\omega\mu_0\mathbf{H}(\mathbf{r}) = 0 \quad (2.5)$$

$$\nabla \times \mathbf{H}(\mathbf{r}) + i\omega\epsilon_0\epsilon_r(\mathbf{r})\mathbf{E}(\mathbf{r}) = 0 \quad (2.6)$$

$$\nabla \cdot \mathbf{E}(\mathbf{r}) = 0 \quad (2.7)$$

$$\nabla \cdot \mathbf{H}(\mathbf{r}) = 0. \quad (2.8)$$

We assume for the equations (2.5-2.8) harmonic solutions of the form,

$$\mathbf{H}(\mathbf{r}, t) = \mathbf{H}(\mathbf{r})e^{-i\omega t}, \quad \mathbf{E}(\mathbf{r}, t) = \mathbf{E}(\mathbf{r})e^{-i\omega t}. \quad (2.9)$$

Inserting (2.9) in (2.5-2.8) we have the fundamental two equations,

$$\nabla \times \left[\frac{1}{\epsilon(\mathbf{r})} \nabla \times \mathbf{H}(\mathbf{r}) \right] = \frac{\omega^2}{c^2} \mathbf{H}(\mathbf{r}) \quad (2.10)$$

with $c = 1/\sqrt{\epsilon_0\mu_0}$ and $\omega/c = k_0 = 2\pi/\lambda_0$, where c , k_0 and λ_0 represent the speed of light, the wave number, and the wavelength of light in vacuum respectively.

Eq. (2.10) is called the **master equation**, and together with equations (2.7) and (2.8), it is possible to retrieve all the information about the magnetic field \mathbf{H} , whereas the electric field \mathbf{E} is obtained from Eq. (2.6). The equation (2.10) can be written as an eigenvalue problem as follows,

$$\hat{\Theta}\mathbf{H}(\mathbf{r}) = \left(\frac{\omega}{c}\right)^2 \mathbf{H}(\mathbf{r}) \quad (2.11)$$

where

$$\hat{\mathbf{O}}\mathbf{H}(\mathbf{r}) \triangleq \nabla \times \left[\frac{1}{\epsilon(\mathbf{r})} \nabla \times \mathbf{H}(\mathbf{r}) \right] \quad (2.12)$$

is an Hermitian operator [22].

2.3 Scaling Properties of the Maxwell Equations

A very interesting feature of Maxwell's equations is that they are *scale invariant*. This means that the same solution is valid in presence of a contraction or expansion of all the distances. Lets consider for example an eigenmode $\mathbf{H}(\mathbf{r})$ of frequency ω with a dielectric function $\epsilon(\mathbf{r})$ and recall the master equation (2.10)

$$\nabla \times \left[\frac{1}{\epsilon(\mathbf{r})} \nabla \times \mathbf{H}(\mathbf{r}) \right] = \frac{\omega^2}{c^2} \mathbf{H}(\mathbf{r}). \quad (2.13)$$

Suppose we want to investigate about the harmonic modes for a dielectric function $\epsilon'(\mathbf{r}) = \epsilon(\mathbf{r}/s)$, which represent a compressed version of the original function and where s is a scale parameter. If we change the variable in (2.13), using $\mathbf{r}' = s\mathbf{r}$ and $\nabla' = \nabla/s$ we get

$$s\nabla' \times \left[\frac{1}{\epsilon(\mathbf{r}'/s)} s\nabla' \times \mathbf{H}(\mathbf{r}'/s) \right] = \left(\frac{\omega}{cs} \right)^2 \mathbf{H}(\mathbf{r}'/s). \quad (2.14)$$

But $\epsilon(\mathbf{r}'/s)$ is none other than $\epsilon'(\mathbf{r}')$ which gives the following expression for the master equation with a compressed version of the dielectric function:

$$\nabla' \times \left[\frac{1}{\epsilon'(\mathbf{r}')} \nabla' \times \mathbf{H}(\mathbf{r}'/s) \right] = \left(\frac{\omega}{cs} \right)^2 \mathbf{H}(\mathbf{r}'/s). \quad (2.15)$$

This is again the master equation but with a mode profile $\mathbf{H}'(\mathbf{r}')$ and frequency $\omega' = \omega/s$. The essence of this new form of the master equation is that the new mode profile and corresponding frequency can be obtained by simply rescaling the old mode profile at its frequency. This result is of a considerable practical importance, where the solution of a problem at a given wavelength provides the solution at all other scales. In fact, often due to manufacturing limitations is not possible to study the optical properties of certain structures at the desired wavelength, but considering (2.15) it is possible to test the same geometry at larger scales, for example, at microwave wavelengths.

2.4 Photonic Band Structure

From solid state theory [23] it is well known that the propagation of electronic waves in periodic crystals obeys the Bloch theorem. The same is true for electromagnetic waves propagating in periodic photonic crystals. The mode of a three-dimensional periodic system are Bloch states that can be labeled by a Bloch wave vector $\mathbf{k} = k_1\mathbf{b}_1 + k_2\mathbf{b}_2 + k_3\mathbf{b}_3$ where \mathbf{k} lies in the Brillouin zone (BZ). Each value of the wave vector \mathbf{k} inside the Brillouin zone identifies an eigenstate $\hat{\Theta}$ with frequency $\omega(\mathbf{k})$ and an eigenvector of the form,

$$\mathbf{H}_{\mathbf{k}}(\mathbf{r}) = e^{i\mathbf{k}\cdot\mathbf{r}}\mathbf{u}_{\mathbf{k}}(\mathbf{r}), \quad (2.16)$$

where $\mathbf{u}_{\mathbf{k}}(\mathbf{r})$ is a periodic function on the lattice: $\mathbf{u}_{\mathbf{k}}(\mathbf{r}) = \mathbf{u}_{\mathbf{k}}(\mathbf{r} + \mathbf{R})$ for all lattice vectors \mathbf{R} . If we now insert the Bloch state (2.16) in to the master equation (2.10) we have,

$$\hat{\Theta}\mathbf{H}_{\mathbf{k}}(\mathbf{r}) = \left(\frac{\omega(\mathbf{k})}{c}\right)^2 \mathbf{H}_{\mathbf{k}}(\mathbf{r}) \quad (2.17)$$

$$\nabla \times \frac{1}{\epsilon(\mathbf{r})} \nabla \times e^{i\mathbf{k}\cdot\mathbf{r}} \mathbf{u}_{\mathbf{k}}(\mathbf{r}) = \left(\frac{\omega(\mathbf{k})}{c}\right)^2 e^{i\mathbf{k}\cdot\mathbf{r}} \mathbf{u}_{\mathbf{k}}(\mathbf{r}) \quad (2.18)$$

$$(i\mathbf{k} + \nabla) \times \frac{1}{\epsilon(\mathbf{r})} (i\mathbf{k} + \nabla) \times \mathbf{u}_{\mathbf{k}}(\mathbf{r}) = \left(\frac{\omega(\mathbf{k})}{c}\right)^2 \mathbf{u}_{\mathbf{k}}(\mathbf{r}) \quad (2.19)$$

$$\hat{\Theta}\mathbf{u}_{\mathbf{k}}(\mathbf{r}) = \left(\frac{\omega(\mathbf{k})}{c}\right)^2 \mathbf{u}_{\mathbf{k}}(\mathbf{r}) \quad (2.20)$$

where we have defined a new Hermitian operator that depends on \mathbf{k} :

$$\hat{\Theta} \triangleq (i\mathbf{k} + \nabla) \times \frac{1}{\epsilon(\mathbf{r})} (i\mathbf{k} + \nabla) \times . \quad (2.21)$$

From the eigenvalue problem in the Eq.(2.20) we can calculate the function \mathbf{u} and the mode profile subject to the transversality condition $(i\mathbf{k} + \nabla) \cdot \mathbf{u}_{\mathbf{k}} = 0$ and to the periodicity condition $\mathbf{u}_{\mathbf{k}}(\mathbf{r}) = \mathbf{u}_{\mathbf{k}}(\mathbf{r} + \mathbf{R})$. Thanks to the periodic boundary conditions we can limit the problem to the single unit cell of the PC. This will lead to a discrete spectrum of eigenvalue [22]. From the solution of this problem we get the modes supported by the PC, they are a family of continuous functions $\omega_n(\mathbf{k})$, indexed in order of increasing frequency by the band number n and $\omega_n(\mathbf{k})$ is called the *band structure* of the photonic crystal. From the information contained in the band structure we can predict the propagation of light inside a PC for every \mathbf{k} , as will be shown in the next paragraphs. Fig.2-3(a) shows a schematic of a 2D PC consisting of dielectric rods embedded in air arranged in a square lattice array, whereas Fig. 2-3(b) shows the corresponding band structures plotted over the irreducible Brillouin zone for TE and TM polarization.

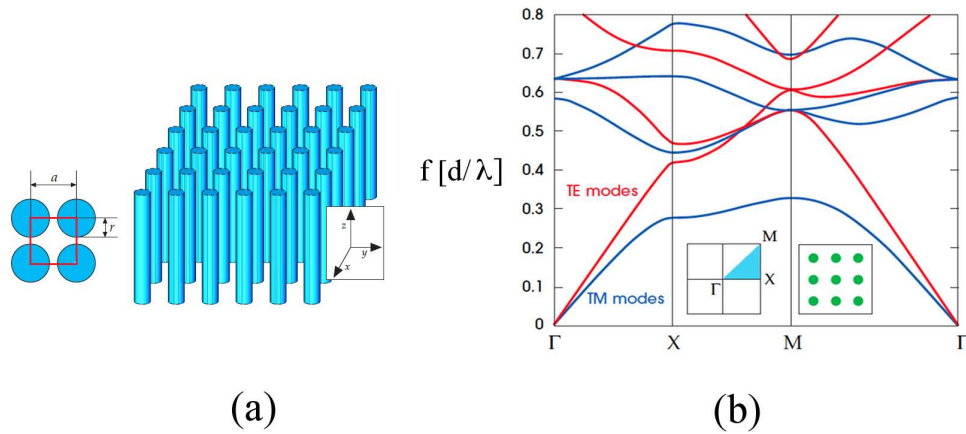


Figure 2-2: 3D schematic of a square photonic crystal realized with dielectric rod in air, (b) corresponding photonic band structure for the TE and TM mode.

2.5 Wave Vector Diagram

The next step in the study on the propagation of light inside photonic crystals is the analysis of the wave vector diagram [24]. The diagram is powerful and straightforward method of calculating the direction of the refracted waves inside PCs. In this frame we will refer mainly to 2D systems, and in some case, to 1D photonic crystals because they represent the main types of lattices that have been investigated for this thesis. The most important part of the wave vector diagram are the equifrequency surfaces (EFSs) that apply to the frequency of operation. For the 2D case the surface reduces to a contour (EFC). These contours consist of all allowed propagation modes in wave vector space that exist in the PC system for a certain frequency. As already noted in the previous section all of the information about the supported modes are contained in Eq.(2.20). One, or a multiple set of contours can be relevant for a certain frequency, depending on the number of bands corresponding to the frequency of interest. For the sake of simplicity we focus the analysis on case with only one band corresponding to the frequency of interest. Figure 2-3(a) represents a three dimensional plot of the function $\omega_n(\mathbf{k})$ for a triangular lattice over the first Brillouin zone. Each different surface represents the locus of all the allowed states for single band number n . Whereas Fig.2-3(b) shows the equifrequency contours in the (k_x, k_y)

space corresponding to the first band of the function plotted in Fig.2-3(a).

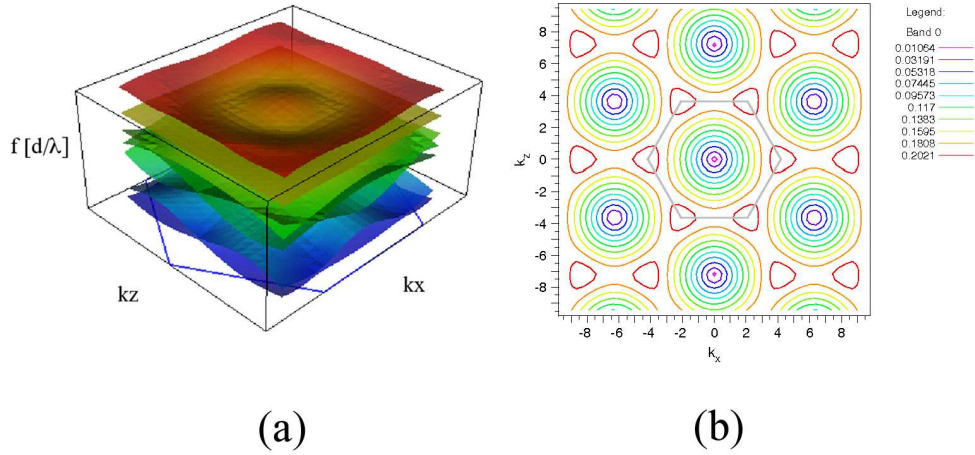


Figure 2-3: (a) Band surface for a photonic crystal with an triangular unit cell, (b) corresponding equifrequency contour limited to the first band only.

The following steps are use to construct the wave vector diagram:

- draw the EFC in the repeated zone scheme
- draw a line perpendicular to the interface that represents the conservation of the tangential component $k_{//} = \frac{\omega}{c} \sin \theta_{inc}$, where θ_{inc} is the angle respective to the normal of the air-PC interface. This represent the *construction line*
- record all intersections between the construction line and the EFC
- fold the intersections which fall outside the first BZ, back to the first BZ, by adding an appropriate reciprocal lattice vector.
- record all the resulting wave vector values in the first BZ, including, the original intersections in the first BZ, and those that were folded back from the higher zones*.

*The reason behind the folding process relates to the nature of the Bloch wave [25]. In fact it can be shown that a Bloch wave that correspond to two wave vectors \mathbf{k}_1 and \mathbf{k}_2 are essentially equivalent if $\mathbf{k}_2 - \mathbf{k}_1 = \mathbf{G}$, with \mathbf{G} being a reciprocal lattice vector. For consistency the Bloch wave is expressed in terms of the wave vector \mathbf{k} (called fundamental wave vector) lying in the first BZ

- determine the actual direction of propagation of the refracted wave by deciphering the sign of the slope of the frequency band under investigation which is given by $\mathbf{k} \cdot \nabla\omega$

The knowledge of the sign of the slope is of fundamental importance in determining the direction of propagation of the energy and can be retrieved from the direction of the energy velocity \mathbf{v}_e . In fact, it can be proved that the \mathbf{v}_e is equal to the group velocity \mathbf{v}_g [24]. Since the group velocity is given by $\nabla_{\mathbf{k}}\omega$ this implies that \mathbf{v}_g is normal to the EFS at certain point in \mathbf{k} space, and points toward increasing frequencies. Moreover, due to the causality constraint, amongst all the possible directions for the refracted signals, we select only that points away from the source. It should be noted, that different wave vector intersections that correspond to the same fundamental wave vector, yield only to one refracted beam, and for this reason are called “equivalent”, whereas different wave vector points that result in the first zone after the folding process, give rise to different beams. Additionally refracted beams can be categorized according to their order. A beam corresponding to an intersection lying in the first BZ, which did not need folding, is a zeroth-order beam called a “transmitted” beam, while beams stemming from intersections in the higher zones, which were subsequently folded back to the first zone, are classified as higher-order beams.

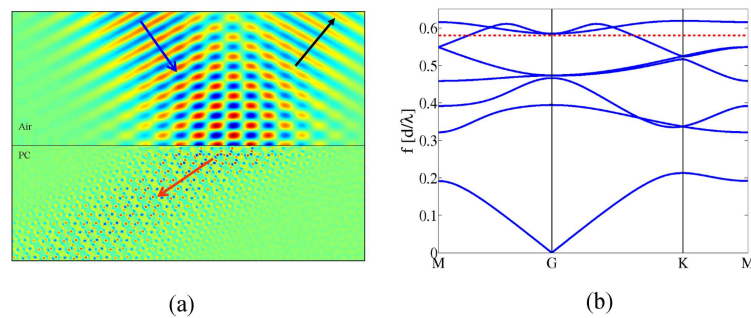


Figure 2-4: (a) FDTD simulation of a plane wave propagating inside a photonic crystals and experiencing negative refraction. (b) Band structure corresponding to the PC analyzed in (a), the red dashed line indicate the frequency at which the plane wave propagates.

In figure 2-4(a) we see a Finite Difference Time Domain (FDTD) [26] simulation of the refraction phenomena occurring in a PC made of air holes embedded in a dielectric matrix, and arranged in a triangular lattice. In Fig. 2-4(b) the corresponding PC band structure is shown, where the red dashed line indicates the normalized frequency of the propagating signal at $f=0.58$. The incident beam (blue arrow) comes with $\theta_{inc} = 30^\circ$ with respect to the normal of the air-PC interface, while, as it is evident from Fig.2-4(a) the transmitted beam (indicated by a red arrow), seems to bend the “wrong” way. The origin of this apparently non-regular behavior is in the diffractive nature of photonic crystals and can be explained by the use of the wave vector diagram shown in Fig. 2-5(a). The green dashed line represents the construction line. It intersects points A and B of the EFC in the first zone (gray hexagon) and also intersects points A_2 , B_2 , A_3 and B_3 of the EFCs in the higher-order zones. According to the steps outlined above, we fold points A_2 , B_2 , A_3 and B_3 back to the first zone by adding $\mathbf{G}_n = n\mathbf{G}_{0y}$ (where $n=-2$ for points A_2 and B_2 and $n=+2$ for A_3 and B_3). It is important to note that they all fold back to points A and B. Since the corresponding band has a negative slope, (see Fig. 2-4(b)), the wave vector corresponding to point A has energy velocity \mathbf{v}_e pointing away from the source, while point B has \mathbf{v}_e pointing toward the source implying that only point A contributes to a propagating beam which is a transmitting beam (indicated with a black arrow in Fig.2-5(a)). This phenomenon is clear evidence of the **negative refraction** effect occurring in the PC structure as the transmitted wave has the fundamental wave vector and the energy velocity antiparallel: $\mathbf{v}_e \cdot \mathbf{k} < 0$. The negativeness of the propagating wave is in the left-handed nature of the vector basis formed by \mathbf{E} , \mathbf{H} and \mathbf{k} .

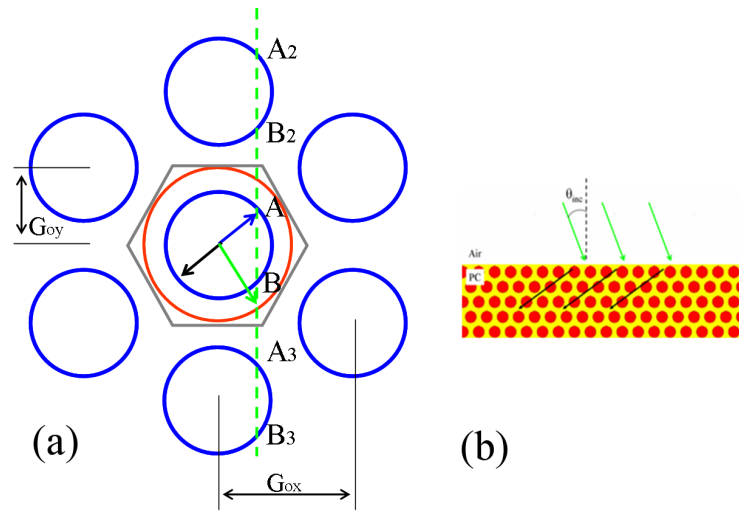


Figure 2-5: (a)EFC plotted in the first and repeated Brillouin zones at $f=0.58$ for a TM mode (H field parallel to the rod axis) and the corresponding (b) ray diagram of the diffraction in the corresponding photonic crystal made of air holes (red colored) arranged in a triangular array and embedded in dielectric having $\epsilon_r = 12.96$ (yellow colored).

2.6 Diffraction Phenomena: from Electronic Crystals to Photonic Crystals

As already mentioned earlier there are a variety of phenomena present in Electronic crystal that have been proved also in the case of PC. One of this is the Pendellösung effect, which is a relatively well known effect of Dynamical Diffraction Theory (DDT), a rigorous formalism accounting for multiple scattering effects that are especially important in Xray, electron and neutron diffraction from perfect crystals [27]. Since the original formulation of the diffraction theory from Ewald [28], the Pendellösung effect was predicted as a periodic exchange of energy between interfering wave-fields. The German term comes from the formal analogy between the mechanical system composed by coupled pendula and the optical problem, where many waves contribute to the optical field. In this formal analogy, pendulum is the counterpart of the wave, whereas the temporal dependence of the mechanical problem corresponds to the spatial dependence in the considered optical problem [29]. The requirement of high

quality crystals explains why the first experimental observation of the Pendellösung effect has been obtained in 1959 only in X-ray measurements [30], and some years later in neutron diffraction [31, 32]. A decade ago using the coherence of third generation synchrotron beams, Pendellösung fringes produced by a plane wave exiting a Si crystal have been recorded [33]. Only recently the Pendellösung effect has been investigated theoretically also in 2D photonic crystals [34, 35], using both analytical and numerical methods as a function of the PC contrast index, beam incident angle, and light polarization. Moreover, this study has been extended to opal 3D photonic crystals, where the dependence of diffraction intensity as a function of the layers number has been investigated using a scattering matrix approach [36]. On the experimental side the properties of microwave diffraction in periodic structures have been reported in literature by measuring the pattern of backscattered waves in two dimensional artificial dielectric media [37]. Recently, the Pendellösung effect has been detected also in the optical regime in volume holographic gratings, observing the oscillatory behavior of the angular selectivity of the diffracted light [38].

2.6.1 The Pendellösung Effect in Photonic Crystals

The Pendellösung effect in PCs can be understood as a beating phenomenon due to the phase modulation between coexisting plane wave components, propagating in the same direction. The coexistence is possible because such wavevectors are associated to two adjacent bands that are overlapped, for a given frequency, in correspondence of suitably chosen PC parameters.

In our case the 2D PC consists of dielectric cylinders in air (dielectric permittivity $\epsilon_r = 8.6$) arranged in a square geometry and having $r/a = 0.255$, where r is the cylinder radius and a is the lattice constant. If TE polarization (electric field parallel to the rods axis) is considered, an overlap occurs between the fourth and the fifth mode for a normalized frequency $\omega_n = fa/c = a/\lambda = 0.722$, as shown in Fig. 1. Moreover, the crystal orientation is fixed such that the normal at its surface is along

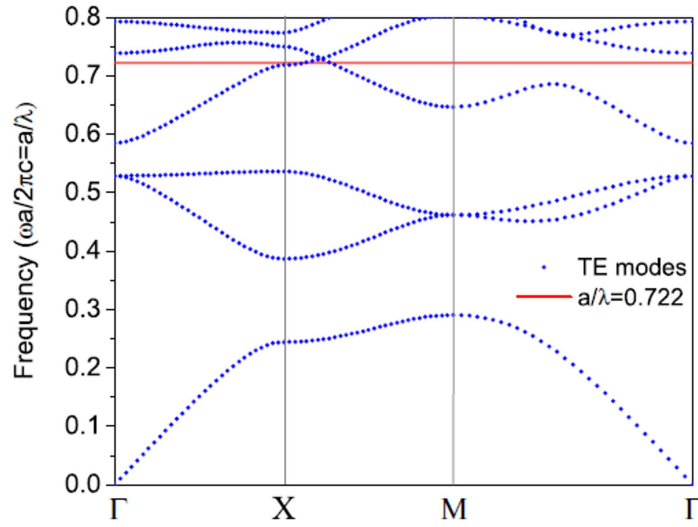


Figure 2-6: The band structure of the square-lattice PC for the TE polarization. The red line represents the normalized frequency $\omega_n = 0.722$ at which the Pendellösung effect takes place

the XM direction. Hence all possible wavevectors excited into the PC will have the same tangential component lying on XM. The Pendellösung phenomenon is analyzed in this context for an incident wavevector that satisfies the Bragg law [34,35]. In Fig. 2-7 we show in the reciprocal space the first Brillouin zone and the corresponding symmetry points for the square lattice PC under study. Considering the reciprocal lattice vector that enforces the momentum conservation oriented along ΓX in the first Brillouin zone, the Bragg law is fulfilled when the projection of the incident wavevector coincides with ΓX , so that k_h is the diffracted wavevector whereas k_i is the incident one. Using the dispersion surfaces (or EFSs), that represent the loci of propagating wavevectors for a fixed frequency, we are then able to evaluate the relevant parameters of the beating effect. The wavevectors inside the PC are determined by the intersection between each EFS and the XM direction. Amongst the different intersections, only wavevectors having group velocity oriented inside the crystal - 2-7 in opposite direction respect to the external normal to the incident surface - will be effectively excited. Consider for instance the contribution of the incident wave: there is an interference between two excited components, with the respective wavevectors

pointing in two different directions. This produces a spatial periodic modulation along the wavevectors difference vector $\Delta\mathbf{k}$. The modulation distance in the real space along the PC normal direction is therefore $\Lambda_0 = 2\pi/\Delta\mathbf{k}$.

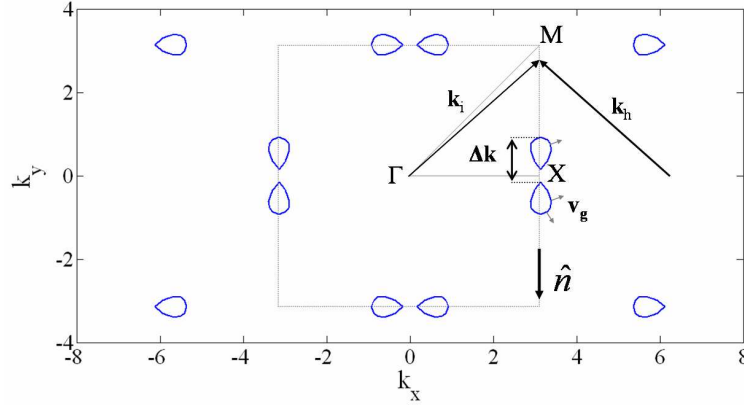


Figure 2-7: The reciprocal space with the first Brillouin zone (dotted line) and symmetry points for the square-lattice PC. The contours for the normalized frequency $\omega_n = 0.722$ are plotted. Arrows indicate the directions of group velocity \mathbf{v}_g , whereas \hat{n} shows the normal to the incident surface.

The same effect occurs also for the diffracted wave, giving rise to a spatial modulation with the same length but 180° out-of-phase in respect to the previous case. As a consequence of the Pendellösung effect, the intensity I at the exit surface is harmonically modulated as a function of the thickness t [34]. When t is an even multiple of half the Pendellösung distance, the beam at the exit surface is parallel to the incident beam, forming a positive angle respect to the PC normal. On the other hand, when t is an odd multiple of Λ_0 the beam at the exit surface is completely directed along the Bragg diffracted direction, forming a negative angle respect to the PC normal. Denoting by $+$ and $-$ the two possible directions at the exit surface, this is summarized by:

$$t = 2m \frac{\Lambda_0}{2} \quad \Rightarrow \quad \max(I_+) \quad (2.22)$$

$$t = (2m - 1) \frac{\Lambda_0}{2} \quad \Rightarrow \quad \max(I_-) \quad (2.23)$$

where $m = 1, 2, \dots$. Forcing the Pendellösung distance Λ_0 be an even number of the lattice constant a , Eqs. (2.22) and (2.23) holds for any number n of PC rows. In particular, $\Lambda_0 = 4a$ ensures that the intensity maxima of the exit waves changes periodically if n is even, and that the energy beam equally splits between positive and negative direction if n is odd. From the EFSs analysis, assuming a TE polarization, we found that an angle $\theta_i = 43.8^\circ$ and a normalized frequency $\omega_n = 0.722$ for the incident wave satisfy both the Bragg law and the peculiar condition $\Lambda_0 = 4a$.

2.6.2 Experimental Observation of the Pendellösung Effect at Microwave Frequencies

Experimentally the Pendellösung effect was never studied before at microwave frequencies, and moreover no one has never measured the electric field distribution of the transmitted field at the exit of the crystal and the field distribution inside the PC. This work represents part of this PhD research activity and has also been published on an international journal [39].

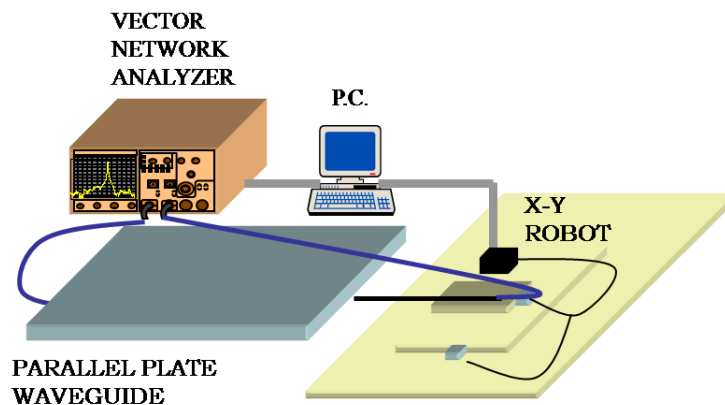


Figure 2-8: Schematics of the basic setup used to perform measurements at microwave frequencies.

In figure 2-8 is shown the basic experimental setup used to perform measurements

at microwave frequencies. This schematics is very general and is suitable for the study of every type of planar structure by mean of scattering parameters characterization [40]. Basically, the sample is treated as a two-ports system and is placed inside the parallel plates waveguide and is illuminated at one port by a monopole antenna connected to a Vector Network Analyzer (VNA) whereas the transmitted signal is measured at the exit port by a second antenna that moves along the x - y plane thanks to an automatic stage controlled by a computer. The VNA performs the measurement over a range of frequencies then elaborates the measure and provides the amplitude and phase of the signal at each frequency.

The experimental results are obtained on 2D PCs having a different number of rows inserted in a waveguide. First, the electromagnetic wave transmitted by the periodic structure is measured at the exit of the PC for different crystal thickness and its spatial distribution is shown. Then, the periodic modulation of the intensity of the diffracted waves with respect to n is reported. Finally, a comparison along selected directions inside the photonic crystal between the electric field distribution measured and simulated using a Finite Difference Time Domain (FDTD) method is presented. Measurements are carried out by placing alumina rods with nominal permittivity $\epsilon_r = 8.6$, radius $r = 0.4\text{cm}$ and height $h = 1\text{cm}$ in a square geometry with $r/a = 0.255$ ($a = 1.57\text{cm}$) sandwiched in an aluminum parallel-plate waveguide terminated with microwave absorbers (see Fig. 2-9). Since the loss tangent of alumina is extremely small at the frequency relevant for this work ($\tan\delta < 10.4$), dielectric losses can be neglected. Due to the presence of metallic plates acting as mirrors, current lines that are perpendicular to the plates can be considered as infinitely long, as stated by the well-known mirror theorem. For the same reason the electric fields produced by these currents are constant along the same direction and thus the whole system acts as a 2D structure.

The microwave photonic crystal is built in the shape of a 38.5cm wide slab (25

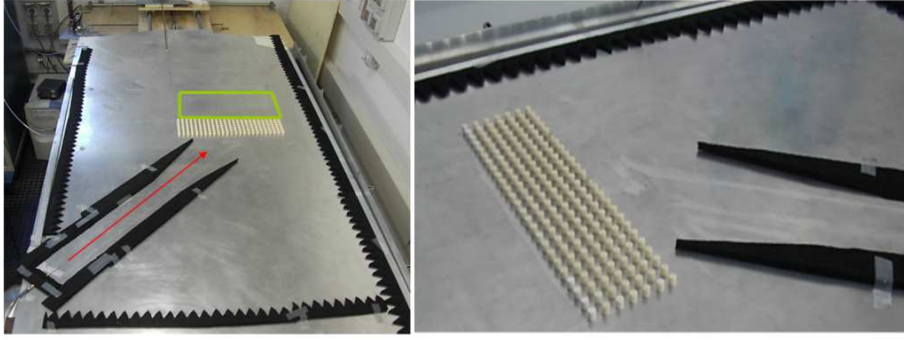


Figure 2-9: Pictures of the open parallel plate waveguide with the photonic crystal and the guiding structure made of absorbers used to generate a directive beam.

rod columns), with a thickness that can be varied adding or removing rows. A dipole antenna is used as source, oriented to produce an electric field parallel to the rods axis and operating at the frequency of $13.784GHz$, in order to reproduce the same normalized frequency $a/$ of the theoretical model. Due to the waveguide characteristics, the TEM mode only can propagate up to $15GHz$. The maps of the real part of the electric field are collected by using a HP8720C Vector Network Analyzer and another dipole antenna as a detector, that moves along the waveguide plane using an $x-y$ step motor. The thickness dependence has been investigated based on the observation of the beams at the exit of the crystal-air interface. We focused our analysis on structures with a number of rows n ranging from 1 to 10.

Figure 2-10 shows the scheme of the measurement. Particular attention has been paid to the source characteristics. The incident beam has to be as collimated and directive as possible, ideally consisting of a single wavevector only. To realize the experiment, we inserted in the parallel plate waveguide two parallel microwave absorber stripes, having the role to “guide” the electromagnetic wave. The channel is $50cm$ long and $10cm$ wide, with tapered sidewalls in order to ensure a good matching condition at the air-to-absorber interface. The field generated by the dipole source is centered into the absorbers channel. To limit the diffraction at the exit of the waveguide, a phenomenon that strongly reduces the beam directivity, the channel

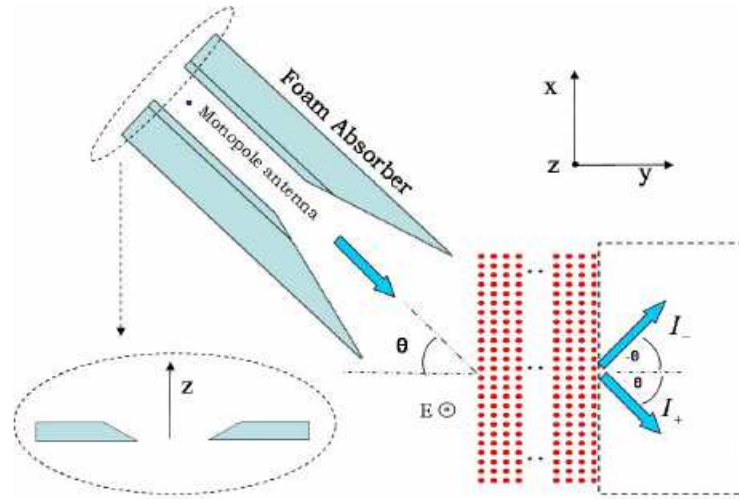


Figure 2-10: Schematic layout of the experiment carried out on the square-lattice PC slab having 25 rods columns and a number of rows n varying from 10 to 1. The dashed line box represents the scanned area during the measurements

section closer to the PC interface has been shaped into a triangular profile. All these solutions provide a beam source having transmission properties close to ideal ones. The incoming beam is then oriented at 43.8° respect to the normal to the PC interface, whereas the two arrows exiting the surface in both the forward diffracted and diffracted directions represent the signals transmitted through the wave guide and the crystal. Furthermore, the angle that describes the outcoming waves is the same as the source. In the image plane, a tiny dipole antenna (radius $\sim 0.6mm$) scans an area $20cm$ long and $40cm$ wide contiguous to the crystal-air interface, in steps of $4mm$ in both x and y direction. As said before, for a fixed frequency and source orientation the intensities I_+ and I_- reach a maximum or a minimum value depending on the difference between the wavevectors inside the crystal and, in turn, on the crystal thickness.

In Figs.2-12(a)-(e) the real part of the electric field experimentally detected in different crystal configurations is mapped in the image plane, using a normalized scale. In Fig.2-12 (a) the spatial distribution is shown for the case $n = 10$. The maps for the other cases of crystals with an even number of rows ($n = 8, 6, 4, 2$) are presented in Figs.2-12(b), (c), (d), (e), respectively. Starting the data analysis from

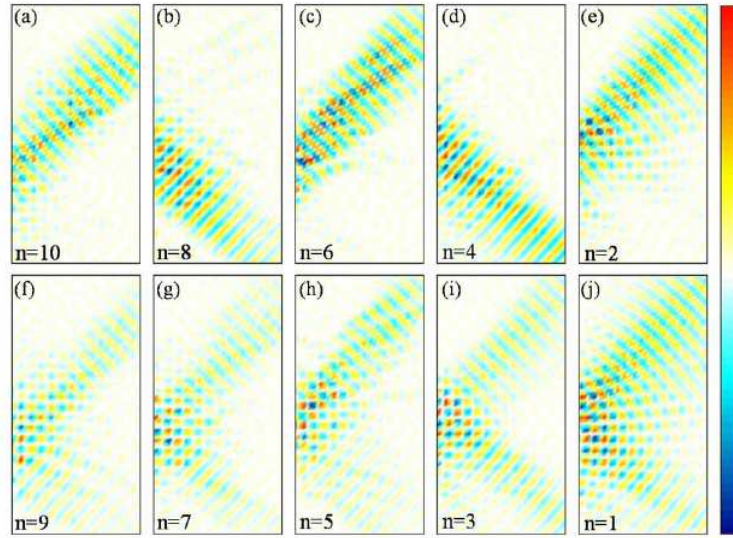


Figure 2-11: (a)-(e): mapping of the measured electric field (real part) in a normalized scale for even n ; (f)-(j): mapping of the measured electric field (real part) in a normalized scale for odd n

the crystal consisting of 10 rows, that is an odd multiple of $\Lambda_0/2$, in this case the beam, as expected, is fully transmitted in the diffracted direction. On the contrary, when the PC consists of 8 rows, the beam exits its surface in the forward diffracted direction (Fig.2-12(b)). By reducing the thickness down to 2 rows for any even n , the transmitted beam alternatively bends from the negative to the positive direction, as shown in Figs.2-12(c)-(e). Other beams related to higher order of diffraction are negligible. Measurements clearly show therefore that for an even number of rows the involved energy is almost entirely concentrated along one exit direction only. It is also clear from the images that the transmitted field propagates along regular and periodic equiphase planes, in agreement with numerical simulations. Let us now analyze the experimental results for crystals having an odd number of rows. In this case, according to the periodical modulation predicted for the field intensity at the exit surface, the thickness is such that at the crystal-air interface the transmitted energy is equally divided in both positive and negative directions. This is shown in Fig.2-12(f)-(j): the electromagnetic beam in the image plane actually splits in two rays having approximately the same intensity, with equiphase planes clearly evident

in both directions. It is worth noting that the case with $n = 1$ (Fig.2-12(j)) reduces to the well known Bragg grating. The fundamental feature of the Pendellösung effect is the spatial periodic modulation of the transmitted field amplitude with the crystal thickness.

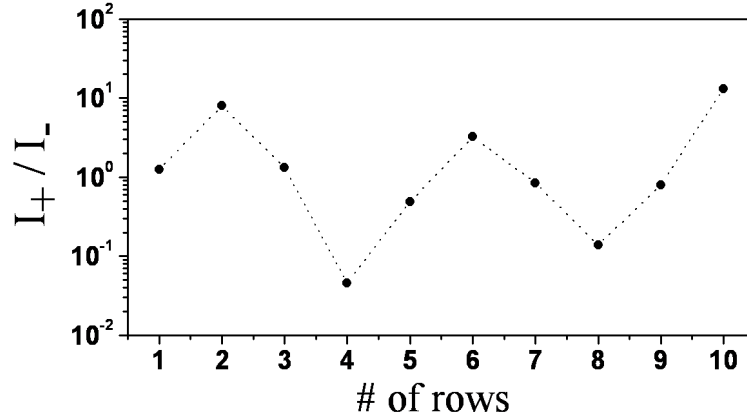


Figure 2-12: The measured electric field intensity ratio I_+/I_- for all the crystal configurations considered. The case of 10 rows corresponds to the maximum thickness $t = (10a + 2r) = 16.4cm$.

We then compared the electric field maximum intensity measured along the two different (positive and negative) transmitted directions as a function of the photonic crystal row number n (thickness). As shown in the Fig.2-12 using a semi-log scale, the intensity ratio I_+/I_- changes periodically, being approximately equal to 1 for any odd n , and exhibiting pronounced maxima and minima alternatively for any even n . We also evaluated the electromagnetic field distribution inside the PC slab. FDTD simulations are performed considering a plane monochromatic incident wave having a rectangular transverse profile. The propagation in the slab is of course well different from that in free-space since Bloch modes will be excited and therefore a strong modulation of the electromagnetic field is expected. In particular, in the Pendellösung phenomenon, the positively and negatively refracted components of the incident wave interfere each other inside the crystal and give rise to a periodic exchange of energy. This translates in a spatial modulation of the field intensity, as it can be clearly seen when the dielectric contrast is not very high [35]. In the

case discussed here the strong Bloch modulation makes the visualization of the wave pattern quite difficult. Moreover, when the contrast is high, the intensity maxima inside the rods mask the distribution in the outside region. Therefore, for the sake of clarity, we have suppressed the field inside the dielectrics. Results are shown in Fig. 2-13(a). It is worth mentioning that the spatial modulation observed in the crystal does not affect the energy direction, which remains normal to the PhC interface. To compare the numerical simulations with experimental data we have then measured the internal field along selected directions normal to the PhC interface. Particular attention has been paid to ensure that the detector antenna moves perfectly parallel to the dielectric rods.

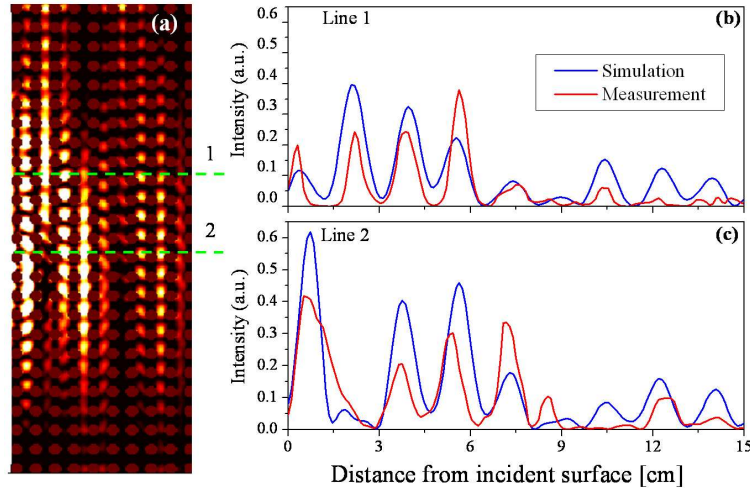


Figure 2-13: (a) FDTD simulation of the propagation pattern inside a crystal consisting of 10 rows of the $13.784GHz$ plane wave modulated by a rectangular profile and incident at an angle of 43.8° across the XM interface; (b) and (c): electric field intensity distribution (blue dashed lines) along line 1 and 2 respectively compared with the experimental results (red solid lines)

Figures 2-13(b) and 2-13(c) shows the simulated longitudinal profile of the field intensity along two different lines, (1) and (2) respectively, and the corresponding experimental results properly rescaled. In spite of the strong field modulation, the presence of peaks and valleys centered in different positions along the PhC normal direction and corresponding to different minima and maxima in the wave energy on the two longitudinal lines is evident, as expected by the theory. Besides that,

the decrease in the intensity as far as the electromagnetic wave propagates inside the crystal reflects the energy radiated from the finite-size PhC. This can be also observed in Fig. 2-13(a).

2.6.3 Application: Polarizing Beam Splitter

In Eqs.(2.22) and (2.23) it was shown that the energy at the exit of the PC can be periodically modulated by varying the crystal thickness t which is a function of the Pendellösung length Λ_0 . Given a certain crystal geometry, Λ_0 is a function of the polarization, of the normalized frequency and the PC filling ratio r/a . We can exploit this properties in order to realize a polarizing beam splitter [35]. In fact since Λ_0 is different for TE and TM polarization if we force the following rule for the thickness

$$t = 2m \frac{\Lambda_{0TE}}{2} = (2m - 1) \frac{\Lambda_{0TM}}{2} \quad (2.24)$$

we obtain a behavior where the TE wave is positively refracted while the TM wave is negatively refracted. In figure2-14 are shown the FDTD simulation for both the TE(a) and TM(b) mode. The simulations are performed at the normalized frequency $\omega_n = 0.413$ on a PC made of dielectric rods arranged in a square geometry with a filling ratio $r/a = 0.195$ while the incoming beam impinges the crystal at 20.6° .

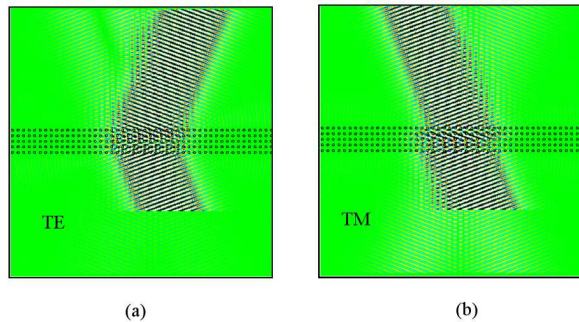


Figure 2-14: FDTD simulation for TM (a) and TE polarization (b). The incident wave ($\omega = 0.413$) has a Gaussian profile impinges at an angle 20.6° over a PC square lattice of air holes in silicon with $r/a=0.195$.

CHAPTER 3

Superlensing in Photonic Crystals

3.1 Introduction

In the second chapter we introduced the concept of John Pendry's superlens, however, we did not describe how such a structure could be created in practice. The properties of photonic crystals make it possible to achieve an arbitrary refractive index for the control and the propagation of light [14]. In fact, as shown in the previous sections, by exploiting the diffraction properties of PCs for a fixed frequency of operation, we can design the shape of the equifrequency surface in order to get the desired angle of refraction, and also achieve negative refraction. The superlensing properties of PCs have been studied mostly for the case of 2D photonic crystals, whereas, few efforts have been made to that of 1D PCs. In the following chapter of this dissertation we will outline the imaging concepts behind 2D PCs, and then focus our attention to how this can be achieved in 1D structures.

3.2 Superlensing in 2D Photonic Crystals

To our knowledge, negative refraction in 2D PCs generally occurs under two conditions. The first, as proposed by Notomi [14] is when the EFC of the PC is rounded, causing its radius to shrink as the frequency nears to the band gap. This is common for frequencies above the first band located near the Brillouin-zone center (Γ point),

where the wave vector and the group velocity are antiparallel. The second condition, lies in frequencies where the EFC is hyperbolic-like, and the normal components of wave vector and group velocity are parallel, which usually occurs near a Brillouin-zone corner farthest from the center (Γ point) [41]. The main differences between these two approaches have been studied extensively, [42, 43] and here we will highlight the most important aspects.

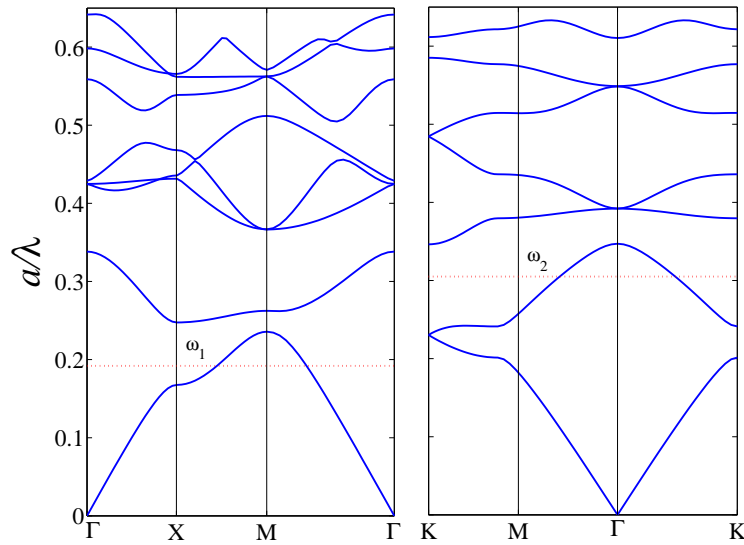


Figure 3-1: Calculated photonic band structures for (a) square 2D PC with air-holes of radius $r = 0.35a$, in a dielectric matrix with $\epsilon = 12$, and (b) triangular 2D PC with air-holes of radius $r = 0.4a$, in a dielectric matrix with $\epsilon = 12.96$. Insets: equifrequency contours for (a) $\omega_1 = 0.192$ and (b) $\omega_2 = 0.305$.

Figure 3-1 are represents the shape of the band structure for a square 2D PC with air-holes in a dielectric matrix (Fig. 3-1(a)), as well as that for a triangular 2D PC with air-holes in a dielectric matrix (Fig. 3-1(b)). First, let's investigate how to achieve negative refraction-like behavior in the case where the 2D PC is square. From figure 3-1 we see that in the first band, which for convention we can label as the 0^{th} band, the frequency surface has a convex shape in the vicinity of the M point, and for this reason the group velocities point inward. Under this condition, when a PC is oriented with the normal to the surface along the ΓM direction, only one mode will be excited when an incoming plane wave illuminates the structure (see red bold arrow

in Fig.3-2), and in this case we have realized negative refraction. Most importantly, it is necessary to point out that we have achieved negative refraction without having negative group velocity, since for this band $\mathbf{k} \cdot \partial\omega/\partial\mathbf{k} \geq 0$.

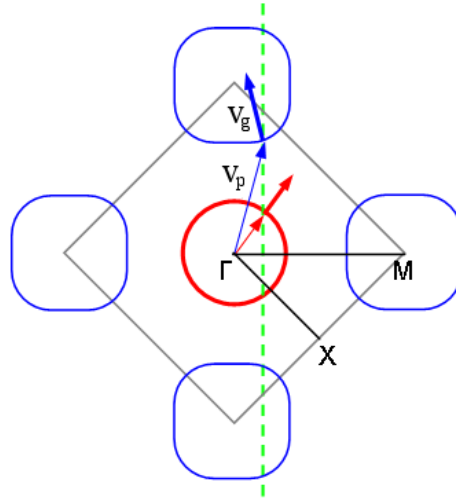


Figure 3-2: Negatively refracted beam constructed from the wave vector diagram method. The bold arrow indicate the group velocity direction, while the thin arrow stand for the phase velocity direction. The gray polygon is the Brillouin zone while the black lines indicate the boundary of the irreducible Brillouin zone.

Figure 3-3 shows a numerical simulation (based on the FDTD method) of the imaging capabilities of a photonic crystal slab made of air holes embedded in a dielectric arranged in a square lattice geometry.

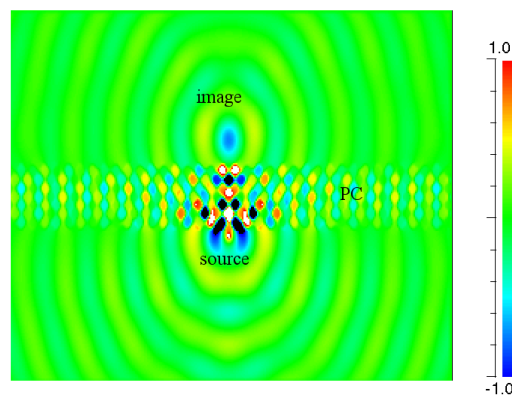


Figure 3-3: FDTD simulation of the real part of the magnetic field obtained performing the point imaging on a triangular photonic crystal slab made of air holes embedded in dielectric matrix at the normalized frequency $\omega = 0.192$ under TE polarization (\mathbf{H} field parallel to the holes axis). The radius of the hole is $r = 0.35a$ while the relative dielectric constant of the matrix is $\epsilon_r = 12$

Now, if we focus our attention to the second band of the photonic band structure in figure 3-1(b) we see that the concavity is negative, which is the condition where negative group velocity can be achieved. Moreover, if we choose a frequency where the EFC of the PC is circular, the electromagnetic properties of the crystal can be assimilated to that of a homogeneous medium [14,24]. In particular, we choose the frequency at which the frequency contour of the PC matches with that of the air, which for the case that we are considering is at $\omega = 0.305$, indicated in Fig.3-1(b) with ω_2 . From the analysis of the wave vector diagram in Fig.3-4 it can be seen that the only intersection of the construction line (green dashed line) with the EFC of the PCs (blue circle) originating an allowed propagating mode in the structure, is in point B. In fact because of the negative concavity of the band structure, and because of the causality requirement this is the only intersection that gives rise to a plane wave pointing away from the source (indicated with a bold blue arrow in Fig.3-4). The phase velocity (thin blue arrow) and group velocity (bold blue arrow) of the plane wave are antiparallel leading to the condition of negative refraction, $\mathbf{k} \cdot \partial\omega/\partial\mathbf{k} \leq 0$.

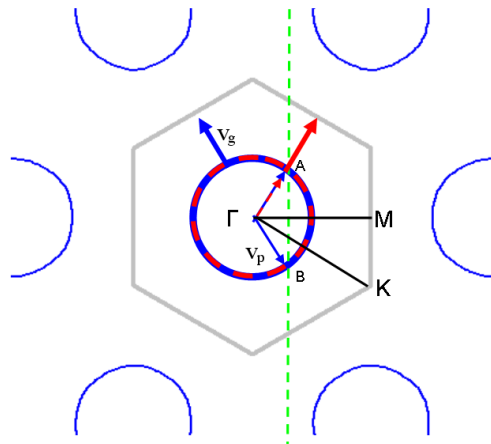


Figure 3-4: Negatively refracted beam constructed from the wave vector diagram method. The bold arrow indicate the group velocity direction, the thin arrow stand for the phase velocity direction, the red dashed circle is the air EFC whereas the blue circle indicates the crystal EFC. The gray polygon is the Brillouin zone while the black lines indicate the boundary of the irreducible Brillouin zone.

In figure 3-5 is shown the real part of the electric field (TE mode) for a point

imaging FDTD simulation performed on a nine row extended PC. There is a clear difference with this figure the case shown in Fig.3-3, which is in the way the field propagates inside the crystals. In the case of Fig. 3-3 the distribution is more intense in the direction perpendicular to the PC. In fact, there is a channel of propagation perpendicular to the slab surface (ΓM direction), which is evidence the anisotropic properties of the crystal EFC. On the other hand, the field distribution in the hexagonal crystal in figure 3-5 clearly shows that focusing first occurs inside of the slab and then a second focusing occurs outside the slab, that in turn, forms the image. This behavior corresponds to that of the Pendry superlens mentioned earlier, where the field propagation can be described in terms of a ray diagram approach by virtue of the isotropic properties of the photonic crystal EFC.

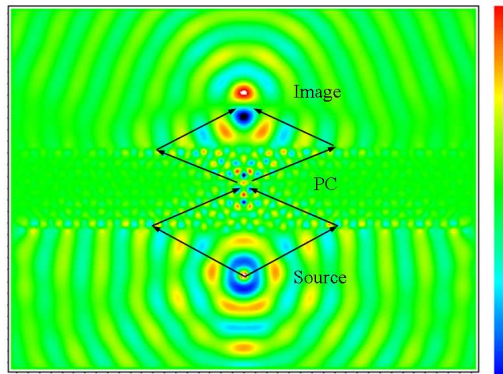


Figure 3-5: FDTD simulation of the real part of the electric field obtained performing the point imaging on a triangular photonic crystal slab made of air holes embedded in dielectric matrix at the normalized frequency $\omega = 0.305$ under TE polarization (\mathbf{E} field parallel to the holes axis). The radius of the hole is $r = 0.4a$ while the relative dielectric constant of the matrix is $\epsilon_r = 12.96$

3.3 Superlensing in 1D Photonic Crystals

The focusing properties of a flat lens made of tilted dielectric elements can be easily understood from the analysis of its Equi-Frequency Contours (EFCs), calculated using the transfer matrix method as in [44].

In the following we will assume TE polarization only, that is the electric field \mathbf{E}

perpendicular to the plane of incidence.

Consider a 1D photonic crystal of infinite extension (see inset in Fig. 3-6(b)) consisting of two different alternating dielectric materials having width W_1 and W_2 and permittivity ϵ_1 and ϵ_2 respectively. Assume that the layers are parallel to the y -axis with a period $a = W_1 + W_2$ along the x direction.

Figures 3-6(a)-(d) show the band structures and EFCs for the two different cases that we have experimentally studied in this work: the alumina-air (Figs. 3-6(a) and 3-6(c)) and the alumina-plexiglas case (Figs. 3-6(b) and 3-6(d)) respectively.

When the dielectric layers are all tilted by the same angle θ with respect to the normal to the lens (see Fig. 3-7(a)), the diffraction inside the structure can give rise to interesting focusing phenomena. The rotation of the layers in the spatial domain implies the same amount of rotation for the EFCs in the k -space. In Figs. 3-7(b) and (c) the wave vector diagrams at two different frequencies for a 1D PC, consisting of alumina-air alternating layers with $W_1 = W_2 = 0.5\text{cm}$, are shown. The magenta curves represent the equi-frequency contour for such structure, plotted in the first and repeated Brillouin zone (BZ), whereas the red circle is the air EFC. Curves are plotted at $\omega = 0.260$ (Fig. 3-7(b)) and $\omega = 0.457$ (Fig. 3-7(c)), where $\omega = a/\lambda$ is the normalized frequency. The two arrows inside the red circles in Figs. 3-7(b) and (c) are two generic wave vectors impinging the air-PC interface at different incoming angles γ_1 and γ_2 . The directions of the diffracted wave vectors inside the PC are determined by imposing the conservation of the tangential component $k_i^{\parallel} = \omega/c \sin \gamma_i$, here represented by the construction line drawn as a dashed line. The two wave vectors normal to the PC EFCs, k_{1r} and k_{2r} , are the diffracted waves that propagate inside the crystal. They are both directed perpendicularly to the EFC and point away from the source.

There is however a fundamental difference between the diffracted wavevectors depicted in Fig. 3-7(b): k_{1r} corresponds to an intersection between the construction line and the EFC lying in the 1st BZ whereas k_{2r} derives from the intersection in the

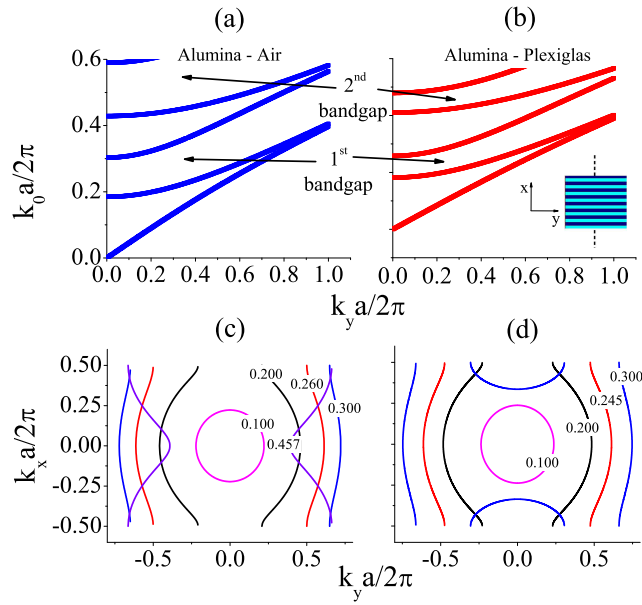


Figure 3-6: Band structure along the off-axis direction for a 1D PC with a unit cell realized using alumina and air (a) or alumina and plexiglas (b) respectively. (c) and (d): EFCs at different frequencies for the same structures.

repeated BZ and therefore is subjected to the folding back process. As it is easily seen in the plot of Fig. 3-7(b), k_{1r} and k_{2r} are positively and negatively refracted respectively. This phenomenon is a direct consequence of the equi-frequency contours shape shown by the 1D structure at the chosen normalized frequency.

At $\omega = 0.457$, although the shape of the EFC (see Fig. 3-7(c)) is very different from the one at $\omega = 0.260$, it is still possible to obtain the conditions for negative refraction due to the convex nature of the EFC with only 0th order diffracted waves involved.

These remarkable diffraction properties can be exploited to realize superlensing, since using a simple ray-diagram it is easy to show that an appropriately designed slab made of this kind of 1D PC will have an off-axis focusing. The performance of a flat superlens made of tilted dielectric elements has been already presented and discussed numerically by Wang et al. [45].

The focusing properties strongly depend on the orientation of the surface termination via the rotation angle θ . Off-axis subwavelength focusing is achieved in [45] for a

high index contrast ($Si - SiO_2$) layered structure, with the best FWHM of 0.164λ for $\theta = 44^\circ$. In this work we chose $\theta = 45^\circ$ since this gives us the best resolution for the index contrast structures presented here, consisting of layered elements of alumina-air and alumina-plexiglas.

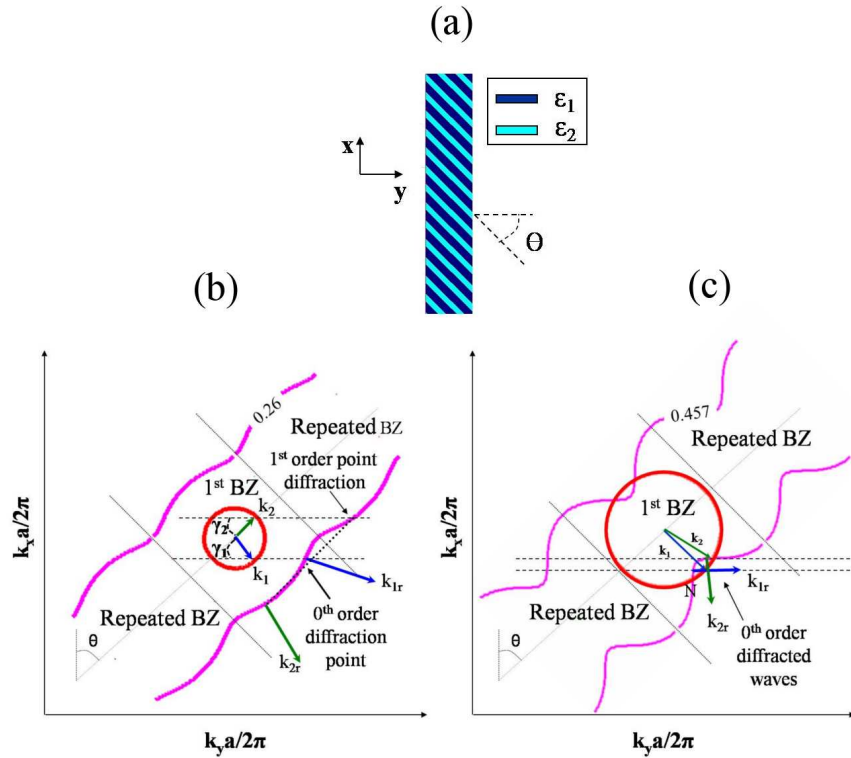


Figure 3-7: (a) Sketch of the slab obtained rotating, by an angle θ , a one dimensional PC having a unit cell made of two different dielectric materials $\epsilon_1 = 8.6$ and $\epsilon_2 = 1$. (b) and (c) equi-frequency contours at $\omega = 0.260$ (1^{st} band) and $\omega = 0.457$ (2^{nd} band) respectively, plotted in the first and in the repeated Brillouin zone, relatively to the crystal in (a); k_1 and k_2 are two wave vectors impinging the air-PC interface at two generic different angles γ_1 and γ_2 , whereas k_{1r} and k_{2r} are the wave vectors diffracted inside the crystal.

3.3.1 Study of the Focusing Properties and Effect of Surface Corrugation

We also show, by means of Finite-Difference Time-Domain (FDTD) simulations that the surface corrugation coming from the simple rigid rotation of the dielectric layers can dramatically improve the performance of this flat lens.

The discretization grid for the simulation domain is $a/30$ along the x and y direction. A point source is located on the slab axis and centered 1cm far from the PC interface without corrugation. The source holds the same position also for the case with corrugation.

In Fig. 3-8(a) a detail of the lens we simulated ($\epsilon_1 = 8.6$, $\epsilon_2 = 2.5$), with and without corrugation on both surfaces, is shown. For the case under study, this particular kind of corrugation yields two evident benefits. First, it increases the transmission efficiency (Fig. 3-8(b)) by about 50%, because of the reduced impedance mismatch with the surrounding medium. Then, it produces also a significant improvement in both the transversal and lateral resolution (about 11% and 36% respectively), as shown in Figs. 3-8(c) and (d).

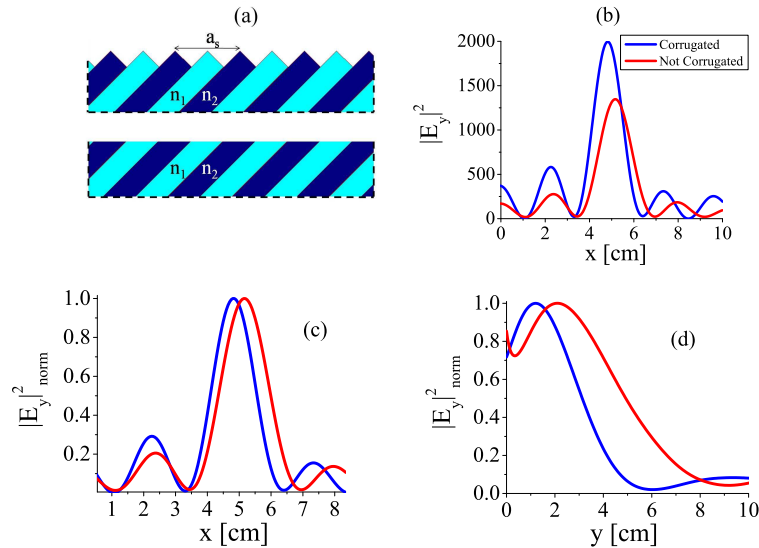


Figure 3-8: (a) Detail of the photonic crystal surface termination for the case with and without corrugation. (b) Comparison of the focus profiles (calculated via FDTD) produced by the slab with corrugation (blue line) and without corrugation (red line). (c) and (d) Transversal and lateral profiles respectively of the transmitted energy in a normalized scale. All the above profiles are taken along the lines (parallel and perpendicular to the PC surface) where the focused image exhibits its maximum.

These enhancements are usually related to the presence of surface states introduced by the surface corrugation [46]. The benefits to the imaging quality introduced by the surface states are a well known property of photonic crystals [47, 48]. It

has been proved both numerically [49] and experimentally [50, 51] that choosing the appropriate corrugation can increase the imaging resolution performance of a PC superlens. Furthermore, surface states can be exploited as well to realize beam shaping with using waveguide made of 2D photonic crystal with corrugated surface [52].

We also numerically evaluated how the frequency at which the lenses show the maximum peak intensity for the focused image varies with the finite width ratio $\alpha = W_1/(W_1 + W_2)$. A parametric study for different values of the dielectric constants ϵ_1 and ϵ_2 was carried out. Results show (see Fig. 3-9(a)) that within a relatively wide range centered at $\alpha = 0.55$ the frequency linearly decreases with increasing α . Moreover, the curves that fit different sets of data, including the cases of alumina-air and alumina-plexiglas based PCs, are approximately parallel.

The lens performance severely degrades, with no focusing observed at all outside the range [0.47, 0.63]. For a fixed value of α , the focusing frequency linearly decreases also by increasing the permittivity of one of the two materials (Fig. 3-9(b)). The square-dotted line represents the case where the elements with the highest permittivity are kept constant ($\epsilon_1=12.5$), letting ϵ_2 to vary from 1 to 5.5, whereas the circle-dotted line represents the case with $\epsilon_2 = 1$, and ϵ_1 is let to vary from 5 to 12.5. We think that it is possible to use these findings as simple “rule of thumb” to design a flat 1D PC superlens consisting of tilted dielectric elements.

3.3.2 Experimental Results

Experimental results are carried out by sandwiching the PCs in an aluminum parallel-plates waveguide terminated with microwave absorbers and measuring the amplitude and phase of the electric field transmitted by the crystals in the image plane. Since the loss tangent of both alumina and plexiglas are extremely small at the frequency of interest for this work ($\tan \delta_{Al} < 10^{-3}$, $\tan \delta_{Pl} < 10^{-2}$), dielectric losses can be neglected.

A dipole antenna (radius = 0.6mm) is used as a source, oriented to produce an

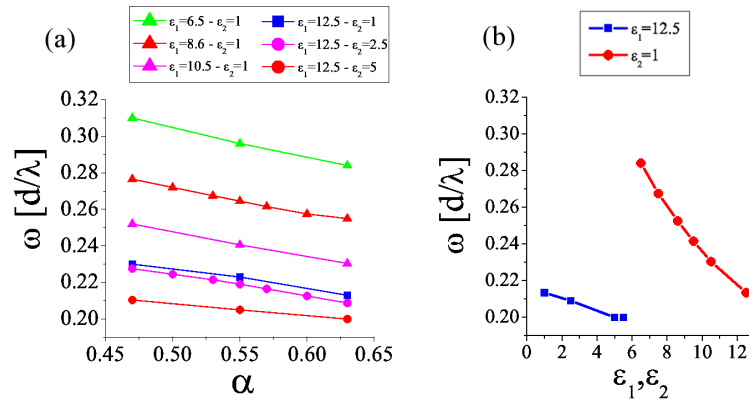


Figure 3-9: Plot of the normalized frequencies at which slabs made of different materials show the maximum transmission for the focused image as a function of the finite width ratio α (a) and dielectric constants ϵ_1, ϵ_2 (b) of the tilted elements ($\theta = 45^\circ$).

electric field z -oriented (TE mode) and operating in the range of frequencies that spans from $5GHz$ to $15GHz$, in order to reproduce the same normalized frequency a/λ of the theoretical model. Due to the waveguide characteristics, the TEM mode only can propagate up to $15GHz$. The maps of the amplitude and phase of the electric field are collected by using a HP8720C Vector Network Analyzer. Another dipole antenna with the same characteristics of the source is used as a detector that moves along the waveguide plane using an x-y step motor. Details of this technique has already been presented in [39].

We have conducted point imaging experiments on two different structures using, in the first case a unit cell made of alumina and plexiglas, in the second case alumina and air. It is straightforward that the latter structure comes as the natural consequence of the first one, since it is obtained by the simple removal of all plexiglas layers. For this reason the two PCs have the same lattice properties but a different index contrast. The PC slabs before rotation, are built with a lattice constant $a = 1cm$, length $L = 30cm$ and width $w = 5.65cm$. We chose dielectric elements having the same width, therefore the corresponding layer widths in the unit cell are $0.5a$ for both structures under study.

When all layers are rotated by the same angle θ , the PC can be seen as a 2D

structure having lattice constants along x and y directions given by $a_x = a/\sin\theta$ and $a_y = a/\cos\theta$ respectively, length $L_s = 30a/\cos\theta$ and width $w_s = w\sin\theta + 0.5a\cos\theta$, where the width is defined including the corrugation.

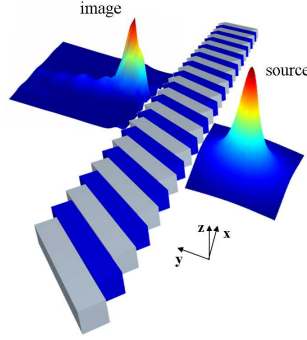


Figure 3-10: (Color online) 3D spatial mapping of the point source signal transmitted by the alumina-air slab at 13.7175GHz .

For the sake of clarity, in Fig. 3-10 is shown the 3D map of the measured point source imaged by the slab.

Measurements are performed scanning an area 10cm wide and 10cm long adjacent to the PC-air interface, in steps of 2mm in both x and y direction. The point source is positioned 1cm far from the lens in $x = 0\text{cm}$, according to our reference system.

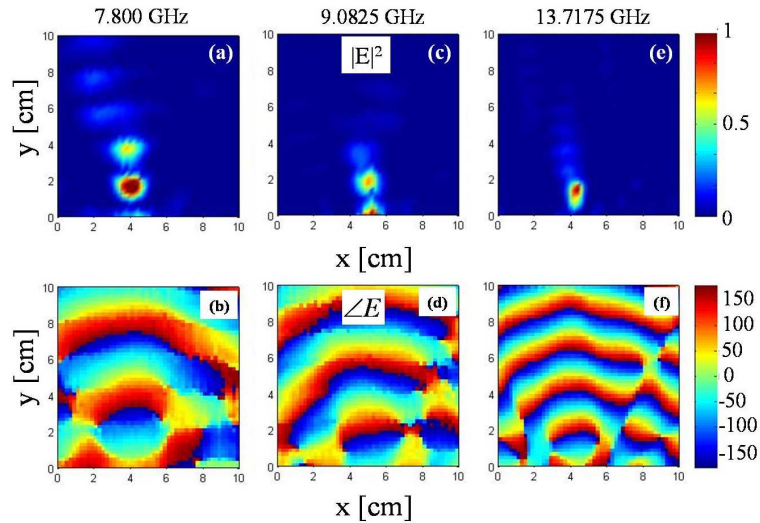


Figure 3-11: In-plane spatial mapping of the measured electric field intensity ((a), (c), (e)) and phase ((b), (d), (f)) for the alumina-air PC at 7.800GHz , 9.0825GHz and 13.7175GHz respectively.

In Figs. 3-11(a)-(f) the complete experimental results for the alumina-air lens are illustrated. This structure exhibits subwavelength imaging in three different bands, $BW_1 = [7.6200 - 7.8200]GHz$, $BW_2 = [8.4700 - 9.2200]GHz$, $BW_3 = [13.4500 - 14.2300]GHz$. The signals imaging are clearly off-axis as evident from the electric field intensity maps in Figs. 3-11(a), (c), (e), and as also predicted by [45].

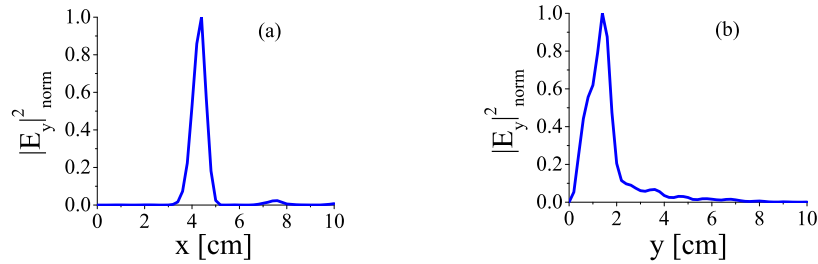


Figure 3-12: Normalized transversal (a) and lateral (b) experimental profiles, taken at $13.7175GHz$ along the lines where the focused image exhibits its maximum, for the alumina-air superlens.

In these three bands, the best achieved resolutions (FWHM) are 0.29λ at $7.8000GHz$ ($\omega = 0.260$), 0.32λ at $9.0825GHz$ ($\omega = 0.300$) and 0.29λ at $13.7175GHz$ ($\omega = 0.457$). Since in Figs. 3-11(a), (c), (e) we use a normalized scale, it is worthwhile to mention that the maximum transmitted intensity decreases with increasing frequency. This is because for higher frequencies the amount of wavevectors collected and focused is lower due to the different shape of the EFCs. It is also worth noting that the measured values of the FWHM well agree with numerical simulations within 30%. In all three cases the focused images are clearly visible, as shown by the spatial mapping of the electric field intensity detected in the image plane and reported in Figs. 3-11(a), (c), and (e). The absence of noticeable aberration is confirmed by the respective phase maps in Figs. 3-11(b), (d), (f), that exhibit a pattern typical of circular waves. In Figs. 3-12(a) and (b) the transversal and lateral profiles respectively for the alumina-air case are shown, as measured at $f = 13.7175GHz$. In Figs. 3-13(a) and (b) the transversal and lateral profiles respectively for the alumina-plexiglass case are shown, measured at $f = 7.3505GHz$ ($\omega = 0.245$). At this frequency, we obtain the best lens resolution (FWHM) of 0.27λ .

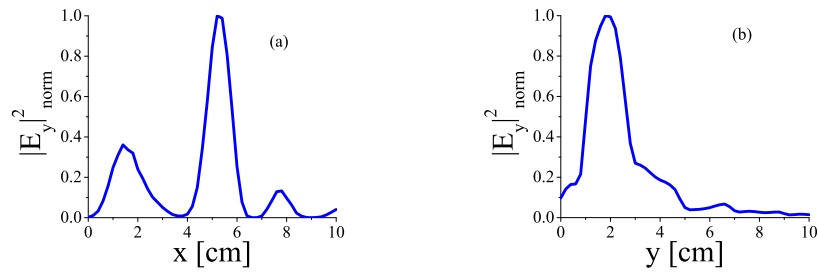


Figure 3-13: Normalized transversal (a) and lateral (b) experimental profiles, taken at 7.3505GHz along the lines where the focused image exhibits its maximum, for the alumina-plexiglas superlens.

We also measured the spatial shift of the focused image changing the source position along the y direction (normal to the PC surface). In Figures 3-14(a) and (b) the simulated and measured lateral profiles respectively of the electric field intensity (in the normalized scale) for the alumina-plexiglass slab are reported. Experimental data (Fig. 3-14(b)) clearly show that the image focus moves closer to the PC superlens as long as the point source moves away, strictly following the behavior predicted by the numerical analysis (Fig. 3-14(a)), and in accordance also with what expected from a simple ray-diagram.

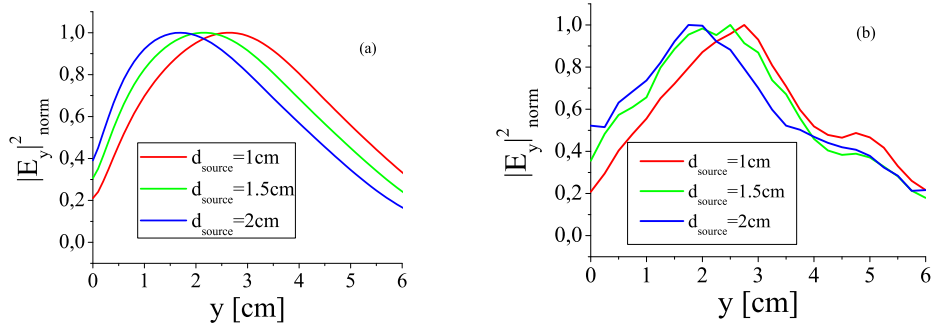


Figure 3-14: Simulated (a) and measured (b) lateral profiles respectively for the focused image of a point source changing its position (d_{source}) normal to the surface of the alumina-plexiglass PC superlens

Part II

Non-Diffractive Metamaterials

CHAPTER 4

Thin-Wires and Split Ring Resonators

4.1 Introduction

In chapter one we introduced a class of non-diffractive metamaterials that showed their unusual properties only when their “atom” sizes were much smaller than the wavelength. For this reason these metamaterials can be modeled by means of an effective medium theory where the whole structure can be described by an effective permittivity ϵ_{eff} for the case of cut wires, and an effective permeability μ_{eff} in the case of a split ring resonators (SRRs) array. These two geometries currently represent the most suitable way to build structures with negative effective properties from the microwave [1] to the optical range [53]. It is also worth mentioning that today considerable efforts are being made to manufacturing metamaterials for terahertz applications which are very promising for medical applications and homeland security imaging. In fact, unlike the X-Ray, THz radiation is not invasive and can more easily be used for the detection of a variety of chemical substances, drugs, explosives, and weapons, and in addition also for tomography.

4.2 Thin-Wire Medium

Periodically arranging thin cut wires can lead to an artificial material which can be modeled in terms of the Drude model [11, 54, 55], where the effective permittivity can be written as,

$$\epsilon_{eff} = 1 - \frac{\omega_p^2}{\omega(\omega + i\gamma)} \quad (4.1)$$

It is important to note that ω_p depends on the geometry of the lattice rather than by the charge, the effective mass, and the density of electrons, as in the case of naturally occurring media. Furthermore from the above equations, when $\omega < \omega_p$ the effective permittivity is negative. Another interesting point of this structure, beside its effective medium properties, is that the plasma frequency is shifted down by six order of magnitude. Moreover, as will soon be discussed, the ω_p can be further shifted by making the wires thinner.

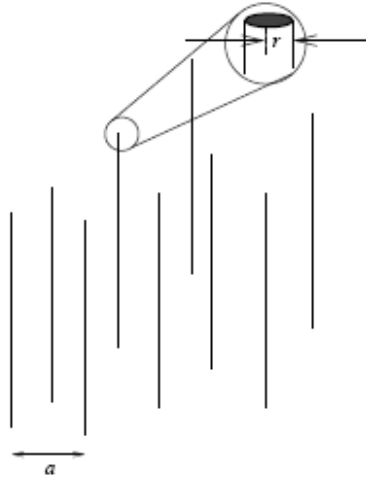


Figure 4-1: Periodic structure composed of infinite wires having radius r arranged in a cubic lattice of period a

Periodic structures built from very thin wires dilute the average concentration of electrons and considerably enhance the effective electron mass through self-inductance.

The conduction electrons of a metal interact with the electromagnetic field to form what is called a surface plasmon, a collective oscillation of electron density. Trying to restrict electrons to move along thin wires has two consequences: the first one is that the average electron density n_{eff} is reduced because only part of the space is filled by the metal, leading to,

$$n_{eff} = n \frac{\pi r^2}{a^2} \quad (4.2)$$

where n is the density of electrons in the wires, r is the radius of the wire and a is the cell side of the square lattice on which the wires are arranged. The second consequence is an enhancement of the effective mass of the electrons caused by magnetic effects. Suppose a current flows in the wire creating a magnetic field circling the wire, then,

$$H(R) = \frac{I}{2\pi R} = \frac{\pi r^2 n v e}{2\pi R} \quad (4.3)$$

where R is the distance from the wire center and v is the mean electron velocity. We can thus write the magnetic field in term of a vector potential:

$$\mathbf{H}(R) = \mu_0^{-1} \nabla \times \mathbf{A} \quad (4.4)$$

where

$$\mathbf{A}(R) = \frac{\mu_0 \pi r^2 n v e}{2\pi} \ln(a/R) \quad (4.5)$$

where a is the lattice constant.

From Classical Mechanics, electrons in a magnetic field have an additional contribution to their momentum of $e\mathbf{A}$, and thus the momentum per unit length of the wire is given by:

$$e\pi r^2 n A(r) = \frac{\mu_0 e^2 (\pi r^2 n)^2 v}{2\pi} \ln(a/r) = m_{eff} \pi r^2 n v \quad (4.6)$$

and thus the new effective mass of the electrons becomes:

$$m_{eff} = \frac{\mu_0 e^2 \pi r^2 n}{2\pi} \ln(a/r) \quad (4.7)$$

Then from the classical formula for the plasma frequency we can write

$$\omega_p^2 = \frac{n_{eff} e^2}{\epsilon_0 m_{eff}} = \frac{2\pi c^2}{a^2 \ln(a/r)}. \quad (4.8)$$

4.3 Split Ring Resonators

Following John Pendry's theory that a periodic arrangement of thin wires could mimic the response of a dilute plasma, the next step was to find a magnetic analogue of an electric conductor. Pendry again offered a solution to this problem by proposing that a periodic arrangement of rings provided with a gap could behave like a magnetic material and support magnetic resonance. He suggested that if we are able to induce an electric current to circulate in a closed loop this will generate a magnetic dipole having a moment \mathbf{m} (see Fig.4-2(a))

$$\mathbf{m} = \frac{1}{2} \int \mathbf{r} \times \mathbf{j} dV. \quad (4.9)$$

In addition if we are also able to introduce resonance, negative permeability can be achieved. By borrowing the idea from the formalism of circuit theory we can model the closed ring as an inductor having inductance L and then introduce a resonance by adding a capacitor C . This can be accomplished by introducing a small gap of width g along the ring, as shown in Fig.4-2(b).

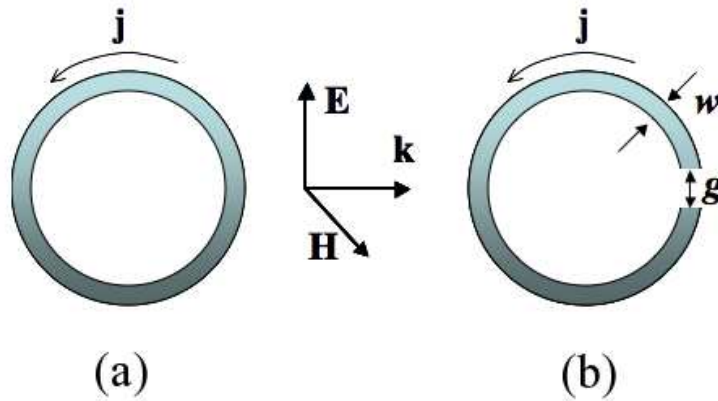


Figure 4-2: Schematic of a closed ring (a) and split ring resonator (b).

Under this condition, a time varying magnetic field parallel to the ring axis can induce a current density in to the LC circuit-like element. Thanks to the gap the split ring can now prevent the current to circulate around the ring, sustaining a resonance condition that, for frequencies within the resonance band, gives rise to the negative permeability behavior.

Fig. 4-3 illustrates an SRR made with two concentric split rings. The purpose of the second ring, whose split is oriented opposite to the first, is to generate a large capacitance in the small gap region between the rings, lowering the resonant frequency and concentrating the electric field.

By arranging the split ring resonators in the shape of a periodic medium where

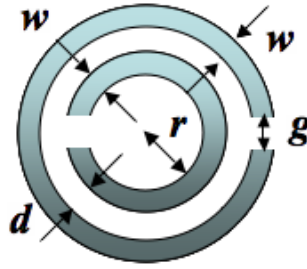


Figure 4-3: Schematic of a split ring resonator made of two concentric rings.

there is a strong magnetic coupling between the resonators, unique properties emerge from the composite. Each SRR responds to an incident magnetic field behaving like a single “atom” with its own magnetic dipole moment. The structure as a whole, behaves like an effective medium having an effective permittivity μ_{eff} given by [8]:

$$\mu_{eff} = 1 - \frac{\frac{\pi r^2}{a^2}}{1 + \frac{2l\rho}{\omega r \mu_0} i - \frac{3l}{\pi^2 \omega^2 \mu_0 C r^3}} \quad (4.10)$$

where ρ is the resistance per unit length of the rings measured around the circumference, ω is the frequency of the incident radiation, l is the distance between layers, a is the lattice parameter, w is the ring width and r and d are defined in Fig.4-3. C is the capacitance between the two elements of the split ring. If we assume the following constraints,

$$r \gg w, \quad r \gg d, \quad l < r \quad \text{and} \quad \ln \frac{w}{d} \gg \pi \quad (4.11)$$

the capacitance between the unit length of two parallel sections of metallic strips reads

$$C = \frac{\epsilon_0}{\pi} \ln 2wd = \frac{1}{\pi\mu_0c_0^2} \ln \frac{2w}{d}. \quad (4.12)$$

Substituting the (4.12) in (4.10) leads to the following expression for the effective permeability,

$$\mu_{eff} = 1 - \frac{\frac{\pi r^2}{a^2}}{1 + \frac{2l\rho}{\omega r\mu_0}i - \frac{3lc_0^2}{\pi\omega^2 \ln(\frac{2w}{d})r^3}}, \quad (4.13)$$

which can be also written in the following form,

$$\mu_{eff} = 1 - \frac{F\omega^2}{\omega^2 + i\omega\Gamma - \omega_0^2}, \quad (4.14)$$

where Γ is the dissipation factor, and while F is the fractional area of the unit cell occupied by the interior of the split ring. It is also interesting to note that the expression (4.2) carries that same dependence from F . As example, figure 4-4 plots both the real and the imaginary part of the $\mu_{eff}(\omega)$. There are two the important parameters to highlight: the resonance frequency ω_0

$$\omega_0 = \sqrt{\frac{3lc_0^2}{\pi \ln \frac{2w}{d} r^3}} \quad (4.15)$$

and the magnetic plasma frequency ω_{mp} which in the lossless case is related to the resonant frequency by the following relation,

$$\omega_{mp} = \frac{\omega_0}{\sqrt{1-F}}. \quad (4.16)$$

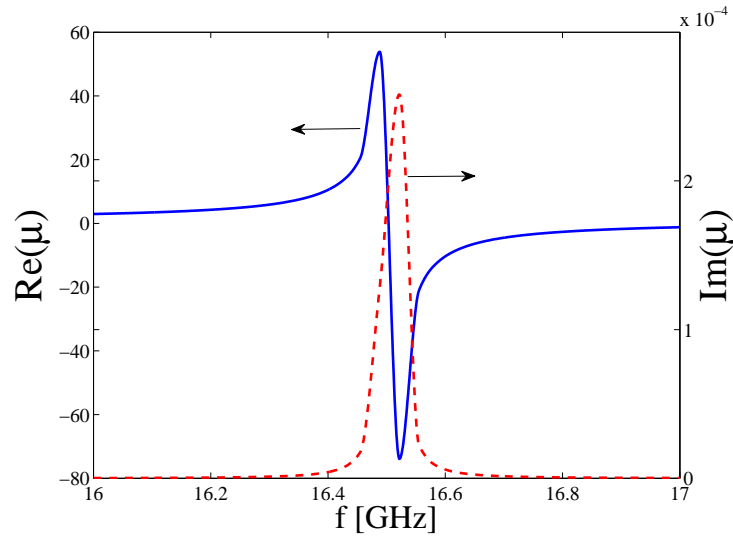


Figure 4-4: Real part (continuous line) and imaginary part (dashed line) of the $\mu_{eff}(\omega)$

The important point to note is that for $\omega_0 < \omega < \omega_{mp}$ the effective permeability is negative and the band $(\omega_{mp} - \omega_0)$ is inversely proportional to the square root of the factor $(1 - F)$ which is the fraction of the unit cell not occupied by the interior of the split ring. This means that increasing the radius r of the internal SRR shifts the frequency ω_{mp} to higher values.

4.3.1 Circuit Modeling of SRRs

Previously we mentioned that the electromagnetic response of a split ring resonator can be described by means of the electric circuit theory formalism. In Fig. 4-5 the equivalent circuit models for the case of a single split ring resonator and a double split ring resonator are shown.

By applying the Kirchoff's law to the circuit mesh in Fig.4-5(a) we have

$$L \frac{d^2 q}{dt^2} + R \frac{dq}{dt} + \frac{q}{C} = -\frac{dB}{dt} \pi r_0^2 \quad (4.17)$$

where the right-hand side term of the previous equation is the contribution of the

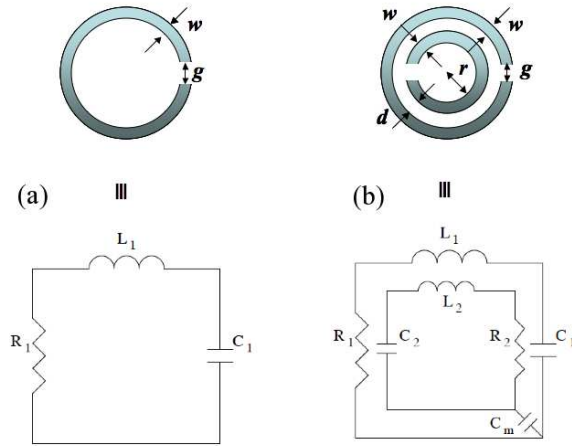


Figure 4-5: Equivalent circuitual model for the single split ring (a) and the double split ring (b).

induction law. By switching to the frequency domain the Eq.(4.16) becomes

$$-\omega^2 Lq + i\omega qR + \frac{q}{c} = -i\omega B\pi r_0^2 \quad (4.18)$$

where we have simply made the substitution $\frac{d}{dt} \rightarrow i\omega$.

From the (4.17) the current induced in the SRR is

$$I = i\omega q = \frac{\frac{B\pi r_0^2}{L}\omega^2}{\omega^2 - i\frac{R}{L}\omega - \frac{1}{LC}}. \quad (4.19)$$

The magnetization M can be expressed in term of the circuit parameters as

$$M = NI\pi r_0^2 = -\frac{\frac{NB(\pi r_0^2)^2\omega^2}{L}}{\omega^2 - i\frac{R}{L}\omega - \frac{1}{LC}}, \quad (4.20)$$

as M can also be written as

$$M = \frac{1}{\mu_0} \frac{\mu - 1}{\mu} B \quad (4.21)$$

by comparing the (4.20) and (4.19) we have the following form for the μ

$$\begin{aligned} \mu &= \frac{\omega^2 - i\frac{R}{L}\omega - \frac{1}{LC}}{\omega^2 \left(1 + \frac{N\mu_0(\pi r_0^2)^2}{L} - i\frac{R}{L}\omega - \frac{1}{LC} \right)} \\ &= 1 - \frac{\frac{\Gamma}{1+\Gamma}\omega^2}{\omega^2 - i\omega\frac{R/L}{1+\Gamma} - \frac{1}{LC(1+\Gamma)}} \end{aligned} \quad (4.22)$$

where

$$\Gamma = 1 + \frac{N\mu_0(\pi r_0^2)^2}{L}. \quad (4.23)$$

Equation (4.22) has the same resonant form as equation (4.14), to proof that the circuital approach is in agreement with the approach followed by Pendry in [8].

4.4 Effective Parameters Retrieval Technique

The design of a metamaterial structure made from either cut wires, or SRRs, or both, involves two main steps. The first step is to start from the analytical model, such as the Pendry's model described in Eqs. (4.13 - 4.16) where SRRs are utilized. The second step is to use numerical tools to confirm that the actual design works. For this purpose, we have used HFSS software from *Ansoft*, based on the Finite-Integration-Technique (FIT), to compute the electromagnetic problem. For this study, we will focus solely on the design of structures made of SRRs, bearing in mind that the guide lines for periodic media made with cut wires, SRRs or both are the same. The first

question that needs to be answered when designing a metamaterial structure is, how to compute the effective permeability and the effective permittivity. The Snell law does not offer assistance here because it can only provide the real part of the effective index at a single frequency, while, in our case we want a rapid and reliable method for obtaining the parameters $\epsilon(\omega)$ and $\mu(\omega)$, which are complex function of frequency. The approach that we have used to calculate numerically the effective parameters of an array of split ring resonators, has been deeply investigated in literature by *Smith, Soukoulis et al.* ([56–58]), and is based on the assumption that electromagnetic metamaterials should respond to electromagnetic radiation as continuous materials at least in the long wavelength limit [8,11]. Moreover, the hypothesis that certain metamaterials configuration can exhibit scattering properties consistent with the approximate form of ϵ and μ has also been proved experimentally by *Smith et al.* [55,59]. This approach utilizes the transmission and reflection coefficients (S-parameters) calculated for a wave that is normally incident on a finite slab of metamaterial. Assuming that the slab is characterized by an index n and an impedance z , simple analytic expressions can be found by inverting the S-parameters, that relate n and z to S. Finally, we retrieve μ_{eff} and ϵ_{eff} from the relations $\epsilon = n/z$ and $\mu = nz$ upon the satisfaction of certain physical requirements based on causality.

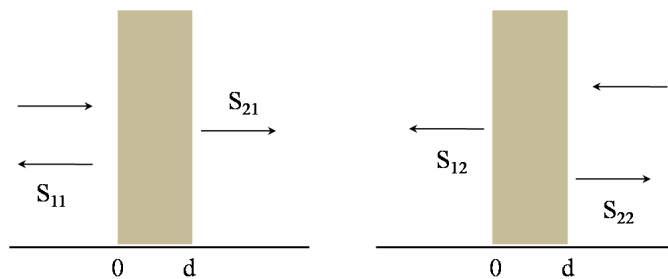


Figure 4-6: Wave incident on a slab of thickness d . The meaning of the S-parameters (i.e. the complex transmission and reflection coefficients) is illustrated.

The transmission and reflection coefficients for waves normally incident on the face of a one-dimensional slab of continuous material having length d , and traveling rightward along the x direction, as shown in Fig.4-6, are related to n and z by

$$\frac{1}{T} = \left[\cos(nkd) - \frac{i}{2} \left(z + \frac{1}{z} \right) \sin(nkd) \right] e^{ikd} \quad (4.24)$$

$$\frac{R}{T} = \left[-\frac{1}{2} i \left(z - \frac{1}{z} \right) \sin(nkd) \right] e^{ikd}. \quad (4.25)$$

where $k = \omega/c$ is the wave number of the incident wave. From the inversion of the equations (4.24) and (4.25) we have the following expressions for the material parameters

$$z = \pm \sqrt{\frac{(1 + S_{11})^2 - S_{21}^2}{(1 - S_{11})^2 - S_{21}^2}} \quad (4.26)$$

$$Im(n) = \pm Im \left(\frac{\cos^{-1} \left(\frac{1}{2S_{21}} [1 - (S_{11}^2 - S_{21}^2)] \right)}{kd} \right) \quad (4.27)$$

$$Re(n) = \pm Re \left(\frac{\cos^{-1} \left(\frac{1}{2S_{21}} [1 - (S_{11}^2 - S_{21}^2)] \right)}{kd} \right) + \frac{2\pi m}{kd} \quad (4.28)$$

where m is an integer number, and where the scattering parameters can be expressed as $S_{11} = R$ and $S_{21} = Te^{jkd}$. The ambiguities related to the signs of equations (4.26-4.28) are fixed by imposing the following physical constraints: the material must be passive, which leads to the following choice for the sign of $Re(z) > 0$, whereas, enforcing $Im(n) > 0$ results in an unambiguous sign for $Im(n)$, and also, uniquely identifies the sign of $Re(n)$. It is important to make clear that the Eqs.(4.26-4.28) are valid for the case of a slab made of homogeneous material. When the unit cell is inhomogeneous, the validity of these equations becomes questionable since the symmetry along the propagation direction is broken, and S_{11} and S_{22} can no longer be considered equal. This implies that the dispersion relation for the refractive index has to be defined either by

$$\cos(nkd) = \frac{1}{S_{21}}(1 - S_{11}^2 + S_{21}^2) \quad (4.29)$$

or by,

$$\cos(nkd) = \frac{1}{S_{21}}(1 - S_{22}^2 + S_{21}^2) \quad (4.30)$$

which, since $S_{11} \neq S_{22}$, gives different values depending on the propagation direction.

However, it was shown [58] that if the unit cell is repeated infinitely a unique value of the index can be recovered, while the dispersion relation for n becomes

$$\cos(nkd) = \frac{1 - S_{22}S_{11} + S_{21}^2}{2S_{21}}. \quad (4.31)$$

CHAPTER 5

Theory of Slow-Light in Metamaterials Structures

5.1 Introduction

Since the speed of photonic systems is much larger than that of electronic systems, the synergy between optics and photonics represents the most promising way to achieve faster communications and data processing rates. Contrary to many research fields in the area of photonics, which are focused on developing communication systems designed to handle continually increasing speeds, there is a branch of the photonic community in which scientists are working to slow down the speed at which light propagates, and in principle to even stop it. The velocity of light in vacuum c_0 , is approximately $3 \times 10^8 s^{-1}$, fast enough to travel around the world for 7.5 times in just one second. The speed of light is that high that some times is it very difficult to control light propagation in the time domain. For this reason, the control of light is a fundamental step toward the goal of *all-optical on chip*. As illustrated in figure 5-1, where is shown a schematic model of a photonic circuit, the ability of processing information traveling under the form of light is related to the possibility of realizing devices that can modulate the velocity of the information and also store data, exactly like the building blocks of a basic electronic digital circuit.

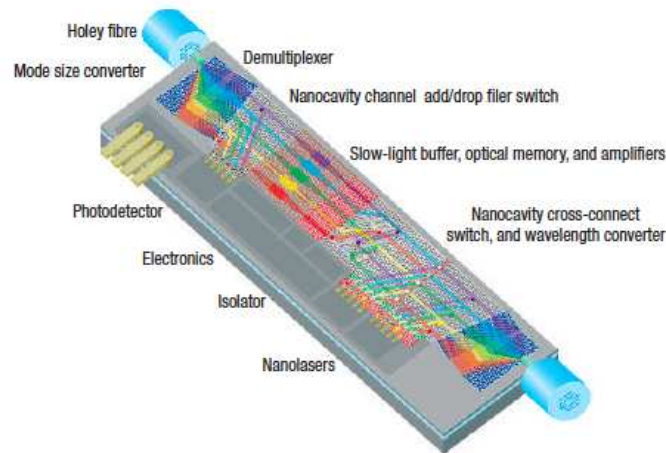


Figure 5-1: Example of a PC based chip provided with all the functions typical of a conventional electronic chip.

5.2 State of the Art

The definition of velocity that is most meaningful in *Slowlight* applications is the group velocity v_g , which describes the speed at which a pulse envelope propagates. In general, v_g is greatly reduced by a large first-order dispersion arising from an optical resonance within the material or structure.

In the past years slowlight has been proven in different ways.

One of the first attempts was via a quantum mechanical interference effect called *electromagnetic induced transparency* (EIT) [60, 61]. Using quantum interference effects involving coherence between the two atomic ground-levels of a three level *Lambda*-system, an initially absorbing medium can be rendered transparent to a resonant weak probe laser when a strong coupling laser is applied to the other optical transition. This effect has gained enormous importance recently because of a variety of possibilities in nonlinear optics and quantum information science, as it leads to the fascinating phenomena of slow light, stopped light, or enhancement of nonlinear effects. However, although it was shown that EIT can allow very long delay it is not suitable for integration purposes because of the large facilities that are needed.

Currently, the most promising candidates to achieve slow-light are engineered structures such as left-handed materials. Because of the dispersion properties shown by their photonic band structure, photonic crystals show region of frequency where in principle it is possible to stop light. Unfortunately, the ineluctable fluctuations of the crystal parameters arising from the manufacturing process reflect in the variability of the photonic band structure properties, making the light trapping almost impossible. However, as shown at microwave frequencies by *Di Gennaro et al.* [2] a light pulse propagating in a bulk photonic crystal can be slowed down by a factor of ten with a resulting group velocity $v_g = c_0/10$ (see Fig.5-2(a)). They also showed that better results can be obtained in left-handed material slabs made of SRRs and cut-wires (composed metamaterial (CMM)), where $v_g = c_0/50$ (see Fig.5-2(b)) was measured.

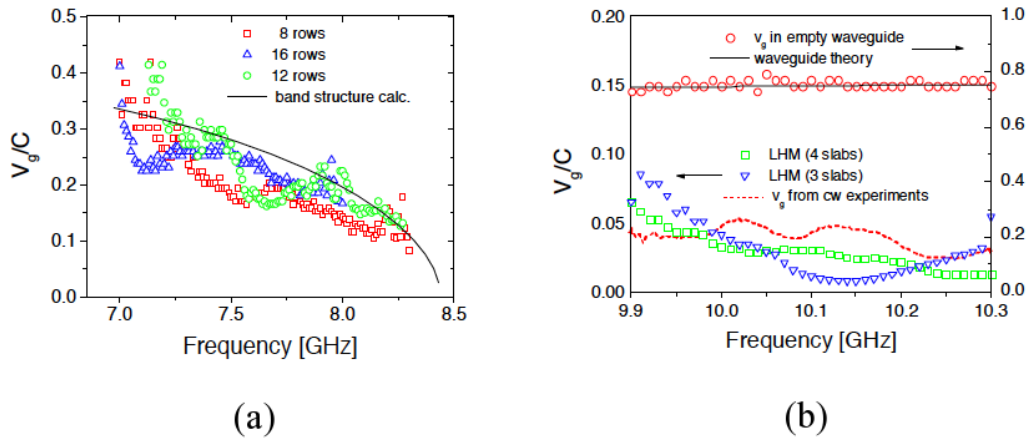


Figure 5-2: (a) Group velocity along ΓM direction versus frequency for three different lengths of PC sample. Solid black line represent the predicted behavior from band structure calculation. (b) Left y axis - group velocity dispersion of a CMM in a waveguide for different sample lengths compared with cw experiment result (red dot line). Slowest v_g of $c/50$ is obtained at 10.3 GHz in this configuration. Right y axis - Experimental and theoretical empty waveguide group velocity dispersion [2].

A different idea was proposed by *Baba et al.* They investigated the slow-light properties of photonic crystal waveguides (see Fig.5-3) at optical frequencies [3] and reported a group velocity delay of about $v_g = c_0/70$. This result is important because it is obtained on a small volume structure suitable for integration and easy to manufacture with the present technologies.

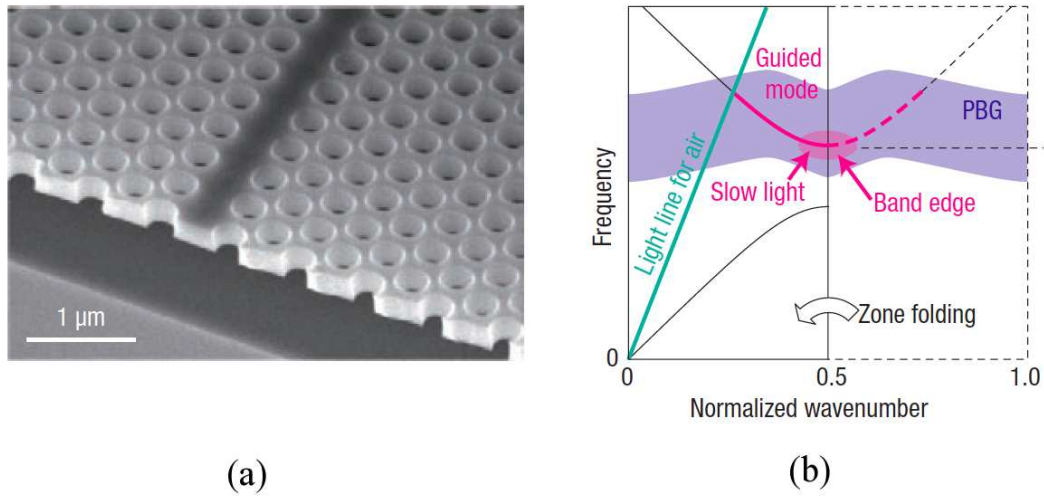


Figure 5-3: (a) Scanning electron microscope image and, (b), schematic band and group-index spectrum of a silicon PCW with respect to the absolute frequency [3].

Outstanding performance has been obtained by *Tanabe et al.* [4], using high-Q cavity made with PCs, where they show a slowdown factor that brings the group velocity of a pulse envelope down to $v_g = 2 \times 10^{-5}c_0$. This result is excellent because it caters to the small volume of the device, making PCs the best candidates for slowlight applications and eventually for light trapping.

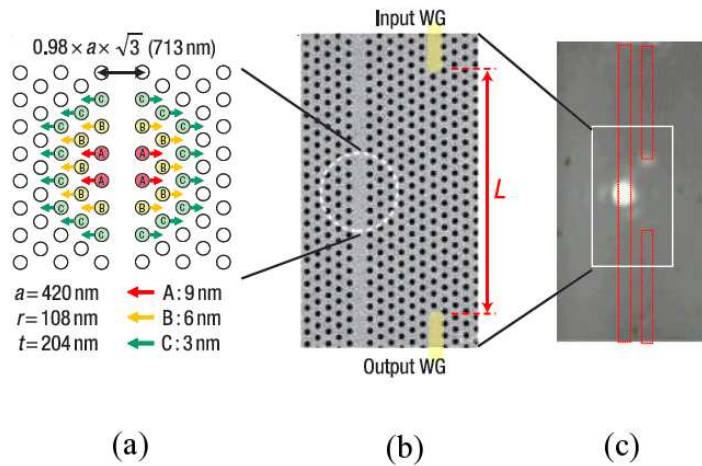


Figure 5-4: Photonic-crystal nanocavity with a locally modulated waveguide width. (a) The design parameters, where a is the lattice constant, r is the hole radius and t is the slab thickness. (b) A SEM image of the device fabricated in a silicon photonic-crystal slab. (c) A near-field image acquired using a near-infrared camera from the top of the sample when a resonant wavelength light was injected through the input waveguide. The waveguide regions are indicated by the red squares [4]

A different approach was followed by *Tsakmakidis et al* [5] who first proposed theoretically a wave guide having a core with $\epsilon < 0$ and $\mu < 0$ and a positive index cladding made of dielectric, as shown in Fig.5-5(a). This waveguide supports degenerate modes at which, for an opportune core thickness d , the propagating rays inside the core experience negative Goos-Hächen phase shift that traps them inside the core.

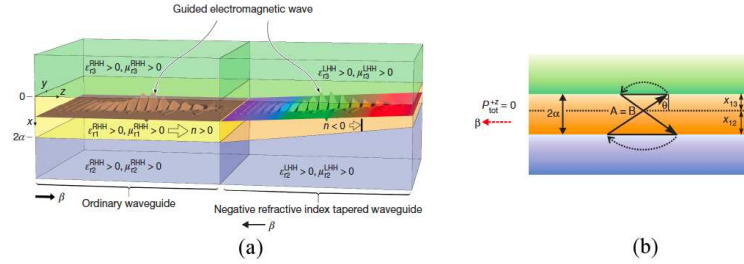


Figure 5-5: (a) Schematic of the waveguide structure made up of an ordinary waveguide part and a tapered waveguide part having a metamaterial core. A wave packet is efficiently injected in from the ordinary waveguide to the left-handed part experiencing a spatial decomposition in to its frequency constituents. (b) Ray diagram of the light inside the tapered metamaterial core when experiencing the Goos-Hächen phase shift [5]

5.3 Slow-Light Theory

Before we carry on with the description of the slowlight phenomena in metamaterials structures, it is important to first highlight the useful physical parameters used in characterizing the propagation of a pulse envelope in a generic dielectric waveguide. Together with the group velocity $v_g = d\omega/dk$, another important parameter is the *Group Delay* τ_g , which represents the time it takes for a pulse to travel a unit distance, for example, the group delay in vacuum is 3.336 nsec/m . By definition, the group delay is the inverse of the group velocity

$$\tau_g = \frac{1}{v_g} = \frac{dk}{d\omega} \quad (5.1)$$

which can be related to the material refractive index, or the modal index $n(\omega)$, by the following equation [62]

$$\tau_g = \frac{d(n(\omega)\omega/c)}{d\omega} = \frac{(n(\omega) + \omega \frac{dn(\omega)}{d\omega})}{c}. \quad (5.2)$$

By inverting the (5.2) we obtain a new expression that resembles the form of the phase velocity $v_p = c/n$

$$\begin{aligned} v_g &= \frac{c}{(n(\omega) + \omega \frac{dn(\omega)}{d\omega})} \\ &= \frac{c}{n_g} \end{aligned} \quad (5.3)$$

where n_g is called the *Group Index*, and which is defined as

$$n_g = n(\omega) + \omega \frac{dn(\omega)}{d\omega}, \quad (5.4)$$

where the second term in Eq.(5.4) accounts for the dispersion in the waveguide. Another important quantity is the delay-bandwidth product (DBP). When n_g is much larger than $n(\omega)$ it can be approximated as

$$\Delta t \Delta f \cong \frac{L \Delta n}{\lambda} \quad \text{and} \quad n_g \frac{\Delta f}{f} \cong \Delta n, \quad (5.5)$$

where Δt is the time delay at λ over the propagation distance L , Δf is the frequency bandwidth centered at f and Δn is the change that n experiences inside Δf . n_g represents the basic constraint when dealing with slowlight applications because it fixes the maximum achievable delay for a defined bandwidth. To give a better

idea for practical applications, the delay-bandwidth product indicates the maximum buffering capacity of a slowlight device.

In the following sections we will discuss about the slowlight properties of a planar waveguide with a cladding made of single negative index metamaterial and a dielectric core. We will first analyze the problem of the theoretical modeling and then discourse of the design, the realization and the experimental characterization in the microwave region of frequencies.

5.3.1 Slow-Light in Single Negative Metamaterial Waveguides

We consider a two-dimensional (2D) structure which is formed by a parallel plate waveguide (PPW). The vertical direction or the normal to the PPW is along the y -direction. If the thickness of the PPW is h , then for frequency below $c/2h$, the waveguide can only support TE waves whose electric field is in the y -direction. For example for $h = 1$ cm, microwaves below 15 GHz will be only TE waves.

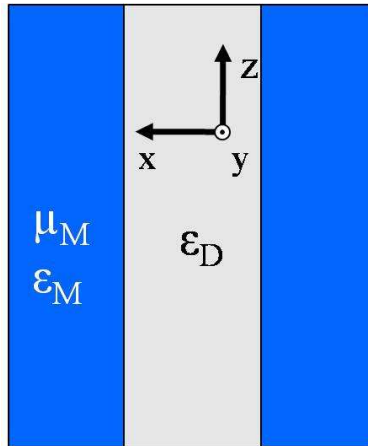


Figure 5-6: A sketch of a slab waveguide inside a parallel plate waveguide.

We thus only need to consider TE wave propagation in the xz -plane. We now consider a slab waveguide made of a dielectric with ϵ_D cladded by a negative permeability metamaterial with $\mu_M < 0$ and $\epsilon_M > 0$ as shown in Fig. 5-6. The dielectric core

layer has a thickness d . We only consider a symmetric cladding and the guided mode travels along the z -direction with the phase $e^{i(k_z z - \omega t)}$ while the transverse direction of the waveguide is along the x -axis.

The transverse components of the TE modes inside the core of the waveguide and the decay constant outside the core of the waveguide are $k_D = \sqrt{\varepsilon_D k_0^2 - k_z^2}$, $\kappa_M = \sqrt{k_z^2 - \varepsilon_M \mu_M k_0^2}$, respectively. For simplicity, we consider the core layer to be nonmagnetic. We introduce a free parameter ξ which gives $\kappa_M = \sqrt{\varepsilon_D - \varepsilon_M \mu_M} \xi / \sqrt{1 + \xi^2}$. After matching the continuity condition for the tangential electric and magnetic field, the eigenmodes equation is obtained as

$$\sqrt{\varepsilon_D} k_0 d = f_{\text{TE}}(\xi), \quad (5.6)$$

where

$$f_{\text{TE}}(\xi) = \frac{\sqrt{1 + \xi^2}}{\sqrt{1 + \sigma}} (m\pi - 2 \arctan \xi / \varrho). \quad (5.7)$$

with $\sigma = -\varepsilon_M \mu_M / \varepsilon_D$ and $\varrho = -\mu_M$. Here the index m denotes the parity of the TE_m modes with $m \geq 1$. In terms of ξ , the phase index $n_p \equiv k_z / k_0$ is given by

$$n_p = \frac{\sqrt{\varepsilon_D} \sqrt{\xi^2 - \sigma}}{\sqrt{1 + \xi^2}}. \quad (5.8)$$

To support guided TE modes which are of our interest, one has $\xi \geq \xi_{\min} = \sigma^{1/2}$ so that n_p is real.

For ordinary waveguides, the phase index n_p is a monotonically increasing function of the waveguide thickness d . Thus, the waveguide will only support one forward-wave TE_m mode for a fixed m , at the most. However, if the following condition is satisfied [63]

$$\frac{\varrho}{\sqrt{\sigma}} \frac{1 + \sigma}{\varrho^2 + \sigma} + \arctan \frac{\sqrt{\sigma}}{\varrho} \geq \frac{1}{2} m\pi, \quad (5.9)$$

Eq. (5.6) will provide two solutions for a fixed m that are for a particular d . At a critical thickness d_c , these two modes will merge into one single mode that will carry

zero total energy flow and also have a zero group velocity. One can prove that the total energy flow P_z is indeed zero at the critical thickness [63]

$$P_z = - \int_{-\infty}^{\infty} E_z H_x^* dx = P_z^{\text{in}} + P_z^{\text{out}} \quad (5.10)$$

with

$$\begin{aligned} P_z^{\text{in}} &= \frac{k_z d}{2k_0} \left[1 + (-1)^m \text{sinc } k_D d \right], \\ P_z^{\text{out}} &= \frac{k_z d}{2k_0} \left[\frac{1 + (-1)^m \cos k_D d}{\mu_M \kappa_M d} \right]. \end{aligned} \quad (5.11)$$

The parameter space for stopping TE₂ modes is shown in Fig. 5-7. From this plot we see that a maximum $\sigma_{\text{max}} = 0.2775$ exists. For $\sigma < \sigma_{\text{max}}$ there is a finite range of μ_M that sets the condition for waveguide to stop light. For example, if $\mu_M = -1$, and $\sigma < 0.1277$, the waveguide can trap TE₂ mode waves.

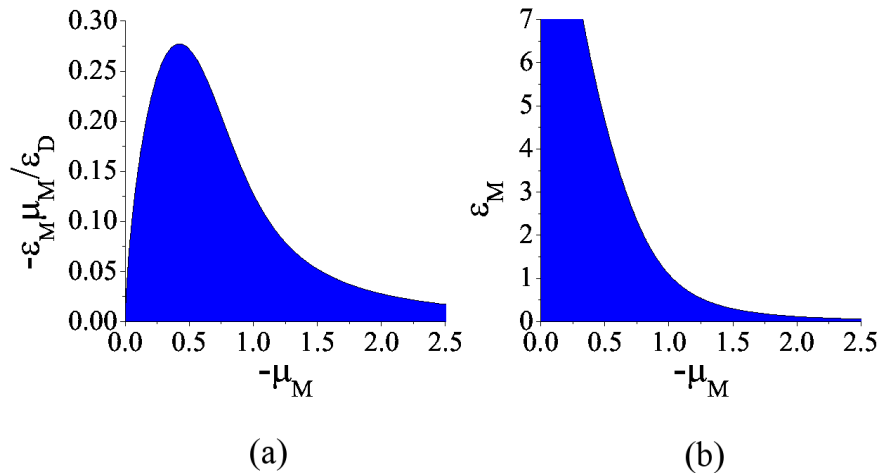


Figure 5-7: Parameter space (shaded area) for stopping light in a waveguide with (a) dielectric core (ϵ_D) and cladded with a negative permeability metamaterial ($\mu_M < 0$ and $\epsilon_M > 0$) and (b) dielectric core with $\epsilon_D = 8.6$ and cladded with a negative permeability metamaterial.

We note that the above condition is also valid for cladding with anisotropic permeability, such that one has $\mu_{Mx}, \mu_{Mz} < 0$ and $\mu_{Mx} \neq \mu_{Mz}$. For this cladding, one has $\sigma = -\mu_{Mx} \epsilon_{My} / \epsilon_D$ and $\varrho = \sqrt{\mu_{Mx} \mu_{Mz}}$, which can be used to model the TE modes

in line defect waveguides in photonic band gap materials [3].

For waves propagating inside the waveguide structure, one has $n_p = n_p(k_0, d)$ with k_0 representing the free space wave number, and d representing the waveguide dimension. For a planar waveguide, d is the thickness while for a cylindrical waveguide, d is the diameter. The group refractive index is $n_g = n_p + k_0 \partial_{k_0} n_p$, thus the divergence of $\partial_{k_0} n_p$ will lead to stopping light. In this situation, the coupling of light to the waveguide structure is very weak, however for waves in a waveguide, $\partial_{k_0} n_p$ and $\partial_d n_p$ can share the same divergence. Thus in certain waveguide structures the divergence of $\partial_d n_p$ will also lead to stopping light. In this case light with certain wavelength will be stopped at certain waveguide dimension d .

As a comparison, we consider the TE modes in a dielectric waveguide cladded with a perfect electric conductor (PEC). Only PEC cladding allows for $\langle P_z \rangle = 0$ at the band cutoff thickness $d_c = \pi / \sqrt{\epsilon_D} k_0$, therefore, $n_p = \sqrt{\epsilon_D - (\pi/k_0 d)^2}$ and $n_g = n_p + (\pi/k_0 d)^2 / n_p$. Furthermore when $d = d_c$, we have $n_p = 0$ and $n_g = \infty$, and due to the vanishing of $n_p = 0$, we have $P_z = 0$ at $d = d_c$. This waveguide does not support degenerate modes. For a dielectric waveguide cladded by a metal with finite conductivity such as copper in the microwave range, the group velocity of TE modes is always positive. However, for our waveguide, the presence of losses will give rise to a small imaginary part to the energy flow, thus with moderate material losses our waveguide is able to trap light.

5.4 Negative Permeability with SRRs

The subsequent step in the study of the slowlight properties of the above mentioned planar waveguide is to understand the best way to achieve, in practice, the condition $\mu < 0$ and $\epsilon > 0$. There are many ways in which negative effective permeability can be achieved, for example by varying the temperature of 3D dielectric composites consisting of dielectric ceramic cube arrays [64]. It has been proven that strong subwave-

length magnetic resonance can be excited in dielectric cubes corresponding to the first Mie resonance mode, and can be continuously and reversibly adjusted from 13.65 to 19.28GHz with the temperature changing from -15 to 35°C . Negative permeability can be also obtained in millimeter waves regime, at cryogenic temperatures utilizing a multilayer stack of ferromagnetic and superconducting thin films [65]. Still, another possible way to achieve negative effective permeability is with polaritonic photonic crystals [66] made of LiTaO_3 , where negative μ is realized in the micron wavelength range. For our purpose, the most suitable candidate for realizing $\mu < 0$ is using a split ring resonator array. This is the best metamaterial to use because it does not require low temperature systems to control the magnetic response, as the case of dielectric ceramic cube arrays and superconductor metamaterials. Moreover, photonic crystals are not suitable because TM polarization (H field out of plane) is required to obtain $\mu < 0$, and experimentally it cannot be realized in a parallel plate waveguide. In [10] we showed that making the cladding with a square geometry SRRs array can lead to the negative permeability condition.

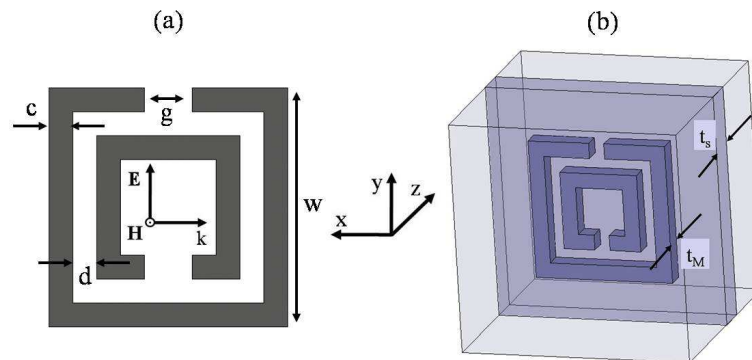


Figure 5-8: (a) SRR layout. (b) SRR unit cell. The dimensions are $w = 3\text{mm}$, $d = c = g = 0.33\text{mm}$. The unit cell size is

In figure 5-8(a) is shown the layout for a split ring resonator geometry, while in Fig. 5-8(b) is shown the 3D unit cell used for the computation of metamaterial effective parameters using the procedure illustrated in the previous chapter. The structure is arranged in a cubic lattice geometry with a period of $a = 5\text{mm}$. The lateral size of the SRR is $w = 3\text{mm}$, whereas the remaining parameters are $d = c = g = 0.33\text{mm}$, and

a 0.25mm thick copper SRR is deposited on a 0.45mm thick Epoxy (FR-4) dielectric substrate ($\epsilon = 4.4$, $\tan \delta = 0.01$ at 1GHz). In Fig. 5-9(a) are shown the simulated transmission and reflection coefficient under normal incidence condition.

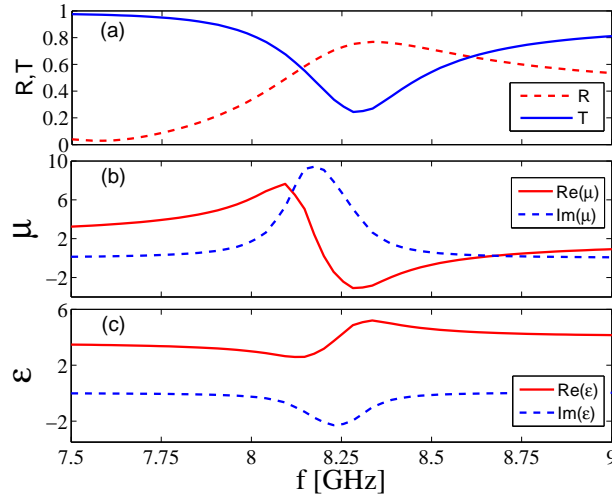


Figure 5-9: (a) Computed transmission and reflection coefficients. (b)-(c) The retrieved effective parameters ϵ and μ for SRR shown in Fig. 5-8

For this design the resonance frequency is at 8.27GHz . The retrieved effective parameters (see Figs. 5-9(b) and 5-9(c)) show, as theoretically predicted, a positive imaginary part for the permeability and a negative imaginary part for the permittivity. The reason that the imaginary part of the permittivity can be negative is due to the finite lattice period associated with the metamaterial structure, as discussed in [57]. This effect is called antiresonance, in contrast to the resonance shown by the positive imaginary part of μ_M .

The next step of the slow light waveguide design is to find the most appropriate values of ϵ_M and μ_M to meet the condition in Eq. (5.9) for TE_2 . This requires that the magnitudes of both ϵ_M and μ_M be small. From our simulations we fixed our choice at $f = 8.57\text{GHz}$, where $\mu_M = -0.22 + i0.27$ and $\epsilon_M = 4.4 - i0.14$.

For the lossless case the phase index for the TE_m modes is calculated and plotted in Fig. 5-10 for a waveguide with core layer $\epsilon_D = 8.6$ and cladded with $\epsilon_M = 4.4$ and $\mu_M = 0.22$ at 8.57GHz . The critical thickness is $d_c = 0.781\text{cm}$.

When we introduce losses the condition for trapping light is lost, and the n_p curve

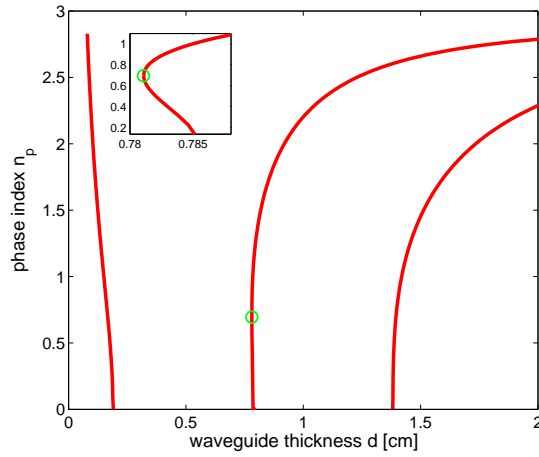


Figure 5-10: Phase index n_p as a function of thickness d for waveguide with core layer $\epsilon_D = 8.6$ and cladded with $\epsilon_M = 4.4$ and $\mu_M = 0.22$ at 8.57 GHz in the lossless case. The circle marks the location of zero group velocity

plotted in Fig. 5-10 changes, as shown in Fig. 5-11. The n_p curve splits in two branches, one accounting for a forward wave (red line) traveling in the core and the other corresponding to a backward wave (blue line) which exists in the cladding with $\mu_M < 0$.

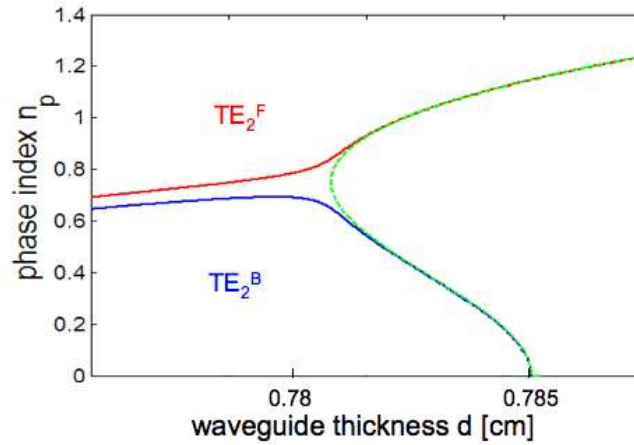


Figure 5-11: Phase index n_p as a function of thickness d when losses are introduced. The cladding has $\mu_M = -0.22 + i0.27$ and $\epsilon_M = 4.4 - i0.14$.

In [10] the waveguide design was made considering a dielectric core made of alumina ($\epsilon_D = 8.6$). Our goal now is to build a structure having a core made of air. There are two reasons to justify this choice, the first is due to the negligible dielectric losses related to the air while the second is because the scanning of the electromagnetic field

inside the core by using antennas would be easier and more accurate. Unfortunately there is a drawback. When the permittivity inside the core lowers there is a drastic reduction of the allowed values for $Re(\mu_M)$ and $Re(\epsilon_M)$ that satisfy Eq. (5.9). The new parameter space is shown in Fig. 5-12. We see that the constraint $\epsilon_D = 1$ makes the design more complicated since it is obtained at the expense of very small values for ϵ_M and μ_M . This represents a serious restriction, more for the design of the effective permeability function then for the permittivity.

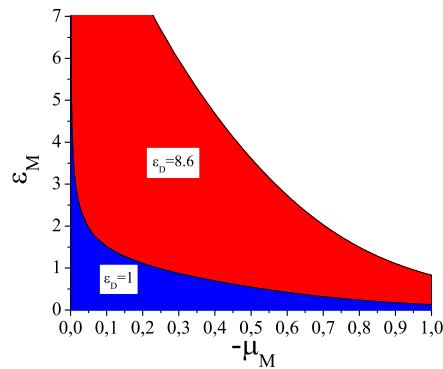


Figure 5-12: Parameter space for stopping light in a waveguide with a dielectric core made $\epsilon_D = 8.6$ (red area) and a core made of air $\epsilon_D = 1$ (blue area)

In fact, when the $Re(\mu_M)$ approaches the crossing point between the negative and positive region its absolute value becomes comparable to the $Im(\mu_M)$ causing an enlargement of the gap between the two branches of n_p (See Fig. 5-11) and a corresponding recession from the slow light condition. This is not an issue regarding ϵ_{eff} since generally the $Re(\epsilon_M) \gg Im(\epsilon_M)$.

For this reason a new design for the split ring resonator is required. We found that the geometry shown in Fig. 5-13(a) can fulfill our requirements. This is the same geometry used by *Smith et al.* to experimentally prove the electromagnetic cloak at microwaves [9]. In order to further reduce the losses contribution due to the supporting medium another material was chosen. This new dielectric substrate consists of Duroid, which has $\epsilon_r = 2.2$ and $\tan \delta = 0.001$ at $10GHz$. Today, Duroid represents one of the best material for microwave applications because of low dielectric

losses. In Fig. 5-13(c) are shown the transmission and reflection curves obtained from the numerical simulation performed under normal incidence on a single cubic unit cell (see Fig. 5-13(b)) having $a = 10/3\text{cm}$, $w = 0.1\text{mm}$, $l = 3\text{mm}$, $s/l = 0.6$ and $g = 0.4\text{mm}$.

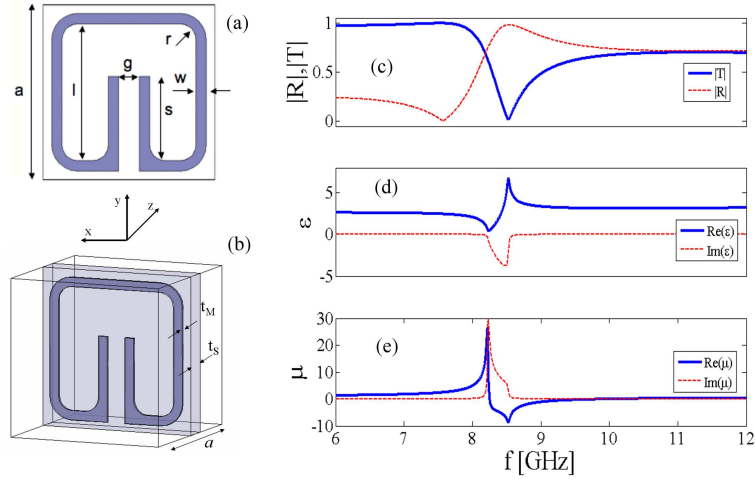


Figure 5-13: (a) Layout and (b) 3D unit cell of the SRR geometry used to in the experiment. (a) Transmission and reflection, (b) effective permeability and (c) effective permittivity parameters corresponding to the unit cell in (b).

Unlike the previous SRR geometry, where the main resonance is determined by the capacitances between the internal and external rings, here the capacitance depends on two factors: the gap width g , and the ratio s/l . In general the electromagnetic response can be tuned by varying the the values of g , s/l , and the radius of curvature r [9]. The corresponding retrieved effective parameters are shown in Fig. 5-13(d)-(e) where at first glance it can be observed that the new SRR shape provide a magnetic and electric response sharper than that obtained from the two rings systems.

The main advantage of this design is in the larger resonance bandwidth and the reduced magnetic losses. Numerical simulations have demonstrated that the single split ring resonator has a resonant bandwidth of about 1.6GHz , a value that is almost four times larger than two split rings case, and which is also in agreement with Pendry's results shown in equation 4.16. The result of this is that the new design shows a larger μ'/μ'' ratio, which is exactly the goal that we wanted to accomplish.

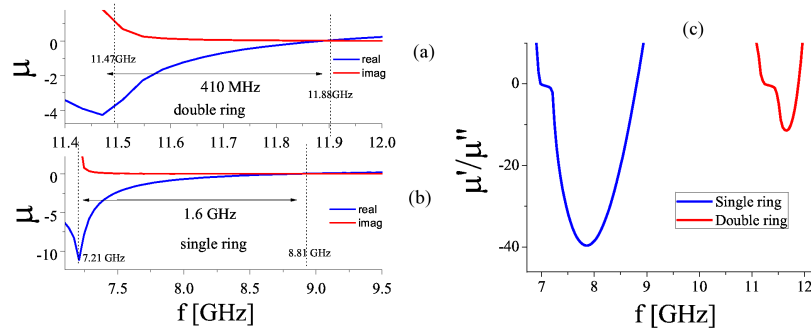


Figure 5-14: (a) Comparison of the effective permeability for (a) the double split ring resonators shown in Fig. 5-8 and (b) the single SRR in Fig. 5-13. (c) Plot of the ratio of the real part and the imaginary part of the effective parameters shown in (a) and (b).

For this reasons we pick this as the final design for the metamaterial based cladding, where we expect, according to the parameter space shown in Fig. 5-12, that the slowlight conditions will be achieved in the frequency band $[9 - 9.2] GHz$.

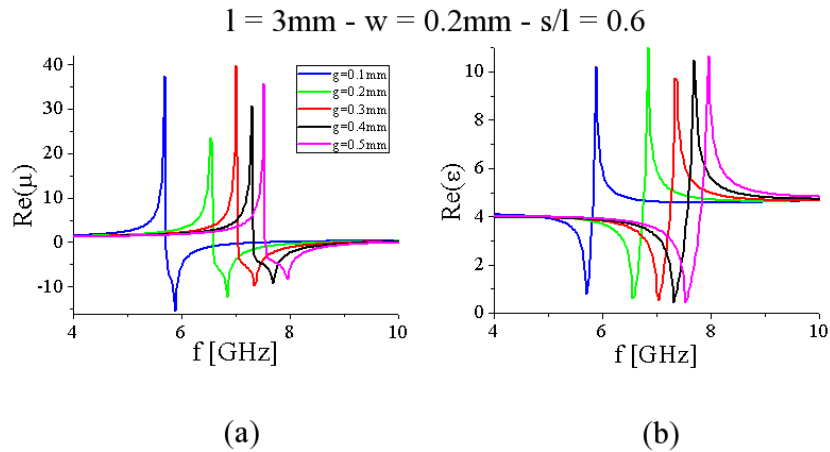


Figure 5-15: Real part of the effective permeability (a) and permittivity (b) for different values of the gap g .

Figure 5-15 shows how the resonance properties of the SRR response can be modulated by the gap width g . As expected, the resonance frequency increases with increasing the distance g between the two capacitor plates of length s .

Further characterizations of the SRR are shown in figure 5-16 where a parametric analysis of the magnetic and electric response is made by varying the parameters s/l , w and r . The ratio s/l strongly modulates the resonant frequency ω_0 because

it modifies the value of the capacitance C , while, the radius r can be used to tune the real part of the effective permittivity ϵ in the regions of frequency above the resonance.

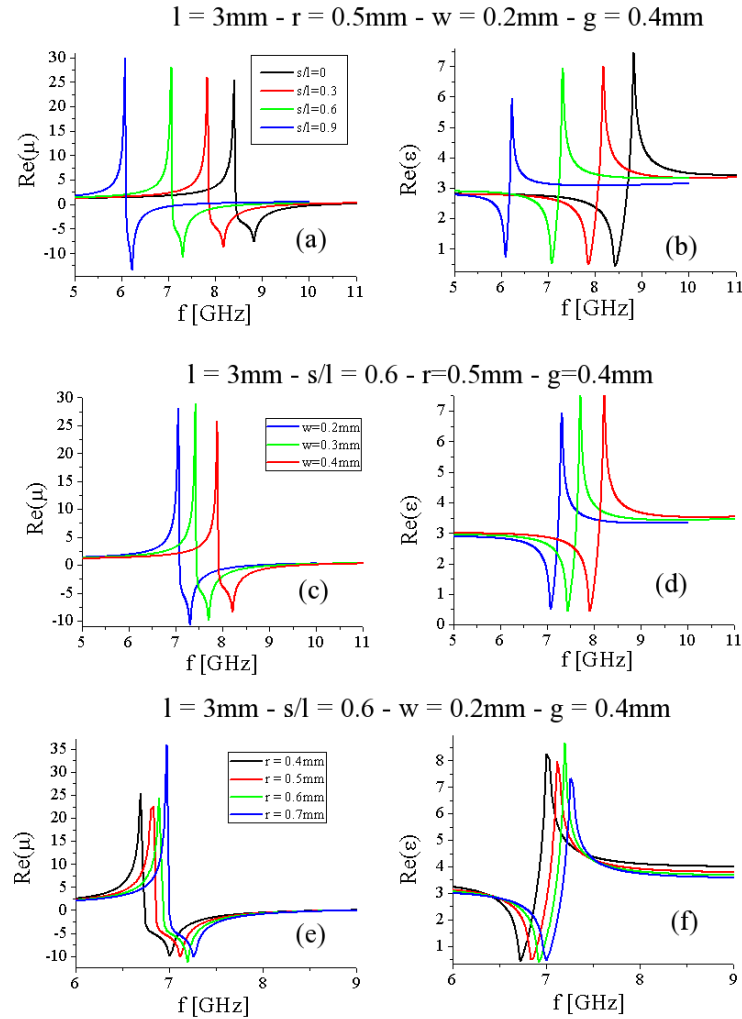


Figure 5-16: Real part of the effective permeability and permittivity for different values of the (a)-(b) ratio s/l , (c)-(d) metal with w and (e)-(f) radius of curvature r .

CHAPTER 6

Waveguide Realization and Experimental Results

6.1 Microfabrication of SRRs Based Metamaterials

The metamaterial structures using periodic arrangement of SRRs were made in house, using the clean room facilities at Northeastern University in Boston. Each side of the cladding was designed in the shape of rectangular slab having height $h_M = 1cm$, length $l_M = 40cm$ and width $w_M = 3cm$ while the size of each unit cell were $a = 10/3cm$, $w = 0.1mm$, $l = 3mm$, $s/l = 0.6$ and $g = 0.4mm$.

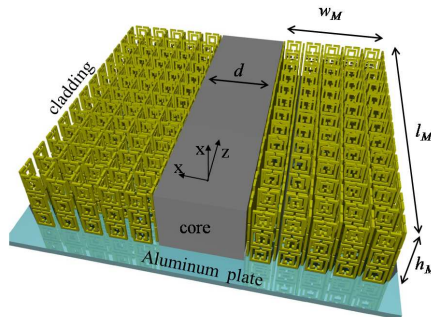


Figure 6-1: 3D illustration of the slow-light structure. The SRRs and the dielectric core (grey) are placed between two parallel metal plates. The top plate is not shown here.

Moreover, the slab is obtained by orthogonally assembling the SRRs deposited on rectangular stripes along the direction of propagation z and along the direction normal to the wave guide axis x , as shown in figure 6-1. The material that we have used is high frequency laminate made of a $0.5mm$ thick Duroid ($\epsilon_r = 2.2$ and $\tan \delta = 0.001$ at $10GHz$) dielectric layer with two copper layers $8\mu m$ thick which have been deposited on the two sides. To create the SRRs we have used the traditional micro-fabrication techniques, as listed below:

1. Spin Coating,

the AZ9260 photoresist was deposited on a $14cm \times 14cm$ square wafers. The spinning was done at 1000rpm for 1 minute in order to obtain a $17\mu m$ thick photoresist layer.

2. Soft Bake for 25 minutes at 125° in oven.

3. Photolithography,

the process was made by using a *Quintel4000 Optical Aligner* exposing the sample for 160s with a dose of $2240mJ/cm^2$

4. Resist Development was performed for 3mins with solution AZ400K:H2O (1:1)

5. Wet Etching,

the copper was removed using the APS-100 copper etchant at $70^\circ C$ for 2 minutes

6. Resist Stripping,

the resist was removed by dipping the sample in a AZ400T stripper for about 2 minute.

Fig.6-2(a)-(e) illustrate the above steps. In Fig.6-2(a) is shown the equipment used to make the spin coating, while Fig.6-2(b) shows the picture of the mask. Figs.6-2(c) and (d) show the photolithography and wet etching steps respectively and Fig.6-2(e) shows the last step of resist stripping.

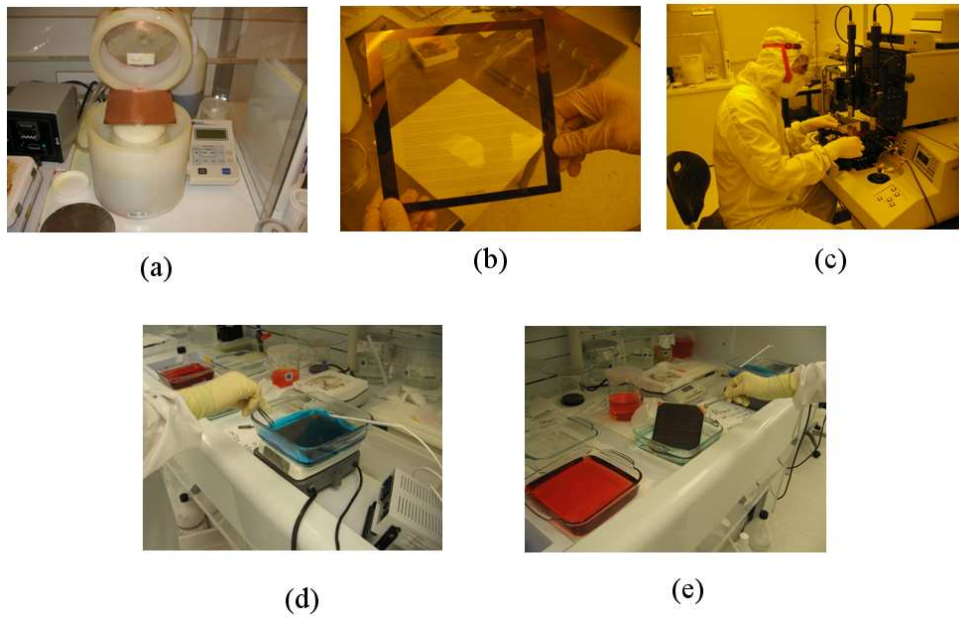


Figure 6-2: (a) Spin coater with the wafer ready to be processed. (b) Mask and (c) machine used for the photolithography. (d) Wet etching step. (e) Stripping

Figs. 6-3(a)-(c) display in order a wafer with the layout of the copper SRRs, the Duroid stripe retrieved from the wafer using a laser cut and the final slab assembled with the stripes orthogonally interlaced with each other.

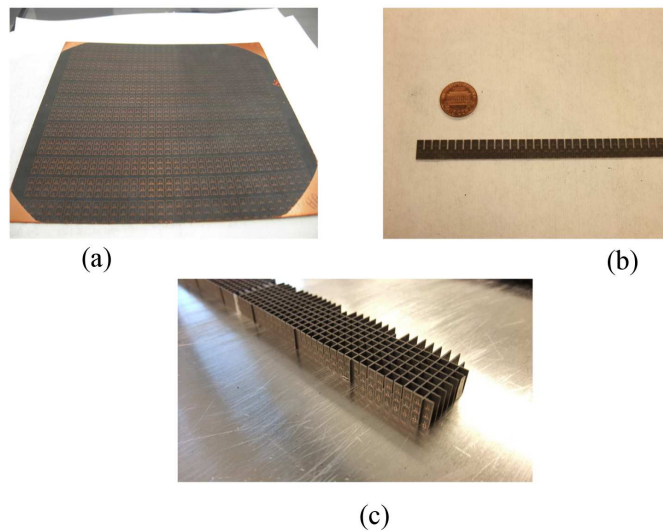


Figure 6-3: (a) Wafer sample with the SRRs layout, (b) single stripe provided with gaps used to assemble the metamaterial slab in (c).

6.2 Experimental Characterization of the SRRs

The first step in order to experimentally characterize the SRRs medium is to check if a resonance dip is visible in the transmission curve. If this check is positive and a gap in the transmission band is present, we can move to the second step which is to prove that the gap is the result of the magnetic resonance. In order to test this we have manufactured a wafer made entirely of *closed ring resonators* (CRRs) which due to the lack of the aperture in the ring we expect will destroy the magnetic response without affecting the electric resonance. As also shown in [67], the presence of a frequency gap in the scattering parameter S_{21} of the SRR slab, but not in the CRR slab is a proof that $\mu_{eff} < 0$ in the frequency band.

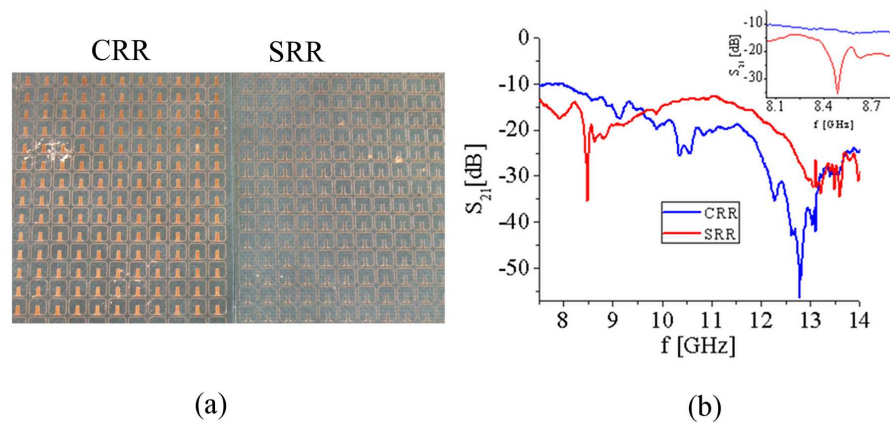


Figure 6-4: (a) Wafers with a CRR and SRR copper layout. (b) Transmission curve for the CRR slab (blue line) and SRR slab (red line), the inset shows a magnification of the curves around the magnetic resonance.

Fig. 6-4(b) confirms the evidence of the presence of a magnetic resonance. The red and blue curves in Fig. 6-4(a) show the measured scattering parameters S_{21} respectively for the SRR and CRR media. The measurements have been performed on a single wafer in free space using two horn antennas placed at the same distance from the object under test. The wafer was oriented parallel to the propagation direction with the ring axis parallel to the \mathbf{H} field. Moreover, it is worth noting that at higher frequencies an additional resonance of electrical nature becomes present, which true of both samples, and which was also reported in [67]. Further characterizations of the

slab with SRRs consist to study the transmission properties under different orientation of the ring axis.

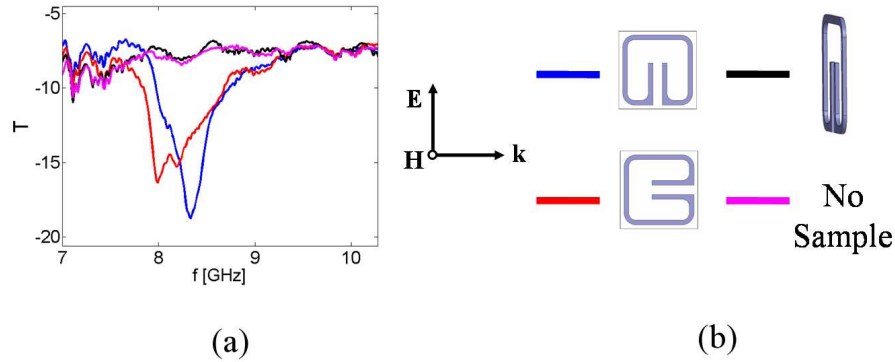


Figure 6-5: (a) Transmission curves for corresponding to the different ring orientation showed in (b).

Experimental data are shown in Fig. 6-5(a) where each different curve corresponds to the transmission under a different orientation of the SRRs in respect to the electromagnetic field, as illustrated in Fig. 6-5(b). As expected, there is no resonance (black line) when the SRR plane is parallel to the \mathbf{H} field since no current can be induced in the ring. However, there is a difference in the response when the SRR is symmetric or not in the propagation direction. The transmission curves for the two different orientations differ to each other as shown in Fig. 6-5(a), where the blue curve refers to the symmetric case, and where the red line corresponds to the asymmetric case. The breaking of the symmetry induces a shift of the absorption to lower frequencies, as also studied numerically by *Markoš et. al.* [68]. This phenomenon is evidence of the bianisotropic behavior shown by a medium made of SRRs [69].

To conclude the first part of the spectral characterization of the SRR metamaterial we have measured the transmission properties of the rectangular slab in Fig. 6-3(c). Unlike the above results, this measure was carried out in a parallel plate waveguide using two dipole antennas: one to transmit, and the other to pick up the signal. The antennas we placed opposite to each other, 1cm apart from the sample. The measured transmission curve is plotted in Fig. 6-6. An excellent agreement with the transmission obtained from numerical design (red line) is found. Comparing the

band gap width of the present slab with that in the inset of Fig. 6-4 corresponding to the transmission from a single planar wafer where the SRRs are replicated along the wafer plane only, it is evident that the latter has a larger resonance bandwidth of approx. 1GHz when compared to the former which has a resonance bandwidth of approx. 300MHz . It is worth mentioning that a similar result was also found, both numerically and experimentally by *Weiland et.al.* [70]. This proves that the resonance bandwidth of a metamaterial structure made of SRRs increases with an increasing number of “atoms” elements that forms the array.

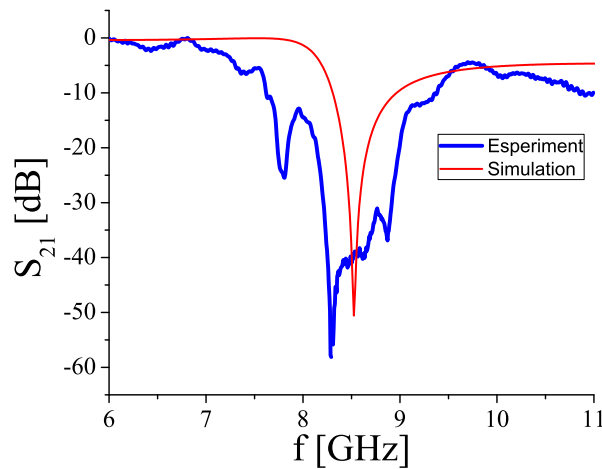


Figure 6-6: Measured (blue line) and simulated (red line) scattering parameter S_{21} in a normalized scale, corresponding to the metamaterial slab showed in Fig. 6-3(c).

For a better understanding of the band gap properties of arrays of an SRRs we have conducted more systematic measurements in a parallel plate waveguide under normal incidence. This is a useful step in order to study the effect of the density at which the interlaced stripes shown in Fig. 6-3(b) and (c) are assembled. In Fig. 6-7(a) are plotted the scattering parameters for three rectangular slabs where the stripes containing the SRRs are arrayed only along the direction x perpendicular to the propagation axis z . The length of these stripes are always the same and equal to $8a$, where a is the unit cell period as shown in Fig. 5-13. The parameters l_x and l_z represent the period at which each stripe is replicated respectively along the x and z directions. Clearly the resonance band broadens when increasing the density of

the parallel elements by reducing the distance between the stripes. This also has the effect of pulling down the resonance frequency which is in agreement with Pendry's prediction [8], and also reported in equation (4.15).

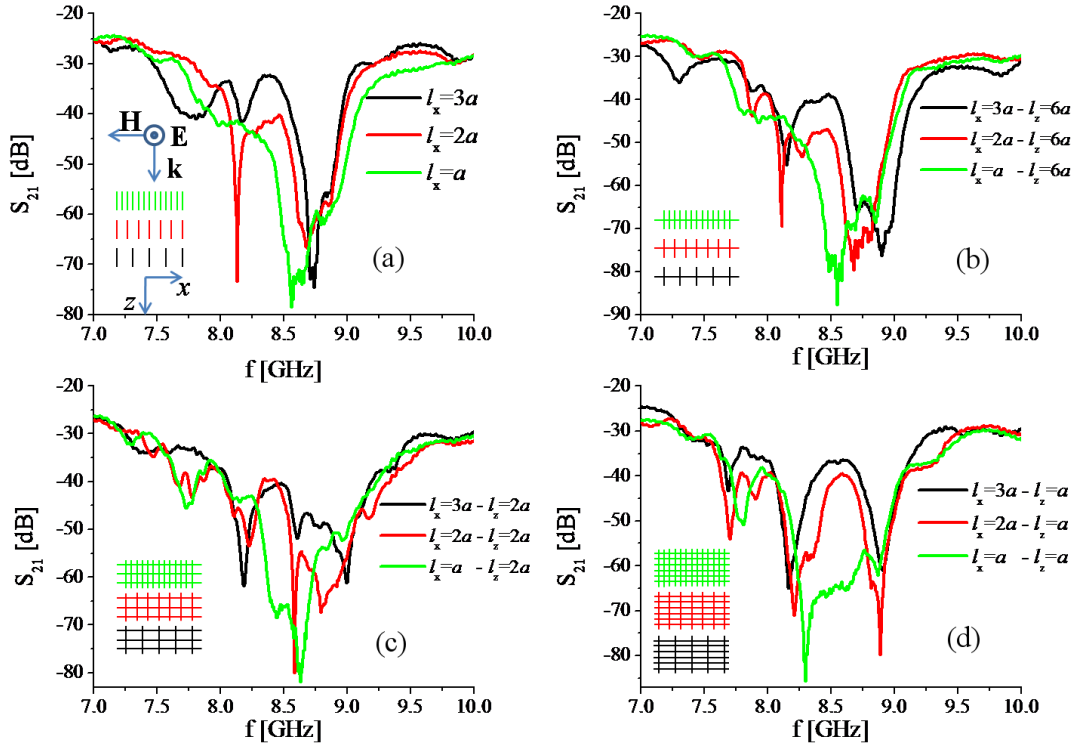


Figure 6-7: (a) Measured scattering parameters for the case of parallel stripes arrayed along the x direction only with period l_x equal to a (green), $2a$ (red) and $3a$ (black). Scattering parameters measured for $l_z = 6a$ (b), $l_z = 2a$ (c) and $l_z = a$ (d). In the insets are the schematics of the arrayed slabs realized with interlaced stripes.

Figs. 6-7(b)-(d) illustrate the influence of the SRRs stripe density along the z direction for each of the examples analyzed in 6-7(a). The results are very interesting. In fact, when $l_z = 6a$ as in Fig. 6-7(b) variations are visible only for the case with $l_x = 3a$ (black line) where a slightly broader resonance bandwidth is measured. No other substantial distinctions from the examples in Fig. 6-7(a) are noticed meaning that the interaction between the orthogonal elements becomes effective only for the lowest density case, $l_x = 3a$ and $l_z = 6a$. When $l_z = 2a$ (see Fig. 6-7(c)) a split in the resonance is very obvious when $l_x = 3a$ (black line), which weakens when

$l_x = 2a$ (red line). On the other hand, the case $l_x = a$ (green line) shows no resonance splitting, and no significant variation in terms of resonance band. The last case that was investigated was $l_z = a$ (see Fig. 6-7(d)), under this condition the magnetic resonance splitting becomes more evident than in the case of $l_z = 2a$, but only when $l_x = 2a$ (black line) and $l_x = 3a$ (red line), whereas the resonance bifurcation is still absent when $l_x = a$. Hence, we can say that by fixing the number of stripes arrayed in the x direction the split in the resonance appears by reducing the density of stripes arrayed along the propagation direction z , but only when $l_x > a$. When $l_x = l_z = a$ the resonance band does not split, but instead becomes more broad than in the case shown in Fig. 6-7(a) by approx. $300MHz$.

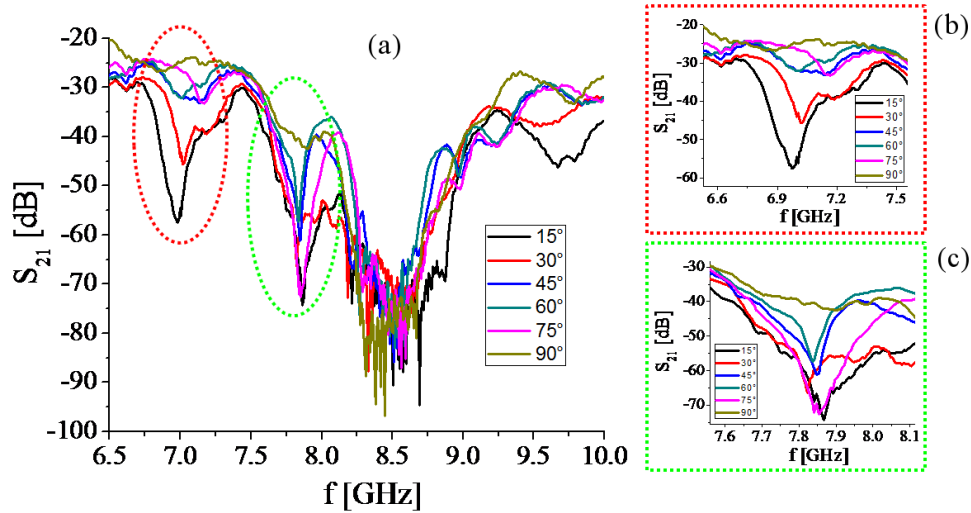


Figure 6-8: (a) Scattering parameters obtained measuring the transmission from a slab made with $l_x = l_z = a$ illuminated with a plane wave impinging the sample at different angles. (b) and (c) magnification of the resonance band highlighted in (a) respectively with red and green dotted lines.

It is also interesting to note the transmission properties for the different angles of incidence of the source. We have performed measurements for six different angles, from 30° to 90° , on a slab with $l_x = l_z = a$, and found that large resonant dips appear at frequencies below the main resonance frequency of approx. $8.5GHz$. As shown in Fig. 6-8(a) when the beams arrive at 90° only the main resonance is present, however when the slab is tilted additional resonances start to appear: the first at

7.85GHz (green dotted line) and then at 7GHz (red dotted line). In the former case the largest deeps are for 15° and 75°, whereas for the latter case the resonance is stronger only when the incident angles are very far from the orthogonal condition, at 15° and at 30°. Except for the small angles the properties of the principal resonant bands are almost unchanged. This result demonstrates that when the slab is arranged with $l_x = l_z = a$ the structure can be assimilated to a homogeneous medium as the transmission properties around the resonant frequency remain practically the same.

6.3 Experimental Characterization of the Slowlight Waveguide

6.3.1 Experimental Setup

After ascertaining that the measured resonance is of magnetic nature it is now possible to carry on with the study of the slow light properties of a planar waveguide structure having a dielectric core, and a cladding made with a periodic array of SRRs. As displayed in Fig. 6-9, each side of the cladding is made with a rectangular slab of the following size: length $l_M = 40cm$, width $w_M = 2.3cm$ and $1cm$ high. The slab width w_M corresponds to 7 unit cells which from our calculation is a distance large enough to ensure that the mode inside the metamaterial is decayed at the interface with the air. The choice of the length l_M is the result of several trials showing that longer cladding fits the requirements of the experiment better.

The planar waveguide has been sandwiched between two aluminum parallel plates, and microwave absorbers have been used to kill reflections and to assure a perfect matching condition for the electromagnetic field. A dipole antenna has been used to excite the propagation mode inside the metamaterial waveguide, while another dipole antenna acted as a receiver.

The experimental setup (shown in Fig. 6-10) consists of an HP-70820A microwave

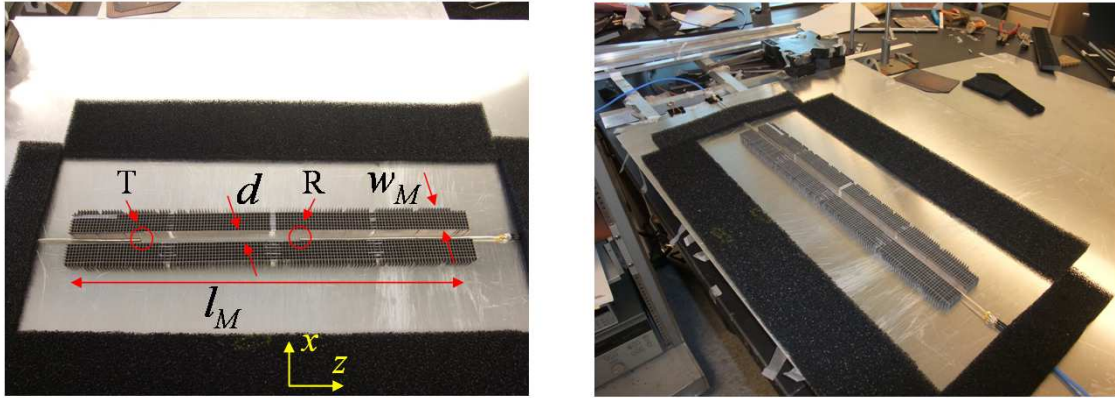


Figure 6-9: Pictures of the planar waveguide having a cladding made of metamaterial cladding ($l_M = 40\text{cm}$, $w_M = 2.3\text{cm}$ and height 1cm) and a core made of air. T and R indicate the position of the transmitting and receiving antenna.

transition analyzer (MTA) connected to an HP-8341B synthesized sweeper (SS). The internal modulator of the MTA generates a pulse width of 100ns . The pulse thus generated with a carrier frequency in the microwave region is made to pass through two transmission lines A and B using a splitter. A represents the line containing the sample, while B serves as the reference channel consisting of a microwave coaxial cable. Two isolators are connected to the beam splitter to prevent reflected signals from interfering with the signals feeding the reference and sample transmission lines. The two signals exiting from A and B are then analyzed by the two MTA input channels. In all measurements, the background time delay caused by the transmission lines is well accounted in order to obtain the time delay due to the sample only. The group velocity is obtained using the formula

$$v_g = \frac{L}{t_m - \frac{L}{v_w}} \quad (6.1)$$

where L is the sample length, t_m is the measured time delay (due to the waveguide plus the sample), and v_w is the dispersion velocity in the parallel plate waveguide without the metamaterial sample.

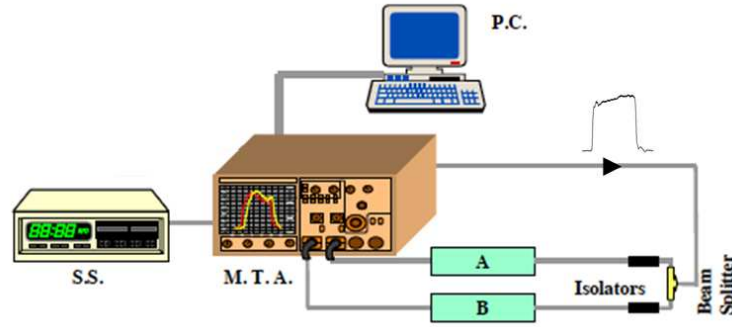


Figure 6-10: Schematic of the experimental setup used to perform the pulsed measurements. A computer controlled microwave transition analyzer MTA modulates the signal generated from the synthesized sweeper SS and feeds, by a rectangular shaped pulse, two lines: A containing the metamaterial sample, and B which is used as a reference. The source is sent to A and B using a power beam splitter. Two isolator are inserted to avoid kill reflections. The two signals from A and B are then sent in the two MTA ports.

6.3.2 Pulsed Measurements

Based on the effective parameters retrieved in the previous chapter, we expect the slowlight effect to take place very close to the metamaterial bandgap edge where the real part of the permeability is extremely small. We performed a set of pulse delay measurements for different values of the waveguide core thickness d over a certain frequency range centered at $9.1GHz$. The measured value of the group index $n_g = c_0/v_g$ are displayed in Fig. 6-11 for different values of d , where c_0 is the speed on the light in vacuum, and v_g is related to the measured delay by Eq. (6.1). Data show that when the core thickness is fixed to $d = 1.8cm$ the $n_g(f)$ has the largest amplitude in the band $f = [9 - 9.15]GHz$.

Fixed the frequency, if we plot n_g as a function of the parameter d we obtain the results shown in Fig. 6-12, plotted only for selected carrier frequencies $f = 9.04GHz$ (gree), $f = 9.45GHz$ (blue) and $f = 9.06GHz$ (red). The measured values of the group index are lower than the theoretical one by a factor of about two. Further investigations of this remains ongoing, however we think that this difference could be related either to a larger magnetic losses or to a larger value of the real part of the effective permittivity. In fact both can contribute to pulling down the group

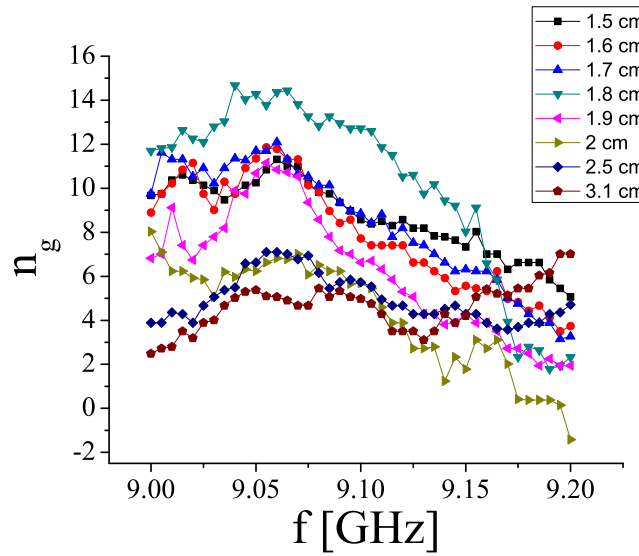


Figure 6-11: Measured values of the group index n_g over a range frequencies f . The different color of the curves correspond to different value of the core thickness d .

index value of this device. Many questions remain answered at the conclusion of this research. The first question is whether or not the present structure could be made more efficient considering different unit cell designs. Another question is related to the design method itself. More accurate numerical simulations, where the study of effective parameters is made considering more than a single unit cell, would explain better the intrinsic limitations related to the present approach. The main obstacle here is the computational capacity that would be required to simulate a large array of SRRs, where reliable results can only be obtained using an adequate mesh size to describe the resonant elements. As a third point to question is the influence of the losses by performing an experiment at cryogenic temperatures where the sample can be dipped in liquid nitrogen, and where the losses due to the copper can be reduced. Even if the performance results shown by the present structure are a stretch from those present in literature, they are still significant in confirming that slowlight phenomena can be achieved in planar waveguide structures under the condition of a single negative index cladding. Moreover, the present results can in principle also be applied at near infrared and optical frequencies, where gain can be introduced to the

material to recover for the losses [63].

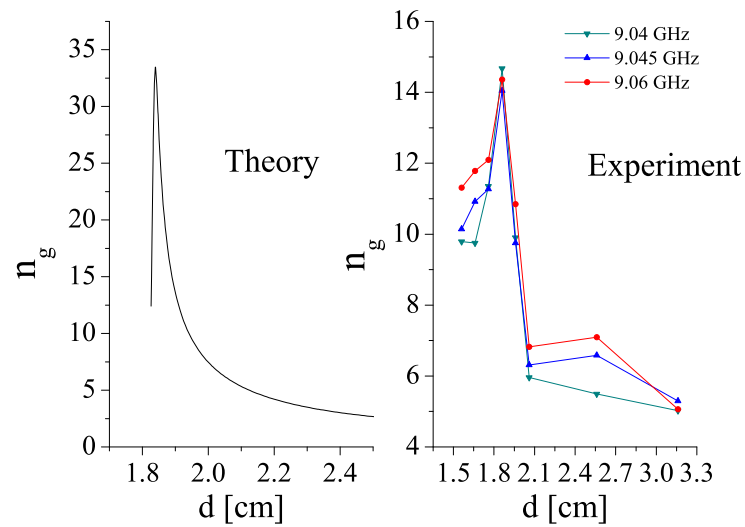


Figure 6-12: Group index plotted versus the core thickness d for fixed frequencies. (a) n_g profile predicted by the model, (b) experimental values.

Conclusions and Perspectives

The results shown in this dissertation reflect my research activities that were conducted during the three years of my PhD studies both at the University of Naples “Federico II”, and at Northeastern University in Boston Massachusetts. While at the University of Naples “Federico II” I worked on two main projects which were both at the microwave frequency range. The first, was the experimental demonstration of the Pendellösung effect, which was done in collaboration with the IMM-CNR research group in Naples, and the second, was on the superlensing properties of 1D dielectric PCs, which was entirely done with the mentorship of my advisor, Prof. Andreone, and with the support of his research group. Both projects led to papers that were published in Optics Express [39, 71].

The Pendellösung effect is a relatively well known phenomenon of the Dynamical Diffraction Theory (DDT), which is a rigorous formalism that accounts for multiple scattering effects that are especially important in X-ray, electron and neutron diffraction from perfect crystals. The Pendellösung effect states that the energy transmitted at the exit-point of a crystal can be periodically modulated by varying the crystal thickness. Measurements were carried out by placing alumina rods with nominal permittivity $\epsilon_r = 8.6$, radius $r = 0.4\text{cm}$, and height $h = 1\text{cm}$, in a square geometry with $r/a = 0.255$ ($a = 1.57\text{cm}$) sandwiched in an aluminum parallel-plate waveguide terminated with microwave absorbers, and where the intensity of the transmitted signal was measured by an HP8720c wave vector analyzer. The results of these experiments showed that the ratio of the energy transmitted in the positive direction to that transmitted in the negative direction is a periodic function of the number of

rows in the PC confirming that the Pendellösung effect also exists in PCs.

The superlensing properties of 1D PCs represents the first experimental proof of the subwavelength imaging properties achieved with 1D periodic dielectric structures. For this dissertation, I demonstrated point imaging measurements using two different lenses, each having the same lattice properties but with different index contrast. The results showed that the flat lens, not only acts as a superlens, but can easily be focused at different frequency bands. It should be mentioned that these properties are difficult to achieve in 1D PCs, in comparison with 2D PCs superlenses.

During my studies at Northeastern University I worked in the laboratory of Prof. S. Sridhar in the field of slowlight. As of late, the concept of slow light is attracting large interest from the scientific community, most notably because of its promising capabilities in the area of telecommunications. The ability to slow down and even stop light is crucial in order to achieve all-optical integrated circuitry. My study in slow light consisted of the design, realization and experimental investigation, at a microwave wavelength, of a planar waveguide made of a conventional dielectric core layer cladded with negative permeability material. Such a structure supports degenerate propagating modes for which the group velocity, and total energy flow, can be zero if the media are lossless. My research plan for this study consisted of four different steps. The first stage studied the problem of finding the most suitable material to realize a cladding with $\mu < 0$ and $\epsilon > 0$. Step two was to consider the design and modeling of the structure by using commercial computational software. For the third phase, I created the samples using micro-fabrication techniques made possible by Northeastern Universitys clean room facilities. The last step consisted of the full electromagnetic characterization of the metamaterial medium sandwiched inside a microwave parallel plate waveguide. I performed an accurate study of the spectral properties of the bulk metamaterial analyzing the resonance properties for different incident angles of the source, as well as for different spatial densities of the constituent elements. Here I found an excellent agreement between the numerical and

experimental results. Finally, I studied the slow light properties of a planar waveguide made with a single negative metamaterial cladding from SRRs with core made of air. I found that the results agreed with the theoretical model.

Regarding my studies on photonic crystals, the results that I have obtained can be extended to the design of photonic devices working at frequencies which were not investigated in this work, such as near infrared and optics . Both the Pendellösung effect and superlensing in 1D PCs can be used to build structures suitable for integration onto photonic chips by means of micro and nano-fabrication techniques. For example, in near infrared regime, the silicon on insulator (SOI) support is the traditional material used. The Pendellösung effect can now be used to build new types of polarizing beam splitters which are crucial for the manipulation of light. In addition, the superlensing effect can be used for applications such as nanolithography where it is fundamental to use systems capable of resolving features smaller than the wavelength, beating the diffraction limit.

In the diffractive metamaterials field, structures like SRRs and cut wires are continually proving their potential as basic building blocks for composite metamaterials. Beside the current applications in the microwave regime, which are very attractive for military based applications like the invisible cloak, today, there is increasing interest in the design and realization of metamaterial structures at terahertz frequencies. Until recently, the terahertz region was the only unexplored spectrum region because of the lack of adequate emitters and detectors necessary to bridge the terahertz gap [72]. Thanks to their astonishing properties, SRRs based metamaterials have proved to be the best candidates for making possible modulators and absorbers [73–75]. But one of the biggest challenge remaining will be the building of THz image sensors, for homeland security purposes, that are capable of capturing pictures using the same method of conventional optical cameras. This will drastically reduce the delay time of current THz imaging systems based on raster-scan approach. Again, it is here that metamaterials have the most promise.

Bibliography

- [1] J. B. Pendry and D. R. Smith, “Reversing light with negative refraction,” *Physics Today*, vol. 57, p. 37, 2003.
- [2] E. D. Gennaro, P. V. Parimi, W. T. Lu, and S. Sridhar, “Slow microwaves in left-handed materials,” *Phys. Rev. B*, vol. 72, p. 033110, 2005.
- [3] T. Baba, “Slow light in photonic crystals,” *Nature Photonics*, vol. 2, p. 465, 2001.
- [4] T. Tanabe, M. Notomi, E. Kuramochi, A. Shinya, and H. Taniyama, “Trapping and delaying photons for one nanosecond in an ultrasmall high-q photonic-crystal nanocavity,” *Nature Photonics*, vol. 1, p. 49, 2007.
- [5] K. L. Tsakmakidis, A. D. Boardman, and O. Hess, “trapped rainbow storage of light in metamaterials,” *Nature Photonics*, vol. 450, p. 397, 2007.
- [6] S. A. Cummer, B. Popa, D. Schurig, D. R. Smith, J. Pendry, M. Rahm, and A. Starr, “Scattering theory derivation of a 3d acoustic cloaking shell,” *Phys. Rev. Lett.*, vol. 100, p. 024301, 2008.
- [7] D. A. Genov, S. Zhang, and X. Zhang, “Mimicking celestial mechanics in metamaterials,” *Nature Physics*, vol. 5, p. 687, 2009.
- [8] J. B. Pendry, A. J. Holden, D. J. Robbins, and W. J. Stewart, “Magnetism from conductors and enhanced nonlinear phenomena,” *IEEE Transaction on Microwave Theory and Techniques*, vol. 7, p. 11, 1999.

-
- [9] D. Schurig, J. J. Mock, B. J. Justice, S. A. Cummer, J. B. Pendry, and D. R. S. A. F. Starr, "Metamaterial electromagnetic cloak at microwave frequencies," *Science*, vol. 314, p. 977, 2006.
- [10] W. T. Lu, S. Savo, B. D. F. Casse, and S. Sridhar, "Slow microwave waveguide made of negative permeability materials," *Microwave and Optical Technology Letters*, vol. 51, p. 2705, 2009.
- [11] J. B. Pendry, A. J. Holden, W. J. Stewart, and I. Youngs, "Extremely low frequency plasmons in metallic mesostructures," *Phys. Rev. Lett.*, vol. 76, p. 4773, 1996.
- [12] V. G. Veselago, "The electrodynamic of substances with simultaneously negative value of ϵ and μ ," *Soviet Physics Uspekhi*, vol. 10, p. 509, 1968.
- [13] J. B. Pendry, "Negative refraction makes a perfect lens," *Phys. Rev. Lett.*, vol. 85, p. 3966, 2000.
- [14] M. Notomi, "Theory of light propagation in strongly modulated photonic crystals: Refractionlike behavior in the vicinity of the photonic band gap," *Phys. Rev. B*, vol. 62, p. 10696, 2000.
- [15] M. Rahm, S. A. Cummer, D. Schurig, J. B. Pendry, and D. R. Smith, "Optical design of reflectionless complex media by finite embedded coordinate transformations," *Phys. Rev Lett.*, vol. 100, p. 063903, 2008.
- [16] M. Rahm, D. A. Roberts, J. B. Pendry, and D. R. Smith, "Transformation-optical design of adaptive beam bends and beam expanders," *Optics Express*, vol. 16, p. 11555, 2008.
- [17] A. V. Kildishev and V. M. Shalaev, "Engineering space for light via transformation optics," *Optics Letters*, vol. 33, p. 43, 2008.

- [18] M. Rahm, D. Schurig, D. A. Roberts, S. A. Cummer, J. B. Pendry, and D. R. Smith, "Design of electromagnetic cloaks and concentrators using form-invariant coordinate transformations of maxwells equations," *Phot. and Nanostr. - Fund.and Appl.*, vol. 6, p. 87, 2007.
- [19] R. Liu, C. Ji, J. J. Mock, J. Y. Chin, T. J. Cui, and D. R. Smith, "Broadband ground-plane cloak," *Science*, vol. 323, p. 366, 2009.
- [20] S. Xi, H. Chen, T. Jiang, L. Ran, J. Huangfu, B. Wu, J. A. Kong, and M. Chen, "Experimental verification of the reversed cherenkov radiation in left-handed metamaterials," *Phys. Rev Lett.*, vol. 103, p. 194801, 2009.
- [21] S. Zhang and X. Zhang, "Flipping a photonic shock wave," *Physics*, vol. 2, p. 91, 2009.
- [22] J. D. Joannopoulos, S. G. Johnson, J. N. Winn, and R. D. Meade, *Molding the Flow of Light*. Princeton University Press, 2008.
- [23] N. Ashcroft and N. Mermin, *Solid State Physics*. Thomson Brooks-Cole, 1976.
- [24] S. Foteinopoulou and C. Soukoulis, "Electromagnetic wave propagation in two-dimensional photonic crystals: A study of anomalous refractive effects," *Phys. Rev. B*, vol. 72, p. 165112, 2005.
- [25] L. Brillouin, *Wave Propagation in Periodic Structures*. Dover Publication, Inc., 1946.
- [26] A. Taflov and S. Hagness, *Computational Electrodynamics, the Finite-Difference-Time-Domain Method*. Artech House, 2005.
- [27] A. Authier, *Dynamical Theory of X-ray Diffraction*. Oxford University Press, Oxford, 2001.

- [28] P.P.Ewald, "Zur theorie der interferenzen der röntgenstrahlen," *Physik Z*, vol. 14, p. 465, 1913.
- [29] P.P.Ewald, "Crystal optics for visible light and x rays," *Rev. Mod. Phys*, vol. 37, p. 46, 1965.
- [30] N. Kato and A. R. Lang, "The projection topograph: a new method in x-ray diffraction microradiography," *Acta Cryst.*, vol. 12, p. 249, 1959.
- [31] D. Sippel, K. Kleinstu, and G. E. R. Schulze, "Pendellösungs-interferenzen mit thermischen neutronen an sieinkristallen," *Phys. Lett*, vol. 14, p. 174, 1965.
- [32] C. G. Shull, "Observation of pendellösung fringe structure in neutron diffraction," *Phys. Rev. Lett.*, vol. 21, p. 1585, 1968.
- [33] V. Mocella, J. Hrtwig, J. Baruchel, and A. Mazuelas, "Influence of the transverse and longitudinal coherence in dynamical theory of x-ray diffraction," *J. Phys. D: Appl. Phys*, vol. 32, p. A88, 1999.
- [34] V. Mocella, "Negative refraction in photonic crystals: thickness dependence and pendellösung phenomenon," *Optics Express*, vol. 13, p. 1361, 2005.
- [35] V. Mocella, P. Dardano, L. Moretti, and I. Rendina, "A polarizing beam splitter using negative refraction of photonic crystals," *Optics Express*, vol. 13, p. 7699, 2005.
- [36] A. Balestreri, L. C. Andreani, and M. Agio, "Optical properties and diffraction effects in opal photonic crystals," *Phys. Rev. E*, vol. 74, p. 603, 2006.
- [37] O. Francescangeli, S. Melone, and R. D. Leo, "Dynamical diffraction of microwaves by periodic dielectric media," *Phys. Rev. A*, vol. 40, p. 4988, 2006.
- [38] M. L. Calvo, P. Cheben, O. Martnez-Matos, F. del Monte, and J. A. Rodrigo, "Experimental detection of the optical pendellösung effect," *Phys. Rev. Lett.*, vol. 97, p. 801, 2006.

- [39] S. Savo, E. D. Gennaro, C. Miletto, A. Andreone, P. Dardano, L. Moretti, and V. Mocella, "Pendellösung effect in photonic crystals," *Optics Express*, vol. 16, p. 9097, 2008.
- [40] D. Pozar, *Microwave Engineering*. John Wiley & Sons, Inc, 2005.
- [41] C. Luo, S. G. Johnson, J. D. Joannopoulos, and J. Pendry, "All-angle negative refraction without negative effective index," *Phys. Rev. B*, vol. 65, p. 201104, 2002.
- [42] X. Wang, Z. F. Ren, and K. Kempa, "Unrestricted superlensing in a triangular two-dimensional photonic crystal," *Optics Express*, vol. 12, p. 2919, 2004.
- [43] H. Zhang, L. Shen, L. Ran, and Y. Yuan, "Layered superlensing in two-dimensional photonic crystals," *Optics Express*, vol. 14, p. 11178, 2006.
- [44] S. Feng, H. Y. Sang, Z. Y. Li, B. Y. Cheng, and D. Z. Zhang, "Sensitivity of surface states to the stack sequence of one-dimensional photonic crystals," *J. Opt. A: Pure Appl. Opt.*, vol. 7, p. 374, 2005.
- [45] B. Wang, L. Shen, and S. He, "Superlens formed by a one-dimensional dielectric photonic crystal," *J. Opt. Soc. Am. B*, vol. 25, p. 391, 2008.
- [46] T. Decoopman, G. Tayeb, S. Enoch, D. Maystre, and B. Gralak, "Photonic crystal lens: from negative refraction and negative index to negative permittivity and permeability," *Phys. Rev. Lett.*, vol. 97, p. 073905, 2006.
- [47] C. Luo, S. G. Johnson, and J. D. Joannopoulos, "Subwavelength imaging in photonic crystals," *Phys. Rev. B*, vol. 68, p. 045115, 2003.
- [48] R. D. Meade, K. D. Brommer, A. M. Rappe, and J. D. Joannopoulos, "Electromagnetic bloch waves at the surface of a photonic crystal," *Phys. Rev. B*, vol. 44, p. 10961, 1991.

- [49] S. Xiao, M. Qiu, Z. Ruan, and S. He, "Influence of the surface termination to the point imaging by a photonic crystal slab with negative refraction," *Appl. Phys. Lett.*, vol. 85, p. 4269, 2004.
- [50] B. Wang, W. Dai, A. Fang, L. Zhang, G. Tuttle, T. Koschny, and C. M. Soukoulis, "Surface waves in photonic crystal slabs," *Phys. Rev. B*, vol. 74, p. 195104, 2006.
- [51] B. D. F. Casse, W. T. Lu, R. K. Banyal, Y. J. Huang, S. Selvarasah, M. R. Dokmeci, C. V. Perry, and S. Sridhar, "Imaging with subwavelength resolution by a generalized superlens at infrared wavelengths," *Optics lett.*, vol. 34, p. 1994, 2008.
- [52] E. Moreno, L. Martin-Moreno, and F. J. Garcia-Vidal, "Efficient coupling of light into and out of a photonic crystal waveguide via surface modes," *Photonics and Nanostructures - Fundamentals and Applications*, vol. 2, p. 97, 2004.
- [53] J. Zhou, T. Koschny, M. Kafesaki, E. N. Economou, J. B. Pendry, and C. M. Soukoulis, "Saturation of the magnetic response of split-ring resonators at optical frequencies," *Phys. Rev. Lett.*, vol. 95, p. 223902, 2005.
- [54] R. W. Ziolkowski and E. Heyman, "Wave propagation in media having negative permittivity and permeability," *Phys. Rev. E*, vol. 64, p. 056625, 2001.
- [55] S. S. R. A. Shelby, D. R. Smith, "Experimental verification of a negative index of refraction," *Science*, vol. 292, p. 77, 2001.
- [56] D. R. Smith, S. Schultz, P. Markos, and C. M. Soukoulis, "Determination of effective permittivity and permeability of metamaterials from reflection and transmission coefficient," *Phys. Rev. E*, vol. 65, p. 195104, 2002.
- [57] T. Koschny, P. M. D. R. Smith, and C. M. Soukoulis, "Resonant and antiresonant frequency dependence of the effective parameters of metamaterials," *Phys. Rev. E*, vol. 68, p. 065602, 2003.

- [58] D. R. Smith, D. C. Vier, T. Koschny, and C. M. Soukoulis, "Electromagnetic parameters retrieval from inhomogeneous metamaterials," *Phys. Rev. E*, vol. 71, p. 036617, 2005.
- [59] D. R. Smith, W. J. Padilla, D. C. Vier, S. C. Nemat-Nasser, and S. Shultz, "Composite medium with simultaneously negative permeability and permittivity," *Phys. Rev. Lett*, vol. 84, p. 4184, 2000.
- [60] M.D.Lukin and A. Inamoglu, "Controlling photons using electromagnetically induced transparency," *Nature*, vol. 413, p. 273, 2001.
- [61] C. H. B. C. Liu, Z. Dutton and L. V. Hau, "Observation of coherent optical information storage in an atomic medium using halted light pulses," *Nature*, vol. 409, p. 490, 2001.
- [62] C. Pollok and M. Lipson, *Integrated Photonics*. Kluwer Academic Publisher, 2003.
- [63] W. Lu, Y. Huang, B. Casse, R. Banyal, and S. Sridhar, "Storing light with single negative-index metamaterials," *Submitted*.
- [64] Q. Zhao, B. Du, L. Kang, H. Zhao, Q. Xie, B. Li, X. Zhang, J. Zhou, L. Li, and Y. Meng, "Tunable negative permeability in an isotropic dielectric composite," *Appl. Phys. Lett.*, vol. 92, p. 051106, 2008.
- [65] A. Pimenov, A. Loidl, P. Przyslupski, and B. Dabrowski, "Negative refraction in ferromagnet-superconductor superlattices," *Phys. Rev. Lett*, vol. 95, p. 247009, 2005.
- [66] K. C. Huang, M. L. Povinelli, and J. D. Joannopoulos, "Negative effective permeability in polaritonic photonic crystals," *Appl. Phys. Lett.*, vol. 85, p. 543, 2004.

- [67] K. Aydin, I. Bulu, K. Guven, M. Kafesaki, C. M. Soukoulis, and E. Ozbay, “Investigation of magnetic resonances for different split-ring resonator parameters and designs,” *New J. Phys.*, vol. 7, p. 168, 2005.
- [68] P. Markos and C. M. Soukoulis, “Numerical studies of left-handed materials and arrays of split ring resonators,” *Phys. Rev. E*, vol. 65, p. 036622, 2002.
- [69] Z. Li, K. Aydin, and E. Ozbay, “Determination of the effective constitutive parameters of bianisotropic metamaterials from reflection and transmission coefficients,” *Phys. Rev. E*, vol. 79, p. 026610, 2009.
- [70] T. Weiland, R. Schuhmann, R. B. Gregor, C. G. Parazzoli, A. M. Vetter, D. R. Smith, D. C. Vier, and S. Schultz, “Ab initio numerical simulation of left-handed metamaterials: Comparison of calculations and experiments,” *Journ. of Appl. Phys.*, vol. 90, p. 5419, 2009.
- [71] S. Savo, E. D. Gennaro, and A. Andreone, “Superlensing properties of one-dimensional dielectric photonic crystals,” *Optics Express*, vol. 17, p. 19848, 2009.
- [72] C. Sirtori, “Bridge for the terahertz gap,” *Nature*, vol. 417, p. 132, 2002.
- [73] H. T. Chen, W. J. Padilla, J. M. O. Zide, A. C. Gossard, A. J. Taylor, and R. D. Averitt, “Active terahertz metamaterial devices,” *Nature*, vol. 444, p. 597, 2002.
- [74] H. T. Chen, W. J. Padilla, M. J. Cich, A. K. Azad, R. D. Averitt, and A. J. Taylor, “A metamaterial solid-state terahertz phase modulator,” *Nature Photonics*, vol. 3, p. 148, 2009.
- [75] H. Tao, A. C. Strikwerda, K. Fan, W. J. Padilla, X. Zhang, and R. Averitt, “Reconfigurable terahertz metamaterials,” *Phys. Rev. Lett.*, vol. 103, p. 147401, 2009.